CHARACTERIZATION OF THE EFFECTS OF RACK1 EXPRESSION ON MITOCHONDRIAL PHYSIOLOGY

by

Michaela Kember

Submitted in partial fulfillment of the requirements
for the degree of Master of Science

at

Dalhousie University
Halifax, Nova Scotia
July 2023

To my first two teachers, Guy and Sue Kember. Thank you, Mom and Dad, for your continuous support and endless love. You are the reason I have achieved goals I never thought possible throughout my personal and academic career.

Table of Contents

List of Tables

List of Figures

Abstract

Receptor of activated protein C kinase 1 (RACK1) is a 36-kDa multifunctional scaffolding protein that coordinates a variety of fundamental cellular processes in eukaryotic cells, including signal transduction, protein synthesis, and cellular migration. RACK1 has been implicated in the development of multiple pathological scenarios, and loss of RACK1 homeostasis is implicated in cancers, heart disease, and neurodegenerative disorders. However, clear characterization on the role of RACK1 expression in eukaryotic cells has been complicated by its ubiquitous cellular presence and massive number of binding partners. A poorly described region of RACK1 biology is how RACK1 function interacts with mitochondrial physiology. Mitochondria are semi-autonomous organelles critical for the management of cellular roles including energy production, stress responses, and death. While RACK1 and mitochondria have numerous overlapping roles in cell health and disease pathology, a broad characterization of mitochondrial structure and function in the context of aberrant RACK1 signaling has yet to be completed. Therefore, the goal of this research project was to characterize how a decrease in RACK1 expression impacts mitochondrial physiology in HeLa cells. We chose three pillars of mitochondrial function to investigate in the context of a decrease in RACK1 expression (RACK1 KD) in HeLa cells. This included characterization of mitochondrial morphology (membrane integrity/network dynamics); mitochondrial energy production (including oxygen consumption rates and ATP production); and mitochondrial genomics (mt-DNA levels, biogenesis/fusion/fission mediator expression). We discovered that RACK1 KD cells exhibited a loss of mitochondrial network connectivity, dysregulation of mediators required for mitochondrial network dynamics/biogenesis, and decreases in mitochondrial respiration and energy production. Low glucose conditions further increased this phenotype in RACK1 KD cells. These results represent the first in-depth characterization focused solely upon the connection between RACK1 expression and mitochondrial structure and function.

List of Abbreviations and Symbols Used

βc	human common beta	3
ADP	adenosine diphosphate	8
ATP	adenosine triphosphate	7
Bax	Bcl-2 Associated X-protein	12
Bcl-2	B-cell lymphoma-2	11
Bcl-xL	B-cell lymphoma-xL	12
BDNF	neurotrophic factor	3
Bim	pro-apoptotic protein Bcl-2 Interacting Mediator of cell death	11
cAMP/PKA	cyclic AMP and protein kinase A	3
COX I	cytochrome c oxidase	25
CytB	cytochrome b	25
DJ-1	Parkinson disease protein 7	12
DNM1L	dynamin 1-like protein	20
Drp1	Dynamin related protein 1	7
FAK	focal adhesion kinase	3
FBS	heat-inactivated fetal bovine serum	16
FCCP	carbonylcyanide-4-(trifluoromethoxy) phenylhydrazone	32
HG	high glucose	14
HRP	horseradish peroxidase	19
HyD	hybrid detector	23

IGF-1R	insulin-like growth factor receptor I	3
IP3R	membrane-associated inositol 1,4,5-trisphosphate receptors	2
KD	RACK1 knockdown	14
LG	low glucose	14
MAO-B	Monoamine oxidase-B	12
MAPs	mitochondrial-associated proteins	11
MFN1	Mitofusin 1	7
MFN2	Mitofusin 2	7
MOAP-1	Modulator of apoptosis 1	12
MRPL	mitochondrial large sub-unit protein	14
MRPS	mitochondrial small sub-unit protein	14
MRPs	mitochondrial ribosomal proteins	13
mt	mitochondrial	6
mt-DNA	mitochondrial DNA	35
ND1	nicotinamide adenine dinucleotide ubiquinone oxidoreductase chain 1	25
ND6	nicotinamide adenine dinucleotide ubiquinone oxidoreductase chain 6	25
NMDAR	N-methyl D-aspartate receptor	2
OCR	oxygen consumption rate	31
OPA1	Optic atrophy 1	7
OXPHOS	Oxidative phosphorylation	8
padj	significant adjusted p-value	32

PDE4D5	phosphodiesterase 4D5	3
PGC1α	peroxisome proliferator-activated receptor-γ coactivator	7
PKCBII	protein kinase C	1
PVDF	polyvinylidene fluoride membrane	19
RACK1	Receptor of activated protein C kinase 1	1
RNR1	mitochondrially encoded 12S ribosomal RNA	25
RNR2	mitochondrially encoded 16S ribosomal RNA	25
ROS	reactive oxygen species	6
RT-qPCR	reverse transcription quantitative real-time PCR	17
SDS	Sodium dodecyl sulfate	17
SDS-PAGE	SDS-polyacrylamide gel electrophoresis	18
TBST	Tris Buffered Saline with Tween 20	19
TEM	transmission electron microscopy	13
TFAM	mitochondrial transcription factor A	7
WD40	tryptophan-aspartate repeat	1

Acknowledgements

A great number of people guided me during my Masters project and made this project possible. I would like to give my warmest thanks to my supervisor, Dr. Zhenyu Cheng, for his constant encouragement and guidance throughout this project. Thank you for your endless patience and kindness over the years - from a undergraduate summer project in 2019 to the completion of my Masters – it has truly meant the world to me. You have seen me through some hard times in the last 4 years and I am so grateful for your unwavering support! I would also like to thank my committee members, Dr. Barbara Karten and Dr. Yassine El-Hiani, who were extremely supportive during this project. Thank you for providing me with lots of kind feedback and providing tools from your own labs that helped my project. I would also like to thank Dr. Craig McCormick for serving as my external examiner. The wonderful members of the Cheng lab made every day in lab an absolute joy. Thank you to Renee Raudonis for answering my millions of questions and helping me at a moment's notice with anything and everything in the lab. Thank you to all of my lab members for their valuable assistance, troubleshooting/discussing my little project with me, and giving me endless feedback, especially Dr. Said Daboor, Dr. Zhong Sun, and Yunnuo Shi. Thank you to Yunnuo and Shannen for their early morning/late night chats in lab, you provided me with so much moral support! I am also extremely grateful to the following individuals who took time from their busy schedules to support my experiments: Mary Ann Trevors, for her knowledge and expertise that helped me create my TEM images; Gerard Gaspard, who had endless patience for my inept confocal microscopy skills, and whose creativity and care for my project helped me create a beautiful final result; Gopal Pathak, who taught me how to run a seahorse assay; Lauren Westhaver, who kindly supported my learning curve regarding mitochondrial DNA; and Gabriela Gomes, who was always a text away to answer my many, many questions. I would also like to thank the Boudreau, Gujar, and Thomas labs, who kindly offered their lab spaces for my project. Finally, I would like to gratefully acknowledge the Beatrice Hunter Cancer Research Institute, who funded my masters research.

Chapter 1

Introduction

1.1 RACK1: a broad overview of structure and function

1.1.1 RACK1 history and structure

Receptor of activated protein C kinase 1 (RACK1) is a 36-kDa multifunctional scaffolding protein that coordinates a variety of fundamental cellular processes in eukaryotic cells [162]. RACK1 was originally identified as a receptor for the active conformation of protein kinase C (PKCBII), but it is now known that RACK1 facilitates many protein-protein interactions either directly or as part of a larger complex [124],[123],[122],[143]. RACK1 is a member of the ancient and highly conserved tryptophan-aspartate repeat (WD40) family of proteins [76],[141],[172],[100]. The WD40-repeat protein family is found in all eukaryotes, and its family members have been identified as players in almost every eukaryotic signaling pathway (reviewed in [76]). RACK1 adopts a seven-bladed β-propeller structure comprised of 40 tryptophan-aspartate repeats [94],[139]. WD40 proteins, including RACK1, are unique from other β-propeller-forming proteins in that they lack direct catalytic enzymatic activity. Instead, they employ their broad structure as a scaffold which acts as a central hub to organize cellular signaling events that become linear or branching signaling networks [141],[172],[100],[106]. In addition, RACK1's β-propeller structure appears to permit varying post-translational modifications to its residues, including O-GlcNAcylation [36] and phosphorylation/dephosphorylation, which alter its activity or cellular location accordingly [62]. The characteristics of RACK1's β-propeller structure allow it to modify its activity in response to its varying cellular location and protein partnerships, making RACK1 a highly adaptable scaffold within the dynamic cellular environment [106]. RACK1 is highly conserved throughout eukaryotic evolution, and is ubiquitous in mammalian cells, where it is highly expressed in most tissues [31],[3]. While RACK1 has been suggested to be nonessential for cellular

life in multiple eukaryotic organisms (including yeast and human immortalized cell lines) [59], abberant RACK1 activity leads to significantly altered cellular signaling [51],[102], shifts in translation [148],[42], and improperly regulated protein quality control in the cell [60],[92],[138],[145]. Furthermore, global deletion of the RACK1 gene *GNB2L1* (G-protein beta subunit-like 1), or decreases in its expression, has been shown to devastate regular cellular function [31]. The RACK1 knockout mouse model produced by Volta et al. (2013) [156] showed deletion of *GNB2L1* is lethal during gastrulation, suggesting that RACK1 expression is crucial for mammalian development.

1.1.2 Characterization of RACK1 interactome and signaling roles

To date, RACK1 has been associated in previous literature reviews with over 80 confirmed binding partners [139],[1],[77]. These partners include receptor/non-receptor kinases, phosphatases, phosphodiesterases, ion channels, membrane-associated inositol 1,4,5-trisphosphate receptors (IP3R), G-proteins/ GPCRs, apoptosis mediators, integrins/adhesion molecules, and ribosomes (all reviewed by [1]) (Figure 5.1A). During these interactions, RACK1 is not limited to operating as a standalone platform within protein complexes but can form both homodimers with itself and heterodimers with other proteins [178],[26],[151],[34]. So far, the complete identification of the RACK1 interactome is complicated by RACK1's environmental adaptability. RACK1's interaction profile and cellular distribution is dependent upon external factors such as cell type and the differential expression of surrounding binding partners. This allows RACK1 to play distinct roles in pathways depending on the cell type, even when RACK1 expression is unchanging throughout different tissue types [1],[77]. The differential compartmentalization of RACK1 in the brain exemplifies how RACK1 binding partners vary by environmental influence: in hippocampal and dorsal striatal neurons, RACK1 associates with both the glutamate receptor N-methyl D-aspartate receptor (NMDAR) and the NMDAR activator Fyn kinase. Here, RACK1 actively blocks Fyn and therefore NMDAR activity [176],[174]. In the cerebral cortex, RACK1 is bound to Fyn but not to NMDAR [174]; and in the ventral striatum, RACK1 is not associated with either of these proteins despite their presence in this brain region [175],[160]. Once bound, RACK1 can influence its partners in four major ways: i)

translocation, where it shuttle its partners from one cellular site to another; ii) activity modification, where it is able to promote or prevent the enzymatic activity of its partners; iii) changing intermolecular interactions between various molecular players, by enhancing the association or dissociation of proteins in complexes of varying sizes; and modulating the stability of its binding proteins to either protect against or promote degradation (reviewed in [77]) (Figure 5.1B). These interactions may be constitutively associated (for example, RACK1 binds the Src kinase to maintain its inactive state until signaled to dissociate [151],[174],[175],[160],[89]) or association may occur following a regulated signal (for example, where RACK1 shuttles PKCβII which enables the kinase to phosphorylate its substrate at the appropriate site [121]). The proteins that interact with RACK1 can be broadly divided into three major categories: signaling proteins in cytoplasm and nucleus, the cytosolic domains of membrane-spanning receptors, and finally, its organellar partners (reviewed in [77]) (Figure 5.1B). Notable examples of cytoplasmic or nucleic proteins known to interact with RACK1 include members of the cyclic AMP and protein kinase A (cAMP/PKA) pathway, the Src family of non-receptor protein tyrosine kinases, and PKC enzymes [1]. RACK1's role within the same signaling pathways shifts depending on whether it is cytoplasmic and nucleic: for example, cytoplasmic RACK1 enables interaction between the cAMP/PKA pathway and NMDAR, allowing NDMAR activation [151]. RACK1 additionally binds phosphodiesterase 4D5 (PDE4D5), a cAMP-degrading enzyme that manages cAMP levels [177],[6], to tightly regulate activity of the focal adhesion kinase (FAK), binding to PDE4D5, which modulates cell polarity [131],[132]. However, RACK1 in the nucleus activates the cAMP pathway to signal β-actin association with nucleic protein brain-derived neurotrophic factor (BDNF) neurotrophic factor (BDNF), supporting cAMP-dependent regulation of BDNF transcription in the nucleus [174],[99]. Examples of the latter category include ubiquitous receptor groups such as the insulin-like growth factor receptor I (IGF-1R)[66],[183] β integrin receptors [74],[80], type I interferon receptor [154], IP3R [109], and multiple ion channels in the CNS and heart [28],[139]. More specialized receptor groups include the cardiac muscarinic acetylcholine receptors [119], the human common beta (βc) receptor for immune system stimulants IL-5, IL-3 and GM-CSF [46], and the adipose-specialized hormone receptor AdipoR1 [173]. RACK1 is additionally capable

of scaffolding interactions between these different membrane receptor groups: for example, RACK1 expression promotes fibroblast migration by bridging communication between β1 integrin receptors and the extracellular matrix, which signal for membrane receptor IGF-1R activation [67],[64],[65],[63]. The third and final group of organellar partners includes ribosomal RACK1. RACK1 is a member of the ribosomal 40S subunit complex [47], where it regulates translation initiation and creates a signaling platform for translation [134],[103]. RACK1 stably binds to the 40S subunit close to the mRNA exit channel [130]. When translation is required, RACK1-associated PKCβII phosphorylates eIF6, which then induces 80S ribosome formation [22],[32]. In yeast, RACK1 homolog Asc1 has been implicated in "closed-loop-dependent ribosome recruitment", where it interacts with eIF4E, eIF4G, and Pab1 to transcribe short mRNAs [149].

1.1.3 RACK1 impact upon disease development and cellular dysfunction

RACK1 activity is heavily involved in cellular processes such as cytoskeletal regulation and cell migration, cell survival and death, proliferation, and is becoming heavily implicated as a mediator of both canonical and non-canonical autophagy [43],[184],[69]. It plays critical roles in organismal processes such as embryogenesis, neural network management, neuronal health and maintenance, and heart function [11],[68],[140],[180],[161],[78],[146],[112]. As this number of binding partners and their associated cellular functions increases, so has its link with an array of disease states. Aberrant RACK1 signaling has been associated with brain developmental disorders and neurodegenerative diseases [165],[85],[95], heart failure and hypertension [108],[181],[28], renal failure [105], impaired bone development and muscle atrophy [12],[107],[20], and cancer [77]. While RACK1 expression imbalance is associated with disease, in many cases it is difficult to clearly predict the role that it plays in the development of these pathological states. For example, decreased RACK1 expression is reported in post-mortem brains of Alzheimer's disease patients and is implicated in dementia development [4],[5],[83],[185]. However, no such changes were reported by Shimohama et al. (2011) [83], which found no difference between the levels of RACK1

in Alzheimer's patients and age-matched controls [83]. One of the most pertinent examples of how unpredictable RACK1 signaling can present in disease is its association with cancer. A review of RACK1 expression in cancer tissues found dysregulation but no concrete association between cancer types and RACK1 expression [77]. For example, in a study conducted in breast cancer, the clinical significance of RACK1 expression was evaluated using immunohistochemistry [17]. Higher RACK1 expression levels were correlated with shorter survival times, and revealed that RACK1 could promote breast carcinoma proliferation and invasion/metastasis *in vitro* and *in vivo*, supporting the conclusion that elevated RACK1 expression could predict poor clinical outcomes [18]. In contrast, when RACK1 expression in breast cancer tissues was examined in a separate study using reverse transcriptase–PCR (RT-PCR), it was found that RACK1 expression levels were decreased in cancer specimens compared to normal breast tissues [2]. In a follow-up study performed a decade later, high levels of RACK1 mRNA expression were associated with a good clinical outcome [2]. As described in Section 1.2, the unique nature of RACK1's adaptable approach to scaffolding is likely to blame for the inconsistent reports of RACK1 expression in disease states, which further stresses the importance of achieving a better understanding of how RACK1 functions in systems biology.

1.2 Mitochondria and RACK1 connections

1.2.1 A snapshot of mitochondrial roles within the cell

Mitochondria are multi-functional organelles that exist in a comprehensive network responsible for a majority of the essential eukaryotic cellular functions reviewed in [9],[104],[142],[37]. They are commonly termed the 'powerhouses of the cell' due to their well-recognized energy production role, where they oxidize organic substrates under aerobic conditions via respiration to produce energy for the cell [9],[104],[93],[142],[37]. Although energy production is the most well-recognized role, mitochondria are integral to normal cellular function in many other ways. This includes roles in cell growth, redox status, synthesis of phospholipids and heme, ion balance, programmed cell death mechanisms (including apoptosis, necroptosis, pyroptosis, ferroptosis, and autophagy) and non-programmed (necrotic) cell death mechanisms [104]. The major

areas of mitochondrial function that will be explored below include: mitochondrial network dynamics, including biogenesis, fusion, and fission; energy production, including cellular oxygen consumption and cellular ATP production; and mitochondrial integrity, including mitochondrial (mt)-DNA management and mitochondrial ribosomal production.

Mitochondria history and structure

Mitochondrial are unique amongst other eukaryotic organelles in both structure and origin [93],[21]. It is theorized that they have a bacterial evolutionary origin, where an alphaproteobacterial endosymbiont entered a proto-eukaryotic host (reviewed in [21]). The ability of this bacterium to efficiently produce energy is what likely resulted in endosymbiosis between the two, transforming the mitochondria into a eukaryotic organelle [21],[90],[91],[49]. However, mitochondria still retain some of their ancient bacterial characteristics. They are the only organelle to have a unique double-membraned structure that separates four distinct compartments: the outer membrane, intermembrane space, inner membrane, and the matrix [7]. In addition, they have their own heteroplasmic circular genome and divide using binary fission, both of which occur independently of the eukaryotic cell cycle [93].

Mitochondrial dynamics

A healthy cell depends upon the careful regulation of its mitochondrial mass to meet the energy demands vital for cellular function. To achieve this goal, mitochondria continuously undergo a cycle of biogenesis, fission, fusion, and mitophagy within the cell (reviewed in [167]). Mitochondrial biogenesis occurs when mitochondria are produced via binary fission (Figure 5.2). Once independent, mitochondria undergo morphological maintenance via the opposing processes of fusion and fission (Figure 5.3) [167],[157],[58]. Mitochondrial fusion ensures uniform mitochondrial content (i.e. mt-DNA), buffers against calcium and reactive oxygen species (ROS) overload, and maximizes the surface area required for energy production via respiration ([58]). Mitochondrial fission is essential for cell growth and division, sustaining cell polarity, and aiding in eliminating damaged mitochondria [157]. When damaged mitochondria are removed via fission, this signals the process of mitophagy

to begin, which removes damaged/defective mitochondria through autophagy [167]. The activation of the master regulator of mitochondrial biogenesis, the peroxisome proliferator-activated receptor-γ coactivator (PGC1α) will begin mitochondrial biogenesis [153],[166],[128],[56]. PGC1α activity upregulates expression of mitochondrial transcription factor A (TFAM) which drives mt-DNA transcription and replication, resulting in a cascade of nuclear and mitochondrial activity that increases mitochondrial biogenesis (Figure 5.2) [14],[15],[170]. The new mitochondrion must now fuse both membranes to other mitochondria. Outer membrane fusion is controlled by two large membrane GTPase proteins, Mitofusin 1 (MFN1) and Mitofusin 2 (MFN2), whereas inner membrane fusion is controlled by Optic atrophy 1 (OPA1) (Figure 5.3). This creates a homogenous organelle population while simultaneously decreasing cellular stress. When fission is required, the Dynamin related protein 1 (Drp1) acts in concert with a small array of support proteins that drive separation of the defective mitochondrion from the network. Fission is typically associated with the process of mitophagy, where dysfunctional mitochondria are selectively eliminated by autophagy. Mitophagy is a central mechanism of mitochondrial quality control, as the timely elimination of damaged and aged mitochondria is essential for maintaining mitochondrial network health [167],[157],[158]. During mitophagy, mitochondria are sequestered within an autophagosome, which will fuse with a lysosome, where the organelle is hydrolytically degraded. The balance of biogenesis, fission, fusion, and mitophagy creates a steady state of mitochondrial morphology, mt-DNA mixing, and bioenergetic functionality [167].

Mitochondrial bioenergetics

Mitochondrial dynamics support cellular function by shifting mitochondrial morphology to meet energy requirements [142],[37]. Mitochondria form massive networks that favor fusion to maximize the number of respiratory complexes that can produce energy [158],[96]. Mitochondrial respiration then drives the synthesis of adenosine triphosphate (ATP) in the cell. ATP is used in turn as the primary energy source for most biochemical and physiological processes [144]. Mitochondria use a well-recognized process to convert pyruvate to ATP (reviewed thoroughly in [144] and [87]) and will only be briefly summarized here: first, sugars enter the mitochondria

as pyruvate after undergoing glycolysis in the cytosol. In the citric acid cycle, a series of eight regenerating enzymatic steps, pyruvate is converted to oxaloacetate, with the electrons removed in the process passed to the electron-carrying cofactors. Oxidative phosphorylation (OXPHOS) will then occur when the cofactors pass these electrons to the ETC. The ETC consists of four multi-subunit protein complexes (NADH: ubiquinone oxidoreductase (complex I), succinate dehydrogenase (complex II), ubiquinol–cytochrome c oxidoreductase (complex III, or cytochrome bc1 complex), and cytochrome c oxidase (complex IV) embedded in the inner mitochondrial membrane. Here, the complexes use the electrons to power the pumping of protons from the matrix to the intermembrane space, generating a potential difference across the inner mitochondrial membrane. This potential difference is ultimately used to power the synthesis of ATP through activity of final ETC member ATP synthase (complex V), which couples electron passage across the membrane to the phosphorylation of adenosine diphosphate (ADP) [144],[87]. By understanding how the mitochondrial structure is utilized to produce energy, it becomes clear how mitochondrial bioenergetics are strongly interdependent on mitochondrial morphology. Changes in bioenergetic demand, such as increased energy demand, will often result in changes in mitochondrial morphology as the network adapts to increase inner membrane capacity for ETC components, corresponding with increased oxygen consumption [87].

Mitochondrial genomics

As noted earlier, mitochondria possess circular genomes resembling bacterial chromosomes (Figure 5.4) [136]. The double-stranded, circular mt-DNA is around 16.5 kilobases in size and is maintained by mitochondrial enzymes that perform synthesis and repair (Figure 5.4) [136],[97]. mt-DNA is required for production of key catalytic sub-units of the mitochondrial respiratory chain complexes and therefore is essential for oxidative ATP production [155],[126]. The mitochondrial genome encodes 37 genes: 13 structural genes encoding subunits of oxidative phosphorylation complexes in the mitochondrial respiratory chain (MT-ATP6, MT-ATP8, MT-CO1, MT-CO2, MT-CO3, MT-CYB, MT-ND1, MT-ND2, MT-ND3, MT-ND4, MT-ND4L, MT-ND5, MT-ND6), 22 transport RNAs (tRNAs), and 2 ribosomal RNAs (rRNAs) (Figure

5.4) [155],[126],[10],[13],[159],[16]. These genes are transcribed by mammalian mitochondrial ribosomes, which are specialized ribosomes that are encoded by nuclear genes, synthesized in the cytoplasm, and then transported to the mitochondria to be assembled into mitochondrial ribosomes [55]. Like bacterial chromosomes, multiple copies of mt-DNA exist in a single mitochondria. However, due to a combined lack of protective histones, ROS generation in the inner membrane from ETC activity, and its lack of genomic repair mechanisms, mt-DNA has an increased susceptibility to damaging mutations [10],[13],[159],[16]. Mitochondria minimize the influence of these mutations by blocking them from forming a new subset of mitochondria. This is achieved by fusion, which supports mt-DNA "mixing" while lowers damaging ROS concentrations that may have initially contributed to the mt-DNA mutations [16]. Additional to its role in encoding ETC components, mt-DNA also acts as a key signaling component within the mitochondrial biogenesis cascade [56],[158],[16]. These additional features illustrate the consistent theme of interconnectivity between the players mediating mitochondrial form and function.

1.2.2 Mitochondrial role in disease

In a healthy cell, cellular and mitochondrial metabolisms are tightly coupled and a loss of efficient interplay between these two systems can devastate cellular function [127],[73]. Mitochondrial dysfunction has been found to influence the pathogenesis and progression of numerous human diseases, including heritable mitochondrial disease [111], cancer [127],[73],[111], neurodegenerative, musculoskeletal, and cardiovascular disorders [127],[73], metabolic disorders [126], and autoimmune diseases [127]. Mitochondrial dysfunction in literature is broadly described as resulting from either the inability to provide necessary substrates to mitochondria, a dysfunction in respiration equipment, or inadequate mitochondrial mass for cellular needs [127]. This dysfunction can be either the result of heritable mutations or increased environmental stressors in cells over time [127]. For example, an expanding number of degenerative disorders are associated with direct mutations in the nuclear genes encoding fusion mediators or mt-DNA maintenance proteins: mutations in *MFN2* and *OPA1* are linked to Charcot–Marie–Tooth disease type 2A and autosomal dominant optic atrophy [116],[25], and early onset Parkinson's disease is linked to loss of ETC complex 1

function due to *PINK1* mutations [44]. In contrast, environmental stressors such as pollution, infection, tissue injury, or aging may cause an increase in oxidative mitochondrial damage and unresponsive mt-DNA repair mechanisms which trigger mitochondrial fragmentation and reduce mt-DNA. This kind of stress initiates a vicious cycle wherein oxidative stress will perpetually increase due to the inefficient synthesis of proteins of the respiratory complexes from mt-DNA decrease [57], which produces chronic inflammation that is linked to metabolic diseases such as diabetes, cancer and cardiovascular disorders [57]. The shifts in mt-DNA homeostasis are gaining increased interest as potential prognostic markers for cancer and metabolic diseases including heart failure, diabetes, and autoimmune diseases such as lupus [110],[163]. For example, Guha et al. (2014) [51], demonstrated breast cancer stem cells carried steeply reduced mt-DNA copy numbers. This was further echoed by a similar dysregulation of mt-DNA content reported in prostate, colorectal, lymphedema, and other breast cancers, with both increases and decreases reported in comparison to a control [61],[135]. However, these conflicting reports on whether levels shift up or down remain to be resolved before mt-DNA-based health predictions are standardized [163]. In spite of the promising clinical connections between mitochondrial and organismal health, the causative agents of mitochondrial dysfunction remain poorly understood. Historical interest in mitochondria as a therapeutic target for the treatment of a broad spectrum of human diseases has previously resulted in numerous preclinical studies that demonstrated beneficial effects of various pharmacological agents that supported mitochondrial health. However, no single mitochondria-targeted compound has been approved for clinical use because the precise mechanisms used by mitochondria to regulate basic physiological functions remain unknown [81]. To further complicate how mitochondria signaling and disease intertwine, multiple defects in mitochondrial function are identified in disease states, making it difficult to ascertain which pathway to target for therapeutic advancement [73],[81]. For example, both mitochondrial ETC dysfunction and severe shifts in the pathways mediating mitochondrial morphology are widely implicated in the cellular pathogenesis and progression of most common neurodegenerative diseases including Alzheimer's, Parkinson's disease, Amyotrophic lateral sclerosis, and neurodevelopmental regression syndromes such as Leigh syndrome [116]. In summary, progress on defining the mitochondrial impact on disease

is hindered by a lack of in-depth knowledge of both the regulatory mechanisms of mitochondrial physiology and the interplay between mitochondria and cellular pathways that contribute to support of optimal cellular function.

1.2.3 Documented RACK1 interactions with mitochondria

RACK1 and the mitochondrion both represent multifunctional cellular entities with numerous roles in maintenance of cellular health [162],[127]. Despite their overlapping impacts on cellular maintenance and organismal disease, there has been little investigation in the RACK1 biology realm on how RACK1 expression impacts mitochondrial physiology. It is established that RACK1 can enter the mitochondrion: Lin et al. (2015) [81], showed that RACK1 is able to enter the mitochondrion and associate with mitochondrial proteins in chicken embryo fibroblasts. Beyond this observation, RACK1 biology currently lacks a mitochondrial characterization in cells experiencing alterations in RACK1 homeostasis. This is likely in part due to the incredible range and diversity of supportive roles that both entities play in cellular homeostasis, which has historically made complete identification of the influence of both RACK1 and mitochondrial interactomes difficult. However, RACK1 has been found to indirectly impact mitochondrial function in apoptosis and ribosome associated- studies, which has provided some characterization of the RACK1 and mitochondrial-associated proteins (MAPs) pathway interactions. These are summarized below.

RACK1 and apoptotic signaling

In general, our current understanding of how RACK1 expression impacts mitochondrial physiology is limited to how RACK1 interacts with closely associated mitochondrial molecular players. Most of the research that indirectly surveys how RACK1 signaling impacts mitochondria function has resulted from investigating RACK1's association with intrinsic pathway apoptosis mediators. RACK1 has been shown to interact with several pro-apoptotic proteins and can mediate mitochondrial membrane potential and apoptosis triggers through this path. Zhang et al. (2008) [182] demonstrated that RACK1 formed a complex with pro-apoptotic protein Bcl-2 Interacting Mediator of cell death (Bim) in the presence of apoptotic stimulants. Bim, a member of the B-cell lymphoma-2 (Bcl-2) family, will translocate to the mitochondrial outer

membrane where it can either block anti-apoptotic Bcl-2 proteins, including Bcl-2 or B-cell lymphoma-xL (Bcl-xL), or directly activate pro-apoptotic proteins, such as Bcl-2 Associated X-protein (Bax). Hence RACK1 was found to help mediate the degradation of Bim, protecting cancer cells from apoptosis [182]. This protective effect was also found in cells impacted by Gumboro disease, a viral infection impacting poultry [81]. During infection, the viral protein VP5 induces apoptosis during infection by interacting with VDAC2, a mitochondrial channel capable of pore formation in the mitochondrial outer membrane, resulting in release of cytochrome c, activation of caspases 9 and 3, apoptosis and virus release. Lin et al. (2015) [81] found that RACK1 played an antiviral role where it formed a complex with both VDAC2 and VP5 that appeared to block apoptosis in host cells. Subsequent knockdown of RACK1 induced apoptosis associated with activation of caspases 9 and 3, suggesting that RACK1 plays a role in protecting the cell against apoptosis in viral infection [81]. Contrastingly, RACK1 has been additionally identified as a separate binding partner of Bax [171], and Bcl-XL. Overexpression of RACK1 dissociated the Bax/Bcl-XL complex and promoted Bax oligomerization, which promoted apoptosis [171]. This was supported by the findings of [88], who demonstrated that RACK1 indirectly regulated expression of several Bcl-2 family members through suppression of the Akt pathway via inhibition of Src. Src-inactivation induced the expression and subsequent translocation of pro-apoptotic Bax and Bim to the mitochondrial membrane, resulting in mitochondrial-mediated apoptosis [88]. Further interactions of RACK1 with mitochondrial apoptotic pathways have shown that the pro-apoptotic tumor suppressor molecule Modulator of apoptosis 1 (MOAP-1) is activated by RACK1, through RACK1-supported ubiquitination that allows the formation of a complex that includes a MOAP-1/Bax association [72]. This triggers a Bax conformational change that results in its insertion into the mitochondrial membrane and several further hallmark events that execute death receptor-dependent apoptosis [72]. The final apoptosis-RACK1 interaction that involves MAPs has very recently been identified in Parkinson's disease [86]. Parkinson disease protein 7 (DJ-1) exerts neuroprotective effects by inhibiting the expression of the enzyme Monoamine oxidase-B (MAO-B). MAO-B is distributed at the mitochondrial outer membrane where it blocks neurotransmitter activity by converting them to highly reactive oxygen species. This can

contribute to ROS generation, mitochondrial dysfunction, and eventually apoptosis in highly stressful environments [86]. It appears that a DJ-1-RACK1 complex forms to protect neurons from mitochondrial oxidative stress-induced apoptosis. In a slight twist on the usual RACK1 interaction style, DJ-1 appears to bind to RACK1 and prevent it from activating the PKC-mediated cascade that is required for up-regulated MAO-B activity, which protects against oxidative stress that would otherwise lead to apoptosis [86]. This suggests that RACK1 may be involved in triggering mitochondrial oxidative stress-induced apoptosis.

One of the most intriguing connections between RACK1 function and mitochondrial function has been presented by [150] who found that cells with the loss of Asc1, the RACK1 homologue in yeast, were unable to use alternative carbon sources that required enhanced mitochondrial function. RNA-seq analysis revealed that cells with decreased Asc1 experienced a concomitant decrease in the expression of mitochondrial ribosomal proteins (MRPs), resulting in a compromised translation of MRPs. Thompson et al. (2016) [148] suggested Asc1's role in the yeast ribosome may hinder translation of the mitochondrial proteins as their mRNAs may have translational features that require Asc1 activity [150].

RACK1 and mitochondrial structure

There is some limited ultra- structural information available of mitochondria experiencing RACK1 dysfunction. In an investigation focused on RACK1 interaction with autophagy, Zhao et al. (2015) [184] discovered that a hepatocyte-specific RACK1 deficiency led to smaller mitochondria in those cells. Fasting in these affected cells resulted in mitochondrial swelling. While transmission electron microscopy (TEM) images seen in this study taken somewhat reveal mitochondrial form, no direct investigation of the mitochondrial ultrastructure was undertaken in this study [150].

1.3 Rationale, hypothesis, and goals of this project

Rationale: investigation of the RACK1-mitochondrial connection will provide valuable context to the regulatory roles of cellular RACK1

Deciphering the RACK1 interaction network is crucial for understanding the cellular processes that are regulated by the scaffolding protein and will further facilitate our understanding of RACK1 involvement in disease states. Unfortunately, minimal characterization of mitochondria within cells experiencing aberrant RACK1 signaling exists. While the studies above have suggested that RACK1 signaling influences mitochondrial health, the current nomenclature lacks a more comprehensive review of the mitochondrial structure and function in a RACK1-depleted cell. Therefore, the goal of this project is to determine how a decrease in cellular RACK1 expression impacts mitochondrial physiology and function. This study builds upon the observations made in earlier preliminary research completed in the Cheng lab investigating the impact of RACK1 depletion on mitochondrial activity: RNA-seq analysis of RACK1 knockdown (KD) cells revealed a significant decrease in the expression of mitochondrial MRPL and MRPS (mitochondrial large sub-unit protein (MRPL), mitochondrial small sub-unit protein (MRPS)) genes after knockdown. Despite the down-regulation of MRPS, when mitochondria in RACK1 KD cells were subsequently visualized using microscopy, RACK1 KD cells appeared to be filled with more mitochondria compared to a control. These findings represent a dichotomy within the cells that formed the basis for this investigation. To increase HeLa cell dependence on mitochondrial function, we decided to perform RACK1 KD on HeLa cells in two glucose conditions, (both 'high glucose', or HG and 'low glucose', or LG). By broadening our understanding of the interplay between RACK1 signaling and mitochondrial function, this study will provide greater insight into how RACK1 signaling impacts cellular pathology and influences the initiation and progression of disease.

Hypothesis

RACK1 knockdown causes dysregulation of mitochondrial form and function in the cell.

Aims of the project

This study consists of three major goals:

1. Assess the impact of RACK1 KD on HeLa cell morphology and growth parameters.

2. Characterize mitochondrial morphology and dynamics in RACK1 KD cells.

3. Characterize mitochondrial biogenesis and functionality in RACK1 KD cells.

Chapter 2

Methods

2.1 Mammalian Cell Line Maintenance and Transfection Conditions

2.1.1 Cell lines and growth conditions

HeLa cells (Human cervical carcinoma cell line) were obtained from the American Type Culture Collection (ATCC®, Cat. No. CCL-2) and grown in monolayer cultures were maintained in an incubator at 37 ^{o}C in 5% atmospheric CO_2. Cells were cultivated in Dulbecco's Modified Eagle Medium (DMEM), high glucose (Wisent, Cat. No. 319-005-CL) supplemented with 10% heat-inactivated fetal bovine serum (FBS) (Wisent, Cat. No. 080450) and 1uM L-glutamine (Wisent, Cat. No. 609-065-EL). Cells were sub-cultured by trypsinization at 37 ^{o}C and cell suspensions were subsequently diluted to the desired cell density in fresh medium. Cells were not passaged more than 9-12 times to maintain experimental consistency and avoid changes in mitochondrial function, at which time they would be discarded and a new culture would be started from pre-prepared frozen aliquots.

2.1.2 siRNA transfection

To knockdown RACK1 expression in HeLa cells, we utilized both an ON-TARGETplus human RACK1 SMARTpool siRNA library (Dharmacon, Cat. No. L-006876-00-0050), and an ON-TARGETplus Non-targeting Control 1# siRNA library (Dharmacon, Cat. No. D-001810-01-50) and followed the manufacterer's recommended DharmaFECT™ Transfection Reagents—siRNA transfection protocol. Briefly, twenty-four hours before transfection, 1.2x105 cells at maximum confluency grown in the conditions above were plated in DMEM/FBS medium in a 6-well plate at 37^{o}C in 5% atmospheric CO_2. On the day of transfection, the RACK1 siRNA pool or nontargeting siRNA pool were diluted 1:100 and DharmaFECT 1 Transfection Reagent (Dharmacon, Cat. No. T-2001-03) diluted 1:50 in DMEM with no additives. The solutions

were incubated for 5 minutes at room temperature before the dharmaFECT/DMEM solution was split equally between the siRNA/FBS mixtures, combined, and incubated for a further 20 minutes at room temperature. The diluted transfection mixtures were further diluted 1:4 with DMEM/FBS for a final siRNA concentration of 25 nM. Cells were incubated with the transfection mixture at 37^{o}C with 5% CO_2 for 24 hours until the transfection/media mixture was replaced with fresh DMEM/FBS medium and incubated a further 48 hours. Low-glucose experiments followed the protocol seen above wherein cells were initially plated in high-glucose medium overnight until transfection was performed. Then transfection reagents and RNAi were combined with low glucose (1g/L) DMEM (Wisent Cat. No. 319-010-CL) as detailed above that was further diluted with low glucose DMEM supplemented as seen above in the high glucose medium. For experimental consistency, transfection in high and low glucose media were performed at the same time and RACK1 KD and control cells from both medium conditions were simultaneously used in experiments at 72 h post-transfection unless otherwise noted. siRNA knockdown of RACK1 expression in each sample set was confirmed through western blot analysis. Before commencing experiments, RACK1 expression in cells was knocked down for 8 days and confirmed with both reverse transcription quantitative real-time PCR (RT-qPCR) and western blot analysis to ensure strong and consistent knockdown that would meet the 72 hour post-knockdown timeline.

2.2 SDS-PAGE and Western blotting

2.2.1 Preparation of whole-cell lysates

At the completion of each knockdown sequence as detailed above, cells from each condition were harvested via trypsinization and washed twice with PBS (Wisent, Cat. No. 311-010-CL) before 200 μL of ice-cold lysis buffer (2% Sodium dodecyl sulfate (SDS) w/v, 50mM Tris/HCl pH 7.4, 1mm EDTA) were added per well in a 6-well plate (adjusted to 200 μL per million cells in alternate plate sizes). After 10 minutes of incubation on ice, lysates were stored at -20^{o}C until further use. Cell lysates were sonicated for 30 seconds at 40 watts (Sonics & Materials, Ultrasonic Processor VC50-1) and cleaned of debris via centrifugation at 15,000xg for 30 seconds at room

temperature. An aliquot of the resulting supernatant was removed for donwstream processing and remaining lysate stored at -20 ^{o}C.

2.2.2 Protein quantification and sample preparation

Protein concentration was quantified using the Pierce BCA Protein Assay Kit (Thermo Fisher Scientific, Cat. No. 23225) following the manufacturer's instructions. Briefly, samples were diluted to 1:4 with distilled water (dH_2O). Triplicate sets of each diluted sample and duplicate sets of bovine serum albumin (BSA) standards (with previously prepared concentrations ranging from 0 μg/mL (pure dH_2O) to 2000 μg/mL) were mixed 1:15 with working reagent, and the microplate was incubated at 37 ^{o}C for 30 minutes. Absorbance at 562 nm was measured on a microplate reader for 1 minute (MBI, Asys UVM 340). The protein concentration of each sample was calculated using the BSA standard curve. Samples for electrophoresis were prepared by mixing samples with 5X-SDS-polyacrylamide gel electrophoresis (SDS-PAGE) Loading buffer (0.25 M Tris-HCl pH 6.8, 50% glycerol, 10% SDS, bromophenol blue 0.25% w/v) and lysis buffer to equilibrate concentration across all samples. Samples were heated at 95 ^{o}C for 5 minutes in a thermoblock (Standard Heatblock, VWR).

2.2.3 SDS-PAGE

Polyacrylamide gels (4% stacking gel and a 12% resolving gel) were placed into an electrophoretic chamber (Bio-Rad, Cat. No. 1658004EDU) filled with 1X running buffer (25mM Tris, 250mM glycine, 0.1% SDS). Between 15 μg to 30 μg of protein (depending on total protein content) were loaded into separate wells along with 3 μL of protein ladder (Bio-Rad, Cat. No. 161-0393 or 161-0394) diluted in dH_2O to match the final volume loaded into respective wells. Proteins were separated first at 80 V (Bio-Rad PowerPac Basic Power Supply, Cat. No. 164-5050) for 15-20 minutes, and then at 120 V for 1.5 hours or until adequate band separation was achieved. After electrophoresis, the gel was prepared for western blotting analysis.

2.2.4 Western blotting and relative protein expression quantification

Gels were equilibrated using 1x transfer buffer (25 mM Tris, 192 mM glycine) with 20% methanol before proteins were transferred to 95% ethanol-activated polyvinylidene fluoride membrane (PVDF) (Bio-Rad, Cat. No.10600023) using the Trans-Blot® Turbo™ Transfer System (Bio-Rad, Cat. No. 1704150). Following protein transfer, PVDF membranes were removed from the cassette then blocked for 1 hour using 5% skimmed milk powder diluted in Tris Buffered Saline with Tween 20 (TBST) (Fisher, Cat. No. BP337-500) (TBST - 50 mM Tris-HCl pH 7.4, 150mM NaCl, with 0.1% v/v Tween 20), followed by a 2 hour incubation at 4^{o}C with primary antibody (diluted in 5% skimmed milk powder in TBST), then finally incubated with the corresponding secondary horseradish peroxidase (HRP) HRP-bound antibodies (diluted in 5% skimmed milk powder in TBST) for 1 hour. All antibodies used in this project are detailed in Table 2.1. Proteins were detected using 0.5 mL of luminol-based Clarity Western ECL Substrate (Bio-Rad, Cat. No. 1705062) and Chemiluminescence detection was performed using a ChemiDoc Imaging System (Bio-Rad, Cat. No. 12003153).

Table 2.1: List of antibodies used for western blotting

Name	**Dilution factor**, **Western Blotting**	**Company**, **Category**
Anti-Actin-HRP	1:5000	Santa Cruz Biotech, sc-47778
Anti-GAPDH-HRP	1:5000	Santa Cruz Biotech, sc-47724
Anti-mouse-HRP	1:5000	Bio-Rad, 170-5047
Anti-RACK1	1:1000	Santa Cruz Biotech, sc-17754

2.3 Molecular biology techniques

2.3.1 RNA extraction

Total RNA was extracted by lysing the cells using Trizol-Chloroform-Isopropanol method (TRIzol reagent; Ambion, 15596026) as per manufacturer's instructions. Extracted RNA was DNase treated using the DNA-free Kit Dnase Treatment & Removal (Invitrogen, AM1906) as per manufacturer's instructions. RNA concentrations were measured using a NanoDrop™ spectrophotometer (Thermo Fisher Scientific, Cat. No.

NDONEC-W). One microgram of RNA per sample was reverse transcribed using the iScript RT Supermix for RT-qPCR(BioRad, Cat. No 1708841) in a T100™ thermal cycler (Biometra, T1) at [25^{o}C for 5 min, 46^{o}C for 20 min, 95^{o}C for 1 min, 12^{o}C hold].

2.3.2 Primer design and validation

Primers were designed for mitochondrial fusion mediators *MFN1*, *MFN2*, and *OPA1, PGC1α, TFAM,* and mitochondrial fission mediator dynamin 1-like protein Drp1 *(DNM1L)*. The oligonucleotides used as genomic PCR primers were designed using the PrimerQuest™ Tool (© 2023 Integrated DNA Technologies, Inc.) ordered from Integrated DNA Technologies, Inc. and primer specificity verified using Primer-BLAST [179], to ensure no homology to unexpected genomic targets was detected. All genomic primer sequences used in this project are specified in Table 2.2. PCR primers were re-suspended in nuclease-free water (Invitrogen, Cat. No. 10977-015) to a concentration of 100 μM (frozen stock) and then diluted further to 10 μM for primer working solutions.

The efficiencies of the genomic primers over temperature and concentration gradients in this project were verified prior to RT-qPCR commencement. Primer efficiency was tested using pooled cDNA from the four experimental sample types as a template, where it was serially diluted from 10^2 ng/μL/reaction to 10^{-2} ng/μL/reaction. The qPCR reaction contained 10 μL of SsoAdvanced Universal SYBR Green Supermix (BioRad, Cat. No. 1725274), 1 μL of each forward and reverse primers and 8 μL of cDNA template (diluted to the correct volume and 10^2 ng/μL reaction concentration using ultrapure H_2O). RT-qPCR was performed using the CFX96 Touch Real-Time PCR system (Bio-Rad, Cat. No. 45933) at [95^{o}C for 3 minutes, 44 cycles [95^{o}C for 20 seconds, 59^{o}C for 30 seconds, 72^{o}C for 30 seconds], and completed with a melting curve analysis [65^{o}C to 95^{o}C increment 0.5^{o}C for 5 seconds]] at the conclusion of the cycles. Primer efficiency was calculated using this formula: Amplification efficiency (%) = [10(-1/m)] -1 x 100, where m is the slope of the trend line.

All primers were verified to have specificity over 90% to continue to experimental RT-qPCR.

Table 2.2: List of primers used for RT-qPCR

Nuclear gene target	Primer sequence (5' to 3')
OPA1	**F:** GAGGACAGCTTGAGGGTTATTC **R:** GTTCTTCCGGACTGTGGTTATT
MFN1	**F:** CAGACCACAGTAAGTGGGATTAG **R:** GTTTGGGAGGCTGAGGTAAA
MFN2	**F:**CCAAGTGCCCTGGACTAAAT **R:**GGTCTCTCCCTCAGTGGTATAA
DNML1	**F:** CGCAGAACCCTAGCTGTAATC **R:** AATTCTAGCACCACCGCATAG
TFAM	**F:** GGCAAGTTGTCCAAAGAAACC **R:** GCATCTGGGTTCTGAGCTTTA
PGC1α	**F:** GAGTCAAAGTCGCTGGCATC **R:** AACTATCTCGCTGACACGCA
β-actin	**F:** TCCCTGGAGAAGAGCTACGA **R:** AGCACTGTGTTGGCGTACAG

2.3.3 Real-time quantitative PCR reactions and fold change analysis

The synthesized cDNA was prepared for RT-qPCR using the SsoAdvanced Universal SYBR Green Supermix (BioRad, Cat. No. 1725274) following manufacturer's instructions. Each 20 μL PCR reaction consisted of 10 μL of SYBR Green Supermix, 8 μL of template cDNA-dH_2O, and one μL of each primer working solution. RT-qPCR was performed using a CFX96 real-time PCR machine (Bio-Rad, Cat. No. BR006412) at [95^{o}C for 3 minutes, 95^{o}C for 10 seconds, 55^{o}C for 30 seconds, repeated for 39 cycles]. Fold change in genetic expression was calculated using the ΔCt method and gene expression values were normalized to β-actin. Each sample was run in duplicate, with 3 separate experimental replicates for each gene target.

2.4 Microscopy methods

2.4.1 Transmission electron microscopy

The morphological changes of cells and their respective mitochondria were observed following RACK1 knockdown and control scrambled knockdown. Seventy-two hours post knockdown, samples were centrifuged (1,000 rpm, 5 minutes, 22^{o}C), and pellets washed twice with PBS. Pellets were then fixed according to Wijesundara et al. (2022) [169] with 2.5% glutaraldehyde (Millipore Sigma, Cat. No. G5882) in 0.1 M sodium

cacodylate trihydrate buffer (Millipore Sigma, Cat.No. C4945) (25% Glutaraldehyde: 0.1 M sodium cacodylate trihydrate buffer (1:9)) for 2 hours at 22^{o}C. The fixed cells were pelleted (1,000 $\times$ g, 10 min, 22^{o}C) and washed with 0.1 M sodium cacodylate trihydrate buffer. This step was repeated three times before cells were fixed with 1% (w/v) osmium tetroxide (in 0.1 M cacodylate buffer) for 4 hours at room temperature. Rewashed cells were placed in 0.25% Uranyl Acetate at 4 ^{o}C overnight before being dehydrated with a graduated series of acetone (50%, 70%, 95%, and 100%). Dried samples were infiltrated with an Acetone/Epon Araldite resin solution (1964, Electron microscopy sciences, Hatfield, PA, USA) (3x Dried 100% Acetone: 1X Epon Araldite Resin for 3 hours, then 1x Dried 100% Acetone: 3X Epon Araldite Resin overnight, then 100% Epon Araldite Resin for 2x 3 hours) before being embedded in 100% Epon Araldite Resin and hardened for 48 hours in a 60 ^{o}C oven. Thin sections were cut using a microtome (Reichert-Jung Ultracut E Ultramicrotome, EquipNet Inc., Canton, MA, USA) with a diamond knife (approximately 100 nm thin) and were placed on 300 mesh copper grids, which were then stained (2% aqueous uranyl acetate stain for 10 minutes, distilled water rinse for 2 $\times$ 5 minutes, lead citrate stain for 4 minutes, brief distilled water rinse) before being air dried. Samples were observed using a Transmission Electron microscope (JEM 1230, JEOL Inc., Peabody, MA, USA) at 80 kV at 4X, 8X, 15X, 40X, 80X, and 100X magnifications. Images were captured using a digital camera (ORCA-HR, Hamamatsu Photonics, Japan). Three replicates of the four conditions were completed and 10 cells were gathered from each condition per replicate. The gross morphological characteristic of the cells and their respective mitochondria was analyzed using the methods described by Lam et al. (2021) [71] using ImageJ software [129] to determine average mitochondrial length, width, and area per condition. To determine the number of mitochondrial present per panel, total mitochondrial counts were normalized to the total area/cell for each panel using ImageJ, then averaged. Finally, gross mitochondrial morphology between conditions was assessed using the following three parameters: 1) Mitochondrial membrane rupture, characterized as a distinct loss of both membranes in plane; 2) Loss of cristae, characterized as a lack of visible cristae in a mitochondrion with both membranes fully in-plane; and 3) presence of mitochondrial inclusions, characterized by the presence of black granular structure within the double membrane of a mitochondrion. The average number

of morphological incidences present in each set of conditions was averaged by each hundred mitochondria previously counted in those panels.

2.4.2 Confocal detection of live mitochondrial networks

Cells were plated on glass coverslips (18 mm diameter, 0.16 - 0.19 mm thickness) (Avantor, Cat. No. 72222-01) in 6-well plates using the plating and subsequent knockdown method used in sections 2.1.1 and 2.1.2. Seventy-two hours post-knockdown, the medium on the cells was removed and replaced with 400 nM MitoTracker™ CMXRos (Invitrogen, Cat. No. M7512) suspended in high or low glucose DMEM that was prepared as shown previously in section 2.1.1 and 2.1.2. Cells were stained for 45 minutes, gently rinsed in 1X PBS three times to remove free dye, and incubated in clear imaging medium FluoroBrite DMEM (Thermofisher, Cat. No. A1896701) supplemented with 10% FBS and 1μM L-glutamine during live cell imaging.

The cells were examined under a Leica TCS SP8 LIGHTNING confocal laser microscope (Leica Microsystem, Germany) using incubation control at 37 ^{o}C and 5% CO_2. Images were collected on the Leica 93× /1.30 glycerol objective (pinhole of 0.6 Airy units, numerical aperture of 1.3). The mitochondrial networks were visualized using 578-nm laser excitation at 0.75% laser intensity and a hybrid detector (HyD) hybrid detector set to a 588- to 680-nm detection window with time gating between 0.3 and 6 nanoseconds. Z-stacks were taken of whole cells in lightning with Pixel size (x, y) and z-spacing were adjusted as per the calculated optimal Nyquist sampling parameters. Bidirectional scanning was enabled, and all images were acquired using at least two frame averages. Laser power, detector filtering/gating, and gain were adjusted to maximize signal without saturation while also minimizing background signal, cross-fluorescence, and photobleaching to extract the highest quality images. Once these settings were selected, they were retained and applied to all image gathering. Images were deconvolved using Leica LIGHTNING deconvolution software and processed with ImarisFile conversion (10.0.0, Bitplane AG, RRID). Mitochondrial networks were quantified by analyzing the network volume using Imaris 10.0.0 software (Bitplane). z-stacks were 3D reconstructed in Imaris and the resulting images were converted to surface renderings. Imaris identifies individual mitochondria and interconnected networks as surfaces; briefly, to create the surfaces of mitochondria,

complete series of Z-stack images were processed using the Surface Creation Wizard, where the surpass object "surface" rendering was assigned using the Fiji Labkit for Pixel Classification software to train the surface thresholding algorithm to select mitochondrial networks using the "Machine Learning Pixel Classification using Labkit and Imaris" protocol described by Imaris Learning center (© Oxford Instruments 2023). The "split touching objects" feature of Imaris software was enabled, and sphericity of every mitochondrion was measured under the "classification" feature. To automate image analysis, parameters for surface rendering were set at the beginning of the analysis for each replicate and the remaining samples were rendered using batch processing where identical parameters and algorithm settings were applied for each cell in the investigated groups. Mitochondrial measurements were then extracted from detailed statistical analysis of each mitochondrial network per cell as generated by the Imaris software using the Z stack size measurements embedded in each image.

Mitochondria were analyzed using the following criteria and methods as Taguchi et al. (2021) [147]. First, mitochondrial counts were performed (n; number of mitochondria/cell nuclei) where mitochondria were assigned a value of 1 regardless of size, i.e. a mitochondrial network with a continuous form would be considered "one" mitochondrion. To characterize the total volume and area of the mitochondria, total mitochondrial volume per cell (μm^3; total mitochondrial volume in a field/the number of cell nuclei), and total mitochondrial surface area/cell (sum of the surface area of networks in a cell/the number of cell nuclei) were determined. To better characterize mitochondrial shape within the cells, the proportion of fragmented mitochondria found between knockdown and control was determined. Mitochondria were divided into three groups by their sphericity indicated by the Imaris software as follows: fragmented, sphericity $\geq$0.451; intermediate, sphericity between 0.450 and 0.311; and filamentous, sphericity $\leq$ 0.310. Proportion (%) of each spherical group was defined by each spherical group's total mitochondrial volume divided by the total mitochondrial volume. For each sample, 10 cells per condition per replicate were analyzed and averaged. Three replicates were completed.

2.5 Mitochondrial DNA analysis

2.5.1 Mitochondrial isolation

Mitochondria were isolated from both knockdown and control cell lines in both glucose conditions concurrently using the Mitochondria Isolation Kit for Cultured Cells (Thermofisher, Cat. No. 89874). Briefly, 2x10^7 cells knocked down 72 hours prior were trypsinized, resuspended in fresh medium, and then centrifuged (1,000 rpm, 2 minutes, 22^{o}C). The pelleted cells then underwent the workflow as outlined by the manufacturer's instructions for Option A: Isolation of Mitochondria using Reagent-based Method (Thermofisher, Cat. No. 89874) at 4^{o}C under sterile conditions.

2.5.2 DNA isolation

Immediately following mitochondrial isolation, mitochondrial DNA (mt-DNA) was extracted from the mitochondrial pellet using the DNeasy Blood & Tissue kit (Qiagen, Cat. No. 69504), according to manufacturer instructions. DNA isolates were eluted in the same volume of sample originally added to the spin column, such that the overall DNA concentration remained constant. The concentration (ng/μL) of mt-DNA extracted from each sample was measured using a NanoDrop™ spectrophotometer (Thermo Fisher Scientific, Cat. No. NDONEC-W). Purified samples were then stored at -20^{o}C until RT-qPCR was performed.

2.5.3 Primers and synthetic oligonucleotides for mitochondrial gene targets

To measure and standardize the amount of mt-DNA present within the knockdown and control cell lines, both synthetic double-stranded oligonucleotide sequences (gBlocks™) and corresponding mitochondrial DNA target-specific primers for each of cytochrome c oxidase (COX I), cytochrome b (CytB), nicotinamide adenine dinucleotide ubiquinone oxidoreductase chain 1 (ND1), nicotinamide adenine dinucleotide ubiquinone oxidoreductase chain 6 (ND6), mitochondrially encoded 12S ribosomal RNA (RNR1), and mitochondrially encoded 16S ribosomal RNA (RNR2) were generated, all of which are shown in Table 2.3 (Integrated DNA technologies).The gblocks and mt-DNA primers for *COX I, CytB, ND1,* and *ND6* were a generous gift from Lauren Westhaver in Dr.

Jeanette Boudreau's lab (Dalhousie University).

gBlocks™ were used to standardize the quantity of mt-DNA (gBlocks Gene Fragments, Integrated DNA Technologies, custom product) for each gene, with each gBlock being based on its respective gene in the consensus sequence for the mitochondrial genome (GenBank; MF737176.1). Following manufacturer's instructions, the gBlock sequences were re-suspended in molecular grade dH_2O to 10 ng/μL, with concentrations verified by a NanoDrop™ before being diluted further using dH_2O to a starting concentration of 1x 10^7 copies/μL using the following equation:

(C) (M) (1 x 10–15 mol/fmol) (Avogadro's number) = copy number/μL

Wherein C is the concentration of the gBlock in ng/μL, and M is the molecular weight in fmol/ng, as provided by the manufacturer for each gBlock.

Primer specificity for human mitochondrial genome targets was verified as described in section 2.3.2 for genomic primers and no homology to unexpected targets was detected. Primers were validated over both temperature and concentration gradients as described in section 2.3.2, using pooled samples of mt-DNA isolated from both RACK1 and control cell types in both glucose conditions and primer efficiency was confirmed to be $\geq$90% for all targets using the formula seen in section 2.3.2.

Table 2.3: Primers and oligonucleotides used for mt-DNA measurement

Mito gene target	**Primer sequence with Citation**	**Oligonucleotide sequence (bolded) for standard curve (5'to 3')**
CytB	**F**: ATGACCCCAATACG-CAAAAT **R**: CGAAGTTTCATCAT-GCGGAG (doi: 10.1038/nature08780)	AAGAACACCA **ATGACCC-CAATACGCAAAAT** TAACC-CCCTAATAAAATTAATTAAC-CGCTCATTCATCGACCTCCC-CACCCCATCCAACAT **CTC-CGCATGATGAAACTTC** GGCTCACTCCT

Continuation of Table 2.3		
Mito gene target	**Primer sequence with Citation**	**Oligonucleotide sequence (bolded) for standard curve (5'to 3')**
COX I	**F**: TCATCTGTAGGCTCATTC **R**: GCGATCCATATAGTCACT (doi: 10.1097/SLA.0b013e3182a4ea46)	AAACATCCTA **TCATCTGTAGGCTCATTC** ATTTCTCTAACAGC AGTAATATTAATA ATTTTCATGA TTTGAGAAGCCTTC GCTTCGAAGCG AAAAGTCCTAATAGTAGA AGAACCCTCCATAAACCTGG **AGTGACTATATGGATGCC** CCCCACCCTA
ND1	**F**: GCTACGACCAACTCATAC **R**: GAATGCTGGAGATTGTAATG (doi: 10.1097/SLA.0b013e3182a4ea46)	CCCNDCGATTCC **GCTACGACCAACTCATAC** ACCTCCTATGAAAA AACTTCCTACCACTCA CCCTAGCATTACTTAT ATGATATGTCTCCATACC **CATTACAATCTCCAGCATTC** CCCCTCAAAC
ND6	**F**: CCATCGCTGTAGTATATCCAA **R**: TCGGGTGTGTTATTATTCTGA (doi: 10.1097/SLA.0b013e3182a4ea46)	TCCTCAATAG **CCATCGCTGTAGTATATCCAA** AGACAACCATCAT TCCCCCTAAATAA ATTAAAAAAACTA TTAAACCCATATA ACCTCCCCCAAAAT **TCAGAATAATAACACACCCGA** CCACACCGCT

Continuation of Table 2.3		
Mito gene target	**Primer sequence with Citation**	**Oligonucleotide sequence (bolded) for standard curve (5'to 3')**
RNR1	**F**: AGCCTATATACCGCCATCTTC **R**: CATGTTACGACTTGTCTCCTC Made using: (www.idtdna.com/pages / tools /primerquest)	ACCTCTTGCT **CAGCCTATATACCGCCATCTTC** AGCAAACCCTGA TGAAGGCTACAA AGTAAGCGCAAG TACCCACGTAAA GACGTTAGGTCAA GGTGTAGCCCATG AGGTGGCAAGAAAT GGGCTACATTTTCT ACCCCAGAAAACTAC GATAGCCCTTATGAAA CTTAAGGGTCGAAGGTG GATTTAGCAGTAAACTAA GAGTAGAGTGCTTAGTTGA ACAGGGCCCTGAAGCGCGT ACACACCGCCCGTCACCCT CCTCAAGTATACTTCAA AGGACATTTAACTAAAA CCCCTACGCATTTATATA **GAGGAGACAAGTCGTAACATGG** TAAGTGTACT

Continuation of Table 2.3		
Mito gene target	**Primer sequence with Citation**	**Oligonucleotide sequence (bolded) for standard curve (5'to 3')**
RNR2	**F**: GAGCTACCTAA-GAACAGCTAAA **R**: GGTGCCTCTAAT-ACTGGTGATG Made using: www.idtdna.com/pages/ tools/primerquest)	CGAAACCAGA **CGAGC-TACCTAAGAACAGCTAA** AGAGCACACCCGT CTATG-TAGCAAAA TAGTGGGAA-GATT TATAGGTAGAG-GCG ACAAACCTACC-GAG CCTGGTGATAGCTG GTTGTCCAAGATAGA ATCT-TAGTTCAACTT TAAATTTGC-CCACAGA ACCCTCTAAATC-CCCT TGTAAATTTAACT-GTT AGTCCAAAGAGGAACA GCTCTTTGGACACTAG GAAAAAACCTTGTAGA GAGAGTAAAAAATTTA ACACCCATAGTAGGCC TAAAAGCAGCCACCAA TTAA-GAAAGCGTTCAA GCTCAA-CACCCACTAC CTAAAAAATC-CCAAAC ATATAACTGAACTC-CTC

Continuation of Table 2.3		
Mito gene target	**Primer sequence with Citation**	**Oligonucleotide sequence (bolded) for standard curve (5'to 3')**
RNR2		ACACCCAATTGGACCAA TC-TATCACCCTATAGAA GAAC-TAATGTTAGTATA AGTAA-CATGAAAACATT CTCCTCCG-CATAAGCCT GCGTCAGAT-TAAAACAC TGAACTGACAAT-TAACA GCCCAATATCTA-CAATCA ACCAACAAGTCAT-TATTA CCCTCACTGTCAACC-CAAC ACAGGCATGCTCATAA GGAAAGGTTAAAAAAAGT AAAAGGAACTCGGCAAAT CTTACCCCGCCTGTTTAC CAAAAACATCACCTCTAG **CATCACCAGTATTAGAG-GCACC** GCCTGCCCAG
End of Table 2.3		

2.5.4 RT-qPCR and quantitation of mitochondrial DNA copy number

RT-qPCR was performed in a 384 well plate, such that both the standard curve generated from primer detection of the standard gblock and the corresponding primer detection of mt-DNA from samples could be run simultaneously for each gene target, to avoid inter-assay variation. Following the protocol described by Westhaver et al. (2023) [168], standard curves for each mitochondrial gene target were generated by creating a set of ten x 2-fold serial dilutions of the corresponding synthetic oligonucleotides in molecular grade dH_2O ranging from $1x10^7$ to $1.95x10^4$ copies/μL, with duplicates created for each dilution. Each 10μL qPCR reaction for both gblocks and

experimental samples consisted of 5μL SYBR Green, 0.25μL each of forward and reverse primers, 3.5μL molecular grade dH_2O, and 1μL of DNA isolate from either the experimental sample or standard curve preparation. RT-qPCR was performed using the CFX384 Touch Real-Time PCR system (Bio-Rad, Cat. No, 1855484) at 95^{o}C for 2 minutes followed by 39 cycles of (i) 95^{o}C for 10 seconds, (ii) 57.8^{o}C for 30 seconds. Melt curve analysis (95^{o}C for 10 seconds and 65^{o}C for 1 minute) was performed at the conclusion of amplification cycles. Each sample was run in duplicate, with 4 separate experimental replicates for each gene target. The resulting averaged standard curve Cq values were plotted against the natural log of the gblock copy number/μL. To determine the copy number/μL of the experimental mt-DNA, linear regression of the standard curve ($y = mx + b$) was calculated wherein x represented log10 (copy number) of mt-DNA, calculated similarly via the resulting Cq values. Following correction for RT-qPCR reaction volume, the total copies/μL of each experimental sample were then normalized to the average cell count per sample before mitochondrial isolation.

2.6 Measurement of mitochondrial bioenergetics

2.6.1 Seahorse Assay sample preparation

The oxygen consumption rate (OCR) was measured by sequentially adding mitochondrial stressors from the Seahorse XF Cell Mito Stress Test Kit (Seahorse Bioscience, Cat. No. 103015-100) using the Seahorse XFe96 Extracellular Flux Analyzer (Seahorse Bioscience, discontinued), according to the manufacturer's protocol as summarized by Gu et al. (2021) [50]. Briefly, 48 hours-post knockdown, control and RACK1 KD cells in both high and LG were incubated overnight at a pre-optimized density of 1.5×10^4 cells/well for control cells and 2×10^4 cells/well in RACK1 knockdown cells in XFe96 Pro Cell microplates (Seahorse Bioscience, Cat. No. 103793-100) at 37^o C with 5% CO_2. The XFe96 Sensor Cartridge (Seahorse Bioscience, Cat. No. 103793-100) was simultaneously hydrated overnight using XF Calibrating Solution (Seahorse Bioscience, Cat. No. 103793-100) in the XF Utility Plate (Seahorse Bioscience, Cat. No. 103793-100) in a CO_2-free incubator at 37^{o}C. Following incubation, the cells were washed twice with assay medium freshly prepared from the DMEM assay pack (Seahorse Bioscience, Cat. No. 103680-100) as per manufacturer's

instructions (High glucose: 10 mM glucose, 1 mM pyruvate, and 2 mM L-glutamine; low glucose: 10 mM glucose, 1 mM pyruvate, and 2 mM L-glutamine) and incubated in a CO_2-free incubator at 37^{o}C for about 1 hour. The three mitochondrial modulators were prepared through initial dilution in pre-prepared assay medium and were then further diluted in more assay medium to the previously optimized working concentrations for the cells as follows: oligomycin (stock: 100 μM; working: 1.0 μM), carbonylcyanide-4-(trifluoromethoxy) phenylhydrazone (FCCP) Stock: 100 μM; Working:1.0 μM), and a mixture of rotenone and antimycin A (Stock: 50 μM Working: 0.5 μM) (Seahorse Bioscience, Cat. No. 103015-100) as per the manufacturer's instructions. Oxygen consumption rates of the cells during sequential injection of the mitochondrial modulators was measured using the XF Cell Mito Stress Test template program on the XFe96 Analyzer with parameters set as follows: [baseline, 3 cycles; inject port A (oligomycin), 3 cycles; inject port B (FCCP), 3 cycles; inject port C (Rotenone/antimycin A), 3 cycles. Each cycle was composed of [mix 3 minutes, wait 0 minutes, and measure 3 minutes]] to obtain the values for the basal mitochondrial respiration, ATP-linked oxygen consumption rate, maximal respiration, and spare respiratory capacity. After the assays, results were normalized using cell counts. A total of three separate experimental replicates were performed. During statistical analysis, the significant outliers identified via graphpad were removed.

2.7 Cellular evaluation

2.7.1 Analysis of mitochondrial-associated gene expression in RACK1 KD HeLa cells

RNA-seq analysis of three independent RACK1 KD HG cells and their respective controls were processed by the Genomics Core Facility at Dalhousie University. Differentially expressed genes (DEGs) in the RACK1 KD HG cells were identified based on their $\log_2$fold change and significant significant adjusted p-value (padj) when compared to control. This list of DEGs was re-assessed for the presence of MAPs using MitoCarta 3.0 [117]. Mitocarta is a online repository that lists the most complete set of genes with strong mitochondrial localization which includes over 1,100 genes coding for proteins that are recognized to be mitochondrial-associated. A total of

237 MAPs were identified in the RACK1 KD HG DEGs. The list of DEGs found in the RACK1 KD HG cells was analyzed using SHINYGO 0.77 [45] to identify statistical enrichments for specific Gene Ontology (GO) terms from the 'cellular component' annotation. This interaction network was additionally assessed for enriched disease pathways. Categories in cellular components and disease pathways that were identified as having high enrichment were visualized using SHINYGO 0.77 graphical software.

2.7.2 Colony formation assay

The colony-forming assay was performed according to the description in [41]. Briefly, 500, 750 and 1000 were seeded in one well of a 6-well plate in triplicates. Cells were left untreated, at 37^{o}C with 5% CO_2, in either high glucose or low glucose medium to form colonies, which was found to be 14 days for 500 cells/well seedings, 10 days for 750 cells/well seedings, and 7 days for 1000 cells/well seedings. Colonies were washed with PBS, fixed and stained with 0.5% crystal violet in dH_2O for 15 minutes at 37^{o}C. Staining solution was removed and wells were rinsed several times carefully with dH_2O. Plates were dried at RT for 1 hour and colonies imaged using an iPhone 11 (Apple, Model A2111). The colonies/plate and average colony size was characterized using Imaris 10.0.0 surfaces pathways as described above. Colony counts (n, number of colonies per plate) and average surface area (mm^2/colony, total surface area divided by total colonies on that plate) was calculated by Imaris conversion of each colony to a "surface" that had its surface area approximated using previously input measurements for plate size for spatial analysis and scaling performed on ImageJ. Six separate experimental replicates were performed, with outlier wells (i.e. wells with little appreciable growth or far too much growth compared to the visible average) removed before analysis.

2.7.3 Quantification of intracellular ATP levels

RACK1 KD and control cells in both high and low glucose conditions were allowed to grow for 48 hours after knockdown as detailed in methods section 2.1.1 and 2.1.2 before being trypsinized, counted, and re-seeded in a 96-well plate at a concentration of 2.5x10^4cells/well. All four conditions were seeded into the same 96-well plate in

2 sets of triplicates to reduce inter-assay variation. Cells were allowed to re-attach overnight or until cellular density reached 70%. Cellular ATP levels were quantified using a luciferin- and luciferase-based assay (Thermofisher, Cat. No. A22066) following the manufacturer's protocol. Briefly, a standard curve was generated using solutions of known ATP concentrations prepared from twelve x two-fold serial dilutions of ATP in dH_2O ranging from 100 μM to 0.05 μM. One set of triplicate cells for each condition were rinsed with PBS and lysed with 10 μL of somatic cell ATP releasing reagent (Sigma-Aldrich, Cat. No. FLSAR-1VL). The resulting lysate and ATP standard curve were diluted to a final 1:10 concentration with standard reaction solution and the sample luminescence recorded with a Perkin Elmer Victor X5 2030 Multilabel HTS Fluorescence Microplate Reader (PerkinElmer, Cat. No. 2030-0050). The second set of triplicates for each condition were trypsinzed and cell counts performed using a CellDrop BF cell counter (Brightfield-only model) (Denovix, Cat. No. BF-UNLTD) ATP levels were calculated as μM ATP and normalized to cell counts from each set of triplicates. A total of three separate experimental replicates were performed.

2.8 Statistical analysis

The two-tailed unpaired Student's t-test and the Mann–Whitney test were performed using GraphPad Prism 9.5.1 (GraphPad Software) on all assays. All functional assays were representative of $\geq$3 independent experiments (unless otherwise indicated), and expressed as mean$\pm$SEM. A p-value less than 0.05 (*), 0.01 (**) or 0.001 (***) indicated statistical significance.

Chapter 3

Results

3.1 Characterization of RACK1 KD on HeLa cell physiology

RACK1 activity and mitochondrial function overlaps in many biological categories, including both cellular pathway and disease interactions [94],[139],[78],[43],[55],[73],[111],[116]. Despite this, research into their associations has mainly focused upon investigating RACK1 interactions with mitochondrial-associated proteins [171],[88],[72],[150]. However, a robust characterization of how the two interact *in vitro* is missing. The goal of this study was to characterize how the mitochondria in cancer cells respond to a decrease in RACK1 expression. The aims of the project were threefold:

1. Assess the impact of RACK1 KD on HeLa cell morphology and growth parameters.

2. Characterize mitochondrial morphology and network dynamics in RACK1 KD cells.

3. Characterize mitochondrial biogenesis and functionality in RACK1 KD cells.

First, a broad characterization of how a decrease in RACK1 expression impacts cellular physiological parameters will be described. This will include investigation of how knockdown impacts mitochondrial-associated gene expression, cellular proliferation, and viability assessment. The following two objectives include a broad assessment of the mitochondrial physiology in RACK1 KD cells. This includes a i) comprehensive assessment of mitochondrial morphology and network activity using confocal and TEM analysis; and ii) characterization of mitochondrial biogenesis, respiration, dynamics, and genomics via measurements of nuclear expression of biogenesis and dynamics mediators, mitochondrial DNA (mt-DNA) levels, and oxygen consumption.

3.1.1 RACK1 KD is successful in both HG and LG conditions

To ensure that the RACK1 KD was successful in depleting RACK1 levels in HeLa cells, immunoblotting for RACK1 protein levels was performed for 8 days in RACK1 KD HG cells. RACK1 levels in RACK1 KD HG cells remained minimal for 6 days post-knockdown (Figure 5.6A). The addition of a second glucose condition (LG) was added to the study to mitigate the Warburg effect, a hallmark of cancer cells [164],[79]. It refers to the preference of cancer cells to use anerobic measures (glycolysis) to process glucose for energy rather than oxidative phosphorylation. This has been found to mask some of the impact of mitochondrial dysregulation on the cells [133],[79]. In the context of this mitochondrial investigation, the LG condition was included to ensure that the RACK1 knockdown cells were forced to rely more heavily on their mitochondrial networks. The efficacy of the KD was assessed in both RACK1 KD HG and LG cells in a western blot. RACK1 levels in RACK1 KD HG and LG cells were decreased 72 hours post-knockdown (Figure 5.6B).

3.1.2 RACK1 KD causes the dysregulation of MAPs expression supporting mitochondrial translation and respiration

Given the broad range of cellular functions that RACK1 facilitates, we decided to analyze how RACK1 KD impacted the expression of various MAPs within the cell. Previous research within the Cheng lab had utilized RNA-seq analysis to profile the transcriptomic changes that occur in RACK1 KD cells. We used this dataset to specifically focus on how RACK1 KD impacted the expression of various MAPs within the cell. These data were analyzed further in this study to fully determine the extent to which various mitochondrial processes and pathways were impacted by the knockdown. After input into the Mitocarta database, it was found that the expression of 237 genes associated with mitochondrial function was impacted by a decrease in RACK1. Further analysis of the mitochondrial-associated genes using ShinyGO to determine which pathways were significantly impacted determined that three major regions of mitochondrial function were impacted: i) the mitochondrial respiratory

chain complex, with mitochondrial respiratory chain complexes I, III, and IV experiencing significant impact; ii) mitochondrial protein synthesis, including mitochondrial translation, mitochondrial translation elongation, and mitochondrial translational termination being impacted; and iii) the mitochondrial transport mediators , including those involved in outer and inner membrane translocation (Figure 5.5A). Given that aberrant RACK1 expression is frequently reported in tissues analyzed in studies on cancer, heart, and neurological diseases, we additionally investigated the associations between the enriched mitochondrial genes and the KEGG database for reported disease-associated molecular pathways. It was found that significant associations between the mitochondrial genes affected by the RACK1 knockdown and neurodegenerative disease pathways, diabetic cardiomyopathy, and liver dysfunction pathways existed (Figure 5.5B).

3.1.3 RACK1 knockdown alters HeLa cell growth parameters and induces significant morphological changes in HeLa cells

RACK1 knockdown in HeLa cells had resulted in the concomitant dysregulation in 237 MAPs that broadly impacted regions of mitochondrial function including translation, membrane integrity and transport, and electron transport chain activity. We suspected that the dysregulation of these mitochondrial roles would have deleterious effects upon the cell and decided to complete a very broad characterization of HeLa cells experiencing RACK1 knockdown was completed to determine how cellular morphology, viability and proliferation was impacted before more closely assessing mitochondrial functionality in the RACK1 KD cells.

We used TEM to analyze the ultrastructural morphology of RACK1 KD HG and LG cells compared to the control. Control HG and LG cells demonstrated intact membranes with punctuate protrusions and organelles scattered throughout the cytoplasm (HG, Figure 5.7A, see inset; LG, Figure 5.8A, see inset). In contrast, the RACK1 KD HG and LG cells showed significant visual morphological changes compared to controls (HG, Figure 5.7C-D, see inset; LG, Figure 5.8C-D, see inset). The membranes of RACK1 KD HG and LG cells had large irregular bulges, with some cytoplasmic bodies separated from the cell membrane (HG, Figure 5.7C, see inset; LG, Figure 5.8C, see inset).

3.1.4 RACK1 KD decreases cellular viability, suppresses cellular proliferation, and decreases ATP production in RACK1 LG cells

Visual analysis of the RACK1 KD cells under TEM indicated that cells were undergoing significant morphological changes compared to control (Figure 5.7, Figure 5.8). We decided to measure functional parameters in the RACK1 KD HeLa cells, including viability, proliferative properties, and ATP production. To determine if cell viability was impacted by RACK1 KD, a colony-formation assay was performed to assess cell survival rates. The ability of RACK1 KD cells to survive and reproduce to form colonies was compared to that of the control. To achieve this, RACK1 KD HG and LG cells and controls were seeded at densities of 750 and 500 cells/well. The number of colonies formed after up to 2 weeks of growth for all three seeding densities was assessed in both the HG and LG conditions. RACK1 KD HG and LG cells demonstrated reduced colony numbers across the 750 and 500-cell seeding densities for both glucose conditions (Figure 5.9A-B). This decrease was not significant for the RACK1 KD HG. However, the RACK1 KD LG cells saw a significant decrease in colony forming ability, with two fold decreases in mean colonies numbers reported (Figure 5.9 A-B).

To determine the ability of the surviving cells in a population to divide and create progeny over time after the knockdown, the diameter of the colonies formed by RACK1 KD HG and LG cells was compared to the control (Figure 5.9C-D). Despite not showing significant decreases in cellular viability, the RACK1 KD HG samples seeded at 750 cells/well demonstrated a significant decrease in colony size (2.5 mm) compared to the control (1.96 mm). RACK1 KD LG mean colony diameter at the 500-seeding density was significantly smaller (2 mm) on average compared to that the control (2.85 mm). The 750-seeding density demonstrated a similar trend, where the RACK1 KD LG mean colony diameter (1.4 mm) was significantly smaller than the control mean colony diameter (2.25 mm) (Figure 5.10C-D). Based on the decreases in RACK1 KD HG and LG cellular viability and proliferation compared to the controls, we assessed the energetic capacity of the RACK1 KD cells compared to the control by measuring ATP production through a luciferin- and luciferase-based assay. RACK1 KD HG cells had significantly lower ATP levels (0.33 μM/cell) in comparison to the control (0.53 μM/cell) (Figure 5.9G). RACK1 KD LG cells also had lower ATP levels

(0.63 μM/cell) compared to control (0.83μM/cell) (Figure 5.9G).

3.2 RACK1 KD alters mitochondrial structure and network dynamics in HeLa cells

RACK1 KD produced several cellular responses that were suggestive of mitochondrial dysfunction, including dysregulated expression of MAPs (Figure 5.5), decreased cellular viability and proliferative potential (Figure 5.9A-D) and lowered cellular ATP production (Figure 5.9G). To better discern the direct impacts of RACK1 KD on mitochondria, we initiated the morphological component of our study with microscopic analysis of mitochondria in RACK1 KD HG and LG cells.

3.2.1 RACK1 KD cells exhibit higher incidence of defects in ultrastructural mitochondrial appearance

We began the morphological assessment of RACK1 KD mitochondria through TEM analysis of the mitochondrial outer/inner membranes and cristae organization in RACK1 KD HG and LG cells/controls (Figure 5.10). The control HG and LG mitochondria displayed consistently smooth outer/inner membranes (Figure 5.10B, D, yellow arrows), the regular appearance of long, organized reticular cristae that spanned the inner membrane (Figure 5.10A, C, yellow arrows), and relatively uniform matrix density (Figure 5.10A-D). In contrast, multiple visual defects present in the mitochondrial physiology of RACK1 KD HG and LG cells appeared, including: i) the presence of mitochondrial "inclusion bodies" (unusual dark matter within the less dense matrix) (Figure 5.10F, yellow arrow); ii) mitochondrial swelling (mitochondrial bloating) (Figure 5.10E, yellow arrows); iii) mitochondrial matrix condensation (dark matrix consistently present throughout inner membrane) (Figure 5.10G, yellow arrows); iv) decrease in cristae (Figure 5.10E, yellow arrows); and v) a shrunken, fragmented appearance (Figure 5.10G, yellow arrows).

We quantified the incidence of three commonly found mitochondrial morphological defects (Figure 5.11A-I), including mitochondrial membrane rupture (Figure 5.11A-B, yellow arrows), loss of cristae (Figure 5.11D-E, outlined in yellow), and presence of mitochondrial inclusions (Figure 5.11G-H, yellow arrows). Cristae absence (Figure

5.11C) and mitochondrial inclusion bodies (Figure 5.11I) were four times more common in RACK1 KD HG cells compared to control. RACK1 KD LG cells had eighteen times more inclusion body incidences compared to the control (Figure 5.11I) but did not exhibit significant change in incidence of cristae absence (Figure 5.11F). Interestingly, neither RACK1 KD HG nor LG demonstrated any change in mitochondrial membrane rupture compared to their respective controls. (Figure 5.11C).

The RACK1 KD HG and LG cells revealed glucose-specific differences in mitochondrial presentation. Large mitochondrial groups would coalesce in a localized region within the cell in the RACK1 KD HG sample (Figure 5.12A-B) (Figure 5.12C-D). A unique phenotype in RACK1 KD LG mitochondria was also identified (Figure 5.13A-D). Afflicted mitochondria exhibited inner membranes packed with unusual black circularized structures termed "inclusion bodies" (Figure 5.13C-D, yellow arrows).

3.2.2 RACK1 KD caused loss of connectivity and fragmentation of mitochondrial networks

Ultrastructural analysis of RACK1 KD mitochondrial membranes revealed distinctive shifts in mitochondrial structure compared to control (Figures 5.10, 5.11, 5.12, 5.13). We decided to further assess how RACK1 KD impacted mitochondrial structure through confocal analysis of mitochondrial networks. Live confocal imaging of stained RACK1 KD cells and controls was used to characterize the connectivity of mitochondrial networks. The three-dimensional capture of these networks was also used to provide quantitative information on mitochondrial mass and network activity.

Confocal analysis of RACK1 KD cells and controls revealed striking differences in mitochondrial network connectivity (Figures 5.14, 5.15). Control HG and LG cells had a singular central, large network that comprised the majority of the visual mitochondrial mass within a given cell (Figure 5.14A-B; 5.15A-B). Smaller sub-networks and individual fragmented mitochondria were dispersed throughout the cell (Figure 5.14A-B; 5.15A-B). In contrast, RACK1 KD HG and LG cells demonstrated a dramatic loss of network connectivity and a corresponding increase in network fragmentation throughout the cell (Figure 5.14C-D; 5.15C-D). We decided to characterize

the changes in the mitochondrial network of RACK1 KD HG and LG cells by quantifying the mitochondrial number, network surface area, network volume, and mean mitochondrial volume values from the three-dimensional cellular images. Imaris software was used to create surface renderings of mitochondrial networks and extract quantitative information from renderings that could be used to describe mitochondrial character (Figure 5.17A-D). First, the total mitochondrial numbers (identified as "disconnected components" by Imaris software) were measured per cell (Figure 5.17A). There was a significant increase in RACK1 KD HG mitochondrial numbers/cell, averaging 499 "disconnected components" per cell compared to the 150 "disconnected components" in control HG cells (Figure 5.17E). The RACK1 KD LG cells did not significantly increase, with an average of 278 "disconnected components" per cell compared to the 265 "disconnected components" found in the control LG cells (Figure 5.17E). We then measured total mitochondrial surface area/cell (sum of the surface area of networks in a cell/the number of cell nuclei) was measured. RACK1 KD HG networks averaged 4730 μm^2 surface area/cell, 1.8 times that of the control HG network's mean surface area/cell, which averaged 2600 μm^2 /cell (Figure 5.17 F). The RACK1 KD LG cells mean network surface area did not significantly change from that of the control, averaging 1860 μm^2 /cell compared to the 2340 μm^2 mean surface area for the control LG networks (Figure 5.17F). RACK1 KD HG cells demonstrated a significant increase in total mitochondrial network volume (1269μm^3) compared to control (770μm^3) (Figure 5.17 G), and RACK1 KD LG cells experiencing a net decrease (360μm^3) compared to the control LG (465μm^3) (Figure 5.17G). Finally, the RACK1 KD HG network mean mitochondrion volume was decreased (2.5μm^3/mitochondrion) compared to the control network mean mitochondrion volume (5.1 μm^3/mitochondrion) (Figure 5.17H). The RACK1 KD LG mean mitochondrion volume did not significantly decrease (1.29 μm^3/mitochondrion), compared to the control HG cells 1.75 μm^3 (Figure 5.17H).

The final mitochondrial network quality that we assessed in this study was mitochondrial network character (Figure 5.16). We used Imaris surface renderings to measure sphericity of each disconnected component within a mitochondrial network and assign a corresponding value between 0 and 1. Higher sphericity values indicated a disconnected piece of mitochondrial network (a single mitochondrion), whereas lower

values indicated a less spherical nature, which suggested a filamentous network. The RACK1 KD cells and control networks were categorized in this manner with the following values used to delineate character "groups": fragmented, sphericity ≥ 0.451; intermediate, sphericity between 0.450 and 0.311; and filamentous, sphericity ≤ 0.310 (Figure 5.16A-D). The proportion (%) of each spherical group within the total mitochondrial network was defined as the volume of the disconnected components in that spherical group/cell divided by the total mitochondrial volume of that cell (Figure 5.16E). The majority of the control cell network volume in both HG and LG cells (Figure 5.16E), was filamentous (82% and 59%, respectively) (Figure 5.16 E). Ten percent and twenty-one percent of the mitochondrial network volume was ascribed a fragmented characteristic (Figure 5.16E). In contrast, 77% and 66% of the mitochondrial network volume of RACK1 KD HG and LG cells was assigned to the fragmented category, respectively (Figure 5.16E).

3.3 Mitochondrial functionality assessment in RACK1 KD cells

The final aim of this project was to characterize the functionality of mitochondria in RACK1 KD HG and LG cells. We used both RT-qPCR and respirometry measurements to determined how mitochondrial biogenesis, respiration, fusion/fission, and genomics were impacted by RACK1 KD.

3.3.1 RACK1 knockdown dysregulates nuclear expression of mitochondrial biogenesis and fusion/fission mediators

Confocal imaging of the RACK1 KD HG and LG networks revealed increases in mitochondrial network fragmentation of the network. Considering these factors, we decided to measure nuclear expression of biogenesis mediators and fusion/fission mediators.

We assessed whether mitochondrial biogenesis was upregulated in the RACK1 KD cells by measuring the nuclear expression of biogenesis mediators *PGC1α* and *TFAM* using RT-qPCR (Figure 5.18). *PGC1α* and *TFAM* expression doubled in RACK1 KD LG cells but was unchanged in RACK1 KD HG cells (Figure 5.18A-B).

Next, we measured the nuclear expression of fusion mediators (*OPA1*, *MFN1*,

and *MFN2*) and fission mediator (*DRP1*) in RACK1 KD cells using RT-qPCR (Figure 5.19). RACK1 KD HG cellular expression of fusion mediators *OPA1* ,*MFN2*, and *DRP1* expression decreased (Figure 5.19). In contrast, the RACK1 KD LG cells demonstrated upregulated nuclear expression of *MFN2* compared to the control (Figure 5.19).

3.3.2 RACK1 knockdown impacts mt-DNA copy number differentially depending on glucose conditions

Mitochondrial biogenesis and network formation are cellular processes that are heavily intertwined with mt-DNA production, so we decided to further characterize the mitochondrial response to RACK1 KD by measuring mt-DNA levels.

The expression of mt-DNA-encoded genes for *COX I, CytB, ND1, ND6, RNR1* and *RNR2* were measured via RT-qPCR (Figure 5.20). RACK1 KD HG cells demonstrated significant increases in the levels of all mt-DNA encoded genes. *CytB* and *RNR1* levels increased by 2-fold and 1.5-fold, (Figure 5.20D-E). *ND1, ND6, COX I,* and *RNR2* levels in RACK1 KD HG cells all increased by under a fold-change compared to the control (Figure 5.20A-C, E-F). It was found that RACK1 KD LG cells had decreased mt-DNA . *RNR1* and *ND6* levels decreased by 4-fold, *CytB* and *RNR2* decreased by 3-fold and *ND1* levels decreased 2.5-fold (Figure 5.20A-B, D-F). There was no significant change in *COX I* levels in RACK1 KD LG cells (Figure 5.20C).

3.3.3 RACK1 knockdown decreased mitochondrial respiration in HeLa cells

Our final assessment of mitochondrial function compared RACK1 KD HG and LG mitochondrial bioenergetics to their respective controls. We used the XFe96 seahorse analyzer to measure mitochondrial respiration in the RACK1 KD cells. The mitochondrial stress test identifies critical respiratory defects by measuring how cellular oxygen consumption rates change in response to the introduction of mitochondrial toxins. It first determines basal oxygen consumption, which reports the energetic demand of the cell under baseline conditions. An injection of oligomycin then decreases the OCR of the cells, which determines the proportion of mitochondrial activity generating

ATP. To estimate the maximal respiration value, injection of the mitochondrial inner membrane uncoupler, carbonyl cyanide p-trifluoromethoxyphenylhydrazone (FCCP), determines the maximum oxygen consumption possible for the cell. Finally, cellular fitness is assessed using the spare respiratory capacity, which is calculated by comparing the maximal respiration values to the original baseline. We used these values to determine the RACK1 KD cellular bioenergetic profiles compared to the control. Oxygen consumption values of RACK1 KD HG and LG cells across the experiment were decreased compared to their controls (Figure 5.21A). The cellular bioenergetic profiles for both RACK1 KD HG and LG demonstrated significant decreases in basal respiration values (Figure 5.21B), spare respiratory capacity (Figure 5.21C), maximal respiration values (Figure 5.21D), and mitochondrial ATP production (Figure 5.21A) compared to their respective controls.

Chapter 4

Discussion

Receptor of activated protein C kinase 1 (RACK1) is a 36-kDa multifunctional scaffolding protein that coordinates a variety of fundamental cellular processes in eukaryotic cells, including signal transduction, protein synthesis, and cellular migration [77],[103],[43]. Unusual RACK1 expression has been identified as a prognostic indicator in the development of a wide range of pathological scenarios [5],[83],[17],[18],[2]. RACK1 literature is complex, and it has remained historically difficult to characterize the role of RACK1 in disease pathology [17],[18],[2]. This is due to its extensive range of protein-protein interactions, its ability to modify its partner choice based on environmental context, and its high expression throughout mammalian tissues [1]. Mitochondria manage many important cellular roles including cellular energy production, stress responses, and death [25]. RACK1 pathway interactions overlap with mitochondrial-associated proteins, but a broad characterization of mitochondrial function in the context of RACK1 signaling has not been completed. Proper characterization of this interaction would advance our understanding of RACK1 biology and contextualize how RACK1 signaling influences the initiation and progression of disease. Consequently, the goal of this project was to characterize how a decrease in RACK1 expression impacts mitochondrial physiology in HeLa cells. A complete summary of the response of both RACK1 KD HG and LG cells can be found in Figure 5.22.

4.1 RACK1 KD impacts HeLa cell morphology, viability, and energy production

Our first goal was to broadly assess how RACK1 KD impacts the HeLa cell using TEM ultrastructural analysis. The control cells exhibited cell membranes with small, short microvilli protrusions (Figure 5.7A, (see inset)); (Figure 5.8A (see inset)). In contrast, the RACK1 KD HG and LG cells displayed overly smoothed, curved cell

membranes that formed "blebs" of cytoplasm ((Figure 5.7C, (see inset)); (Figure 5.8C (see inset)). RACK1 dysfunction has been correlated with a loss of cytoskeletal maintenance in a diverse range of cell types, and RACK1 KD can devastate cell membrane integrity [171],[72]. Freitas - Filho et al. (2021) [40] demonstrated that RACK1 KD in mast cells caused cells to assume an unusual rounded membrane with "ruffled" edges, similar to the RACK1 KD ultrastructural morphology reported here.

We additionally explored how HeLa cell viability and proliferation were impacted by RACK1 KD (Figure 5.9A-D). At seeding densities of 500 cells/well and 750 cells/well, the RACK1 KD HG cells did not experience a significant decrease in viability (Figure 5.9A-B). However, the RACK1 KD LG cells experienced a significant decline in viability at both seeding densities; a twofold decrease in colony numbers was recorded at both 500 cells/well and 750 cells/well (Figure 5.9A-B). RACK1 KD cells in other studies show a similar trend wherein they survive initial knockdown and retain normal function unless further challenged with additional stressors [40],[43],[148]. These stresses are typically nutrient-related deficits: for example, Asc1/RACK1 KD cells demonstrate growth defects when moved to glucose-free medium that requires increased mitochondrial function to process alternative carbon sources [148]. This decreased ability to tolerate stress may explain why the RACK1 KD HG cell viability did not decrease whereas the RACK1 KD LG cell viability measurements did.

RACK1 KD HG and LG cells had decreased proliferation measurements compared to the control at a seeding density of 750 cells/well (Figure 5.9C-D). Decreases in cellular proliferation following RACK1 KD are consistent with findings in other studies [113],[38],[84]. However, this project only based proliferation measurements upon final colony diameter. While this methodology is useful for gauging how cellular proliferation is impacted by experimental treatments, these findings should be further confirmed with a more conventional method. For example, an MTT assay could be used to quantify the cellular proliferation results seen in this study [84].

The unchanged viability measurements in the RACK1 KD HG cells contrasted the TEM membrane micrograph results in this project. The micrographs taken of the RACK1 KD HG and LG cells showed significant membrane changes in the KD cells compared to the respective controls. Considering that the RACK1 KD HG cells had no significant shift in viability, this contrast in findings was surprising. The difference

between the results of the TEM analysis and the cell viability analysis may be the result of the different processing methodologies between experiments. The fixation process used for TEM imaging may place additional stress upon the RACK1 KD cells and produce the membrane disintegration seen in the final images [53]. Given that RACK1 KD cells react poorly to stressors, this may explain the difference between the RACK1 KD HG cells in these two experiments [148],[38].

Investigation of ATP levels in RACK1 KD HG and LG cells revealed a 50% decrease in RACK1 KD HG cellular ATP levels and an insignificant decline in RACK1 KD LG cellular ATP levels (Figure 5.9G). The RACK1 KD HG result is consistent with results from Cardenas et al. (2015) [19], who showed that RACK1 ortholog LACK knockdown decreased ATP levels in unicellular *Leishmania* parasites. However, RACK1 KD LG cellular ATP levels did not significantly decrease, which was unexpected considering the significant decrease in RACK1 KD LG cellular viability and proliferation. This phenomenon may be attributed to the Warbug effect in the RACK1 KD HG cells, where glycolytic intermediates are funneled into pathways that produce nucleosides and amino acids, instead of ATP. The net decrease in the already limited cellular ATP produced in glycolytic cells like the RACK1 KD HG cells may appear more striking than the RACK1 KD LG, which are forced to use aerobic pathways for energy production [157].

Overall, the results found in this study are largely consistent with previous literature findings and indicate that RACK1 KD impacts cellular morphology, viability, proliferation, and energy production in HeLa cells.

4.1.1 RACK1 KD significantly altered mitochondrial ultrastructural membranes in a manner exacerbated by decreased glucose in HeLa cells

To investigate how RACK1 KD impacted mitochondria morphology, TEM was used to visualize RACK1 KD cell mitochondrial membranes, cristae, and matrix morphology (Figure 5.10). The RACK1 KD HG and LG cells had a higher incidence of mitochondrial membrane structural anomalies such as inclusion bodies (Figure 5.10F, yellow arrows), ii) mitochondrial swelling, (Figure 5.10E, yellow arrows), mitochondrial matrix condensation (Figure 5.10G, yellow arrows), lamellar cristae loss, (Figure

5.11D-E, yellow arrows), and a shrunken, fragmented appearance (Figure 5.10G, yellow arrows).

The significant increase in lamellar cristae loss in the RACK1 KD HG cells was measured by selecting mitochondria with both inner and outer membranes fully in plane that displayed little to no inner cristae formation (Figure 5.11C-D). Cristae comprise a dynamic framework that houses the ETC protein complexes. 'Lamellar' cristae are long, organized, reticular structures that span the inner membrane [136]. The maintenance of cristae is a complicated, poorly understood process requiring the careful balance of the mitochondrial fusion/fission mediators and specialized cristae modelling machinery [137]. While cristae loss can be triggered by a multitude of factors, the best recognized currently include loss of fusion/fission balance and ETC chain dysfunction [137],[125], which are other regions of mitochondrial function impacted by RACK1 KD in this study.

RACK1 KD HG and LG mitochondria displayed an increased incidence of mitochondrial inclusion bodies within the matrix. In particular, RACK1 KD LG mitochondria had an increased incidence of a unique inclusion body phenotype. Mitochondria assigned to this category were shrunken, with lamellar cristae loss and increases in vesicular cristae that surrounded dense, black inclusion bodies (Figure 5.13C-D). We performed a preliminary review for images of stressed mitochondria to determine what caused this structure. The most convincing visual matches to the RACK1 KD LG phenotype was reported by Singh et al. (2021) [137], who suggested that the structure results from thickened cristae that surround a condensed, darkened matrix. This phenomenon is attributed to compaction of the inner mitochondrial membrane to support the metabolic demands of the leukemic cell [137]. The results seen in this study were supported by Liu et al. (2012) [82], who reported a similar mitochondrial phenotype in cells experiencing a decrease in prohibitin 2 (PHB2) levels. PHB2 is a chaperone suspected to support ETC complex protein folding. PHB2 and RACK1 engage in reciprocal stabilization in the cell and RACK1 KD abolishes PHB2-mediated activation. Liu et al. (2012) [82] reported loss of PHB2 in these cells impaired complex I activity in these cells, resulting in mitochondrial fragmentation, loss of cristae, and an increase in matrix condensation. This provides an interesting connection between decreased RACK1 activity and mitochondrial cristae modelling

that produces a phenotype similar to that in our RACK1 KD LG cells. Finally, Rottner et al. (2023) [125] reported a similar phenotype while studying how loss of type II diabetes-implicated autophagy receptor CALCOCO2 impacts beta cell activity. TEM analysis of mitochondrial structure revealed dramatically distorted cristae and outer membrane shape in CALCOCO2 KD cells. The results of these studies above suggest that the "inclusion body" phenotype seen in this study may be a pro-survival restructuring of cristae to maximize ETC functionality, but more work will be required to confirm the causal relationship between RACK1 KD and the cristae morphology shifts.

All of the membrane perturbations described above can be connected to dysfunctional cristae modelling. Cristae dysfunction is a potential consequence of dysregulated fusion/fission activity and ETC dysfunction, both of which were identified in the RACK1 KD HG and LG mitochondria [144],[101]. This provides an interesting connection between the form and the function of the mitochondria in this project. Quintana et al. (2021) [114] suggested that the cause of the ETC dysfunction and fusion/fission imbalance in cells experiencing thickened, unusual cristae was due to increased concentrations of ROS in the cell. Improperly cleared ROS oxidizes mtDNA in the cell and affects respiratory chain complex production, which results in further overproduction of ROS. This cycle gradually erodes the integrity of the mitochondrial structure and decreases oxygen consumption [114],[101],[110]. Fusion is paused in these mitochondria, fragmenting them from the network to protect the structure from deleterious mutations and high ROS production [110]. Understanding how cristae are impacted by RACK1 KD by examining potential triggers such as ROS production could provide interesting context to RACK1's impact on mitochondrial physiology.

4.1.2 Increased mitochondrial numbers, surface area, and volume corresponds with a twofold increase in expression of biogenesis mediators in RACK1 KD HG cells

RACK1 KD HG cells displayed an increased incidence of large numbers of mitochondria clustered in groups throughout the cell (Figure 5.12A-B, beige outline). Confocal analysis of mitochondrial networks in RACK1 KD HG cells revealed increased

mitochondrial numbers (Figure 5.17E), mitochondrial network surface area (Figure 5.17F), and mitochondrial network volume (Figure 5.17G). Imaging results similar to the results seen here have been recorded in other RACK1 KD studies: Qiu et al. (2017) [113] found that RACK1 deficiency caused increased mitochondrial numbers and increased mitochondrial network mass in splenic T cells. Further confocal analysis revealed mitotracker-positive "tubular clusters" of mitochondria, which is also similar to the results reported here (Figure 5.12A-B, beige outline). Additional RT-qPCR analysis of biogenesis mediator expression in RACK1 KD HG cells revealed a two-fold increase in *PGC1α* and *TFAM* expression, suggesting a concerted cellular effort to increase mitochondrial numbers in the cell. In a separate study, Zhu et al. (2016) [185] reported that mitochondrial numbers and their total network area within the cell significantly increased as myocardial muscle cells experienced hypoxia. Cells responded by increasing *PGC1α* and *TFAM* expression levels to drive increased mitochondrial network volume during recovery [185]. However, an alternative explanation for the mitochondrial accumulation within the RACK1 KD HG cells is that the increased mitochondrial volume is the result of an impaired mitophagy response. RACK1 promotes the autophagy-initiation complex formation in several mammalian cell types [184], and RACK1 absence leads to impaired autophagy and the accumulation of mitochondria in peripheral T cells [113]. The accumulation seen in the RACK1 KD HG cells of damaged mitochondria could be similarly related to the loss of mitophagy in the cell. The impact of RACK1 KD upon the mitophagy process could be measured through use of indirect immunofluorescence to measure LC3, the autophagosome marker in mammalian cells [75], [113]. Measurement of LC3-positive dots representing autophagic LC3 puncta after treatment with a lysosomal protease inhibitor in RACK1 KD cells may provide a clue as to how RACK1 KD impacts autophagy in both high and low glucose environments. Alternatively, immunoblotting of the mitophagy pathway mediators PINK1 and PARKIN could provide valuable context to the upstream effects of RACK1 KD upon mitophagy [113]. Determining whether mitophagy or biogenesis are the primary drivers of the increased mitochondrial load seen in the RACK1 KD HG cells will add important context to the impact of RACK1 KD on mitochondrial function.

While RACK1 KD LG cells had significantly increased expression of biogenesis

mediators *TFAM* and *PGC1α* (Figure 5.18A-B), they demonstrated a decrease in overall surface area, volume, and no change in overall mitochondrial number compared to the control (Figure 5.17B-D). The increase in biogenesis mediator expression may indicate an attempt to increase mitochondrial numbers [166], but RACK1 KD LG cells are unable to complete this successfully (Figure 5.17B-D). This project constitutes one of the few descriptions of the mitochondrial network phenotype in RACK1 KD LG cells. More analysis will be required in RACK1 KD LG cells to determine how RACK1 signalling impacts network dynamics in response to nutrient deprivation.

4.1.3 Mitochondrial networks became fragmented following RACK1 KD and glucose condition altered cellular expression of fusion/fission mediators

Sphericity assessment of mitochondria in RACK1 KD HG and LG displayed a predominantly fragmented network phenotype (Figure 5.16) and a decrease in mean mitochondrion volume (Figure 5.17H). Literature indicates that RACK1 KD dysregulates mitochondrial network dynamics in a variety of ways. Zhao et al. (2015) [184] describes small, shrunken, unconnected mitochondria in RACK1-deficient macrophages, but conversely, Qiu et al. (2017) [113] found that elongated mitochondria networks form in RACK1-deficient CD8+ T cells. This contrast in findings suggests that RACK1 impact on mitochondrial network remains unclear. The balance of fusion and fission in a mitochondrial network serve as a quality control mechanism for cellular integrity [167],[158],[96]. The dysregulation of this network through loss of mitochondrial fusion could indicate a protective reponse by the cell against further mitochondrial damage [167],[116]. The mitochondrial fusion mechanism mediates content mixing, which compensates for dysfunctional gene products of individual mitochondria by i) decreasing the concentration of ROS in stressed mitochondria and ii) allowing mt-DNA to mix, compensating for missing or dysfunctional gene products [152]. Impairment of mitochondrial function strongly inhibits mitochondrial fusion in mammalian cells [118],[167]. Dysfunctional mitochondria lose their fusion capacity by inactivating fusion machinery, preventing the damaged mitochondria from incorporating back into the healthy mitochondrial network, sending the network into a state of fragmentation [101]. The loss of network fusion may act as a mechanism

to distinguish non-functional from functional mitochondria on a morphological basis [101],[167], which may be occuring in response to the stress incurred via RACK1 KD.

Dysregulation of the mitochondrial network in the RACK1 KD cells continued at the phenotypic level. RACK1 KD HG cells had decreased *OPA1, MFN1* and *DRP1* expression (Figure 5.19A-C). Decreases in fusion and fission protein expression has consequences for the mitochondrion; *OPA1* knockdown causes hyper-fragmented mitochondrial networks, cristae depletion, and ETC dysfunction due to a complex I-mediated NAD+ regeneration [70]. The RACK1-PHB2 interaction explored earlier in the context of cristae malformation may additionally impact OPA1 activity. PHB2 forms a complex with stomatin-like protein 2 (STOML2) that regulates integral mitochondrial integral protease (OMA1) [29]. Active OMA1 cleaves the long fusion-active isoform of OPA1 (L-OPA1), to short fusion inactive OPA1 (S-OPA1) [29]. Dysregulation of PHB2 activity via RACK1 KD could potentially cause uncontrolled OMA1 activity, blocking OPA1-mediated inner membrane fusion in the cell, hereby fragmenting the network [39],[29]. The decrease in *DRP1* expression in RACK1 KD HG cells (Figure 5.19B) has been shown in other investigations to induce lamellar cristae dysfunction, loss of ETC components and reduced mitochondrial respiration. Li et al. (2015) [78] found that increase in *GNB2L1* expression corresponded to a decrease in Drp1 levels in kidney (HK-2) cells, but protein-protein interactions between RACK1 and Drp1 are not confirmed. Outside of physical interactions, RACK1 could potentially influence Drp1 dynamics via its role in actin regulation. Drp1 recruitment to fission sites on the outer mitochondrial membrane is largely mediated via actin polymerization [52]. This stimulates oligomeric maturation of Drp1 on mitochondria in mammalian cells and allows fission to commence [52]. The loss of RACK1 could potentially dysregulate actin dynamics, impacting Drp1 activity in the cell. Finally, RACK1 KD HG cells experienced a decrease in *MFN1* expression (Figure 5.19C, which is associated with network fragmentation, complex I deficiency, and reduced mitochondrial membrane potential [33]. No direct association between RACK1 and MFN1 has been identified; RACK1 may associate with MFN1 via βIIPKC activity [27]. βIIPKC is a regulator of mitochondrial dynamics through MFN1 phosphorylation, which appears to cause loss of MFN1 activity in the cell in cardiomyocytes [27].

In RACK1 KD LG cells we found increased *MFN2* expression (Figure 5.19D). The increase in fusion mediators usually occurs under stress as the cell works to recover, and the overexpression of fusion mediators is associated with a "rescue" response that restores optimal function in neurons, cardiomyocytes, and cancer cells under stress [98]. For example, overexpression of *MFN2* in hepatocellular carcinoma cells promotes mitochondrial fusion and a rapid metabolic shift from glycolysis to oxidative phosphorylation [13]. Hence, the response seen here for the RACK1 KD LG may be associated with the LG medium [73]. While the expression of nuclear fusion/fission proteins is useful for mitochondrial analysis, all four mediators panelled in this study exist in multiple isoforms and undergo a range of PTMs [8]. Protein expression analysis via immunoblotting should be conducted to better visualize how RACK1 KD impacts mitochondrial function in these cells and confirm the RT-qPCR results above. This will support future investigation of how RACK1 KD impacts mitochondrial network dynamics.

4.1.4 RACK1 knockdown impacts the expression of numerous nuclear proteins that localize to the mitochondria to support mitochondria structure and function

RACK1 KD dysregulated 237 genes associated with mitochondrial function. Mitochondrial categories with significant enrichment included ETC components, MRPs, and mitochondrial carrier proteins (Figure 5.5A). Decreases in ETC component expression and mitochondrial membrane-associated carrier molecules in *Saccharomyces cerevisiae* was reported by Rachfall et al. (2013) [115]. Over 50% of all proteins that were impacted by loss of Asc1 were MAPs, including proteins involved in energy metabolism, biogenesis/respiration genes, and inner membrane translocation genes [115]. This phenomenon was also described by Cardenas et al. (2015) [19], who found that *Leishmania* strains deficient for LACK/RACK1 displayed a substantial depletion of ETC subunits, resulting in compromised mitochondrial function. These findings reassert the potential for a connection between a loss of RACK1 signaling and defects in mitochondrial energy metabolism expression.

RACK1 KD downregulated MRPLs and MRPS, translation initiation and release factors of the mitochondrial ribosome, and insertases for ribosomal co-translational

anchoring. The majority of the mitochondrial ribosome factors are nuclear-encoded, and problems with the nuclear ribosome negatively impact mitochondrial ribosomal function [7]. RACK1 is a core ribosomal protein on the 40S subunit that influences protein synthesis rates [102] and controls translation of specific mRNA subsets [102],[149]. RACK1/Asc1 KD decreases the translational efficiency of mitochondrial ribosomal protein mRNAs, resulting in substantial defects in mitochondrial protein synthesis [148]. This suggests an important role for RACK1 in supporting cellular respiration by promoting synthesis of mitochondrial ribosomal proteins through its influence on the nuclear ribosome. The idea that RACK1 may indirectly facilitate "crosstalk" between cytoplasmic and mitochondrial protein translation should be investigated further.

Replication and transcription factors are required to maintain mt-DNA levels and meet energy requirements of cells [159],[16]. In mitochondria, MRP expression is correlated with mt-DNA levels due to the detailed feedback loops surrounding mitochondrial biogenesis and oxygen consumption [23]. Nearly two-thirds of mitochondrial ribosomal genes are essential in the transcriptional and translational pathway maintaining optimal ETC chain functionality [37]. Even singular pathway defects cause devastating changes to mitochondrial function: single MRP knockouts cause rapid ETC component imbalance and decrease mitochondrial respiration [23]. Biogenesis mediators may influence MRP function as well. Increases in *PGC1α* stimulate the production of crucial ribosomal components *RNR1* and *RNR2* [157] and upregulate mitochondrial ribosome activity as a member of the OXPHOS 'rescue team' during the mitochondrial biogenesis response [158],[166]. Given the decrease in MRPs seen in these cells, we were curious if the mt-DNA levels were impacted by knockdown. Previous research has shown only linear relationships between RACK1 expression and mt-DNA levels. Both a decrease in RACK1 expression and a corresponding decrease mt-DNA expression have been identified [48], and mt-DNA increases in ALL cancer patients are correlated with heightened *GNB2L1* expression [24].

RACK1 KD HG cells had significant increases in *COX I, CytB, ND1, ND6, RNR1,* and *RNR2* levels (Figure 5.20A-F). Increased mt-DNA has a dual role in stress alleviation: it produces critical electron transport chain components that will increase ATP production, and elevated mt-DNA:nDNA ratios in the cell act as a positive feedback

loop that increase *PGC1α* expression [37].

RACK1 KD LG cells saw sweeping decreases in mt-DNA genetic expression levels compared to control, despite their increases in biogenesis mediators (Figure 5.20A-F). Interestingly, cells may utilize the "mitonuclear protein imbalance" [54] response to decreases in MRP levels. This process enacts the mitochondrial unfolded protein response, which destroys mt-DNA and overrides biogenesis signals [54].

4.1.5 Oxygen consumption in RACK1 KD HG and LG cells is lowered in spite of increased biogenesis demands

RACK1 KD dysregulated mt-DNA levels, biogenesis mediators, fusion/fission mediator activity and heavily fragmented the mitochondrial network in RACK1 KD cells. This suggested a dysregulated mitochondrial network synonymous with decreased mitochondrial functionality [163]. Our earlier cellular ATP measurements demonstrated a decrease in ATP levels, indicating that mitochondrial function in the cells may be impacted (Figure 5.9G) We measured RACK1 KD HG and LG mitochondrial bioenergetics through oxygen consumption rates. The analysis of metabolic flux revealed that RACK1 KD significantly decreased mitochondrial basal and maximal respiration (Figure 5.21B-C), as well as ATP production (Figure 5.21D), demonstrating reduced functional capabilities of mitochondria in these cells (Figure 5.21B-F). The decreased ATP levels were consistent with the cellular ATP production in RACK1 KD cells, where both RACK1 KD HG and LG had decreased ATP production (Figure 5.9G). In addition, the spare respiratory capacity was halved in both RACK1 KD HG and LG, indicating that the RACK1 KD cells had decreased ability to respond to stressors (Figure 5.21C). Thus far, no studies have focused directly upon how RACK1 KD impacts OCR levels in cells. However, the loss of some confirmed RACK1 interactors have been found to decrease OCR rates in cells. A study by Chou et al. (2021) [30] investigating RACK1-interacting protein AIM2 found that a decrease in *AIM2* expression results in a decrease in OCR parameters in CD4+ T cells. Similarly, Ren et al. (2023) [120] found that PHB2 knockdown significantly reduced OCR levels in colorectal cancer cells. These results suggest that further investigation of how RACK1 is involved in the maintenance of efficient mitochondrial oxygen consumption is worth exploring.

Chapter 5

Conclusion

5.1 Final thoughts

5.1.1 The RACK1-mitochondria axis

Our characterization of RACK1 KD cells revealed that RACK1 KD cells have decreased ATP output and experience difficulty proliferating. Mitochondria in RACK1 KD cells revealed increased incidences of structural damage and loss of network connectivity. Further functional investigation revealed dysfunctional mitochondrial fusion and fission mediator expression, changes in biogenesis mediators expression, and shifts in mt-DNA levels. The specific differences that emerge from the RACK1 KD HG versus the RACK1 KD LG cells are detailed in Figure 5.22B.

The RACK1 KD HG cell phenotype appears similar to that of stressed cells encountering mitochondrial dysfunction. These mitochondrial networks upregulate mitochondrial biogenesis, perturb fusion/fission dynamics, and increase mt-DNA levels in the cell [61]. Following RACK1 KD, mitochondria begin to experience increasingly dysfunctional ETC chain activity, as indicated by decreasing oxygen consumption and mitochondrial respiration parameters. This will gradually create a bioenergetic deficit and sub-optimal ATP synthesis in these tissues, triggering a compensatory response to increase biogenesis [152]. Upregulated *PGC1α* expression will drive increased *TFAM* expression, resulting in increased mt-DNA levels [142]. The subsequent increase in mt-DNA in the stressed cell has a dual role in stress alleviation: it codes for critical electron transport chain components, which will be rapidly produced to meet increased energy needs; and the elevated mt-DNA:nDNA ratios in the cell will also act as a positive feedback loop that drives further increases in PGC1α expression [159]. As mitochondrial biogenesis and ETC component production increases, the mitochondrial network incurs changes to fusion/fission patterns in response to the

stress. If the mitochondria are dysfunctional, fusion is abruptly halted and the network will preferentially undergo fission to remove dysfunctional regions [104]. This results in a fragmented network. However, mutations in mitochondrial proteins resulting from a dysfunctional mitochondrial ribosome impact the entire mitochondrial network. The increasingly dysfunctional mitochondria become less and less able to provide the services required by the cell, resulting in increased cellular stress and in extreme cases, the beginning of disease pathologies [104]. Mitochondria then begin to build in the cell, either due to a lack of mitochondrial clearance from mitophagy dysfunction or from excessive biogenesis. The RACK1 KD LG cells may be blocked from fully extending this response due to the change in nutrient levels in these cells; this is well-recognized as an exacerbating factor for the RACK1 KD phenotype [148]. Despite the lack of literature evidence surrounding how RACK1 KD impacts mitochondrial OXPHOS capabilities, the response of the RACK1 KD HG cells seen here suggests that the role of RACK1 KD and ETC chain dysfunction should be examined more critically.

5.1.2 Study limitations and future directions

Some of the study limitations that were encountered over the course of this study was the lack of uniform randomization, which is critical for the unbiased quantification of microscopy images. The RACK1 KD cellular phenotype was so distinctive that it presented a major hurdle when collecting and analyzing images; blinding could not be applied to cellular imaging collection and analysis (Figure 5.7, Figure 5.8). For TEM, bias was minimized by selecting "squares" within the prepared slides that were images regardless of sample type, and during quantification all images regardless of cellular presentation were included in analysis. During confocal microscopy, cells were imaged on the same settings. Analysis was completed using Imaris computer algorithms in "batch format" to process all photos equally. However, to fully remove bias, future analysis could be better blinded by using an outsider to the project to collect images for analysis. Another study limitation that was encountered was our selection of HeLa cells to model mitochondria responses to RACK1 KD. More mitochondrially-dependent cells, such as a hepatic cell line with greater mitochondrial content, could serve to further elucidate the RACK1 KD phenotype for mitochondria

[35]. Finally, the fusion and fission mediator expression levels in both cell sets were inconsistent across replicates. Immunoblotting should be substituted for RT-qPCR in future investigations to confirm the expression and post-translational modifications of the fusion/fission mediators.

The exciting results seen in this study indicate that there is far more to be done to better describe RACK1's relationship with mitochondrial function. The future directions for this study should start by immunoblotting the mitochondrial MRPs to confirm decreased expression. In addition, the MAPs associated with this study included a broad variety of ETC chain components; blotting for those to determine the extent of their downregulation would be useful to confirm the suspected impact of RACK1 upon subunit expression, which could help highlight the role of RACK1 KD on ETC activity. Finally, mitochondrial membrane parameters including calcium flux, ROS levels, and mitochondrial membrane potential should be investigated to better understand how the ETC and inner membrane is impacted by RACK1 KD.

RACK1 activity mediates various cellular signaling cascades that support crucial biological functions. The relationship between RACK1 expression and mitochondrial function remains highly under-investigated. To better characterize this relationship, we decided to investigate the impact of RACK1 KD expression on mitochondrial physiology. We have demonstrated here that a decrease in RACK1 expression in the cell causes a variety of changes in major mitochondrial physiological parameters, including membrane dynamics, network connectivity, energy production, and mt-DNA expression. These results highlight how important further characterization of the RACK1 interactome is for our future understanding of its influence over cellular function, and its role in disease.

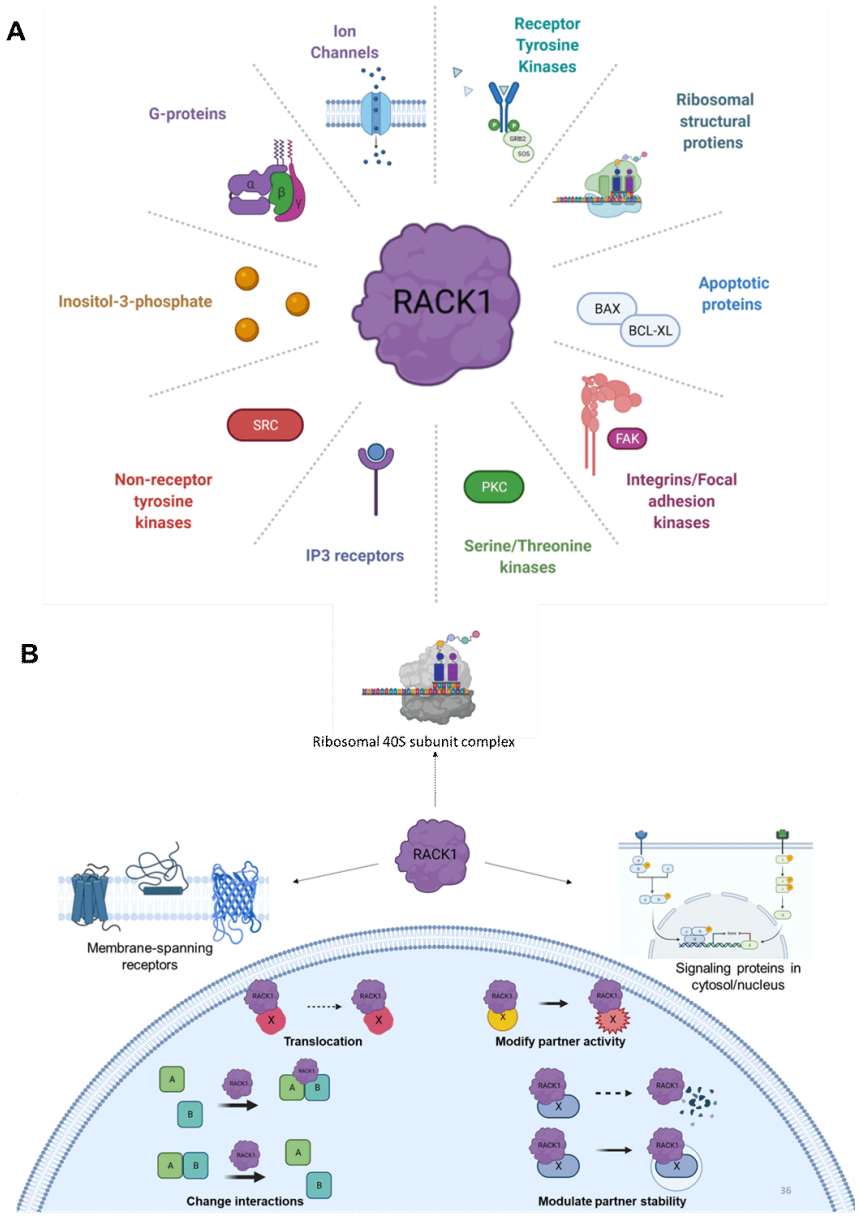

Figure 5.1: **RACK1 is a scaffolding protein capable of many interaction types. (A).** RACK1 has diverse roles and acts as a signaling hub critical in numerous scaffolding protein complexes with a broad range of interactors. In **(B)**, the workflow for protein-protein interactions with RACK1 is outlined. Three major classes of interactors are identified: (i) the cytosolic domains of membrane-spanning receptors, (ii) the signaling proteins in cytoplasm and nuclei, and (iii) organellar partners. The interaction of RACK1 with these molecular players can be classified into four types: (i) shuttle its partners from among sites, (ii) modify partner activity, (iii) change intermolecular interactions, and (iv) modulate binding protein stability.

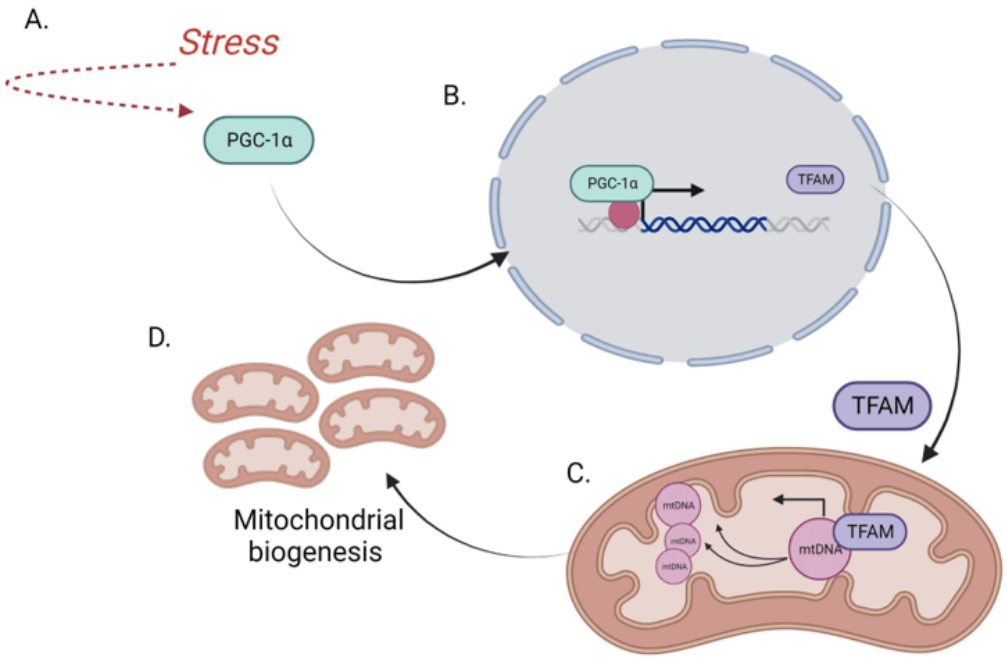

Figure 5.2: **Schematic representation of mitochondrial biogenesis. (A).** Stressors (nutrient deprivation, hypoxia, oxidant stress, or exercise) activate PGC1α, causing its relocation from the cytoplasm to the nucleus. **(B).** Activated PGC1α works with other nuclear mediators (NRF1 and NRF2) to stimulate the synthesis of TFAM, **(C)** which subsequently mediates mt-DNA replication and transcription. **(D).** The increase in mt-DNA levels will contribute to the formation of new mitochondria.

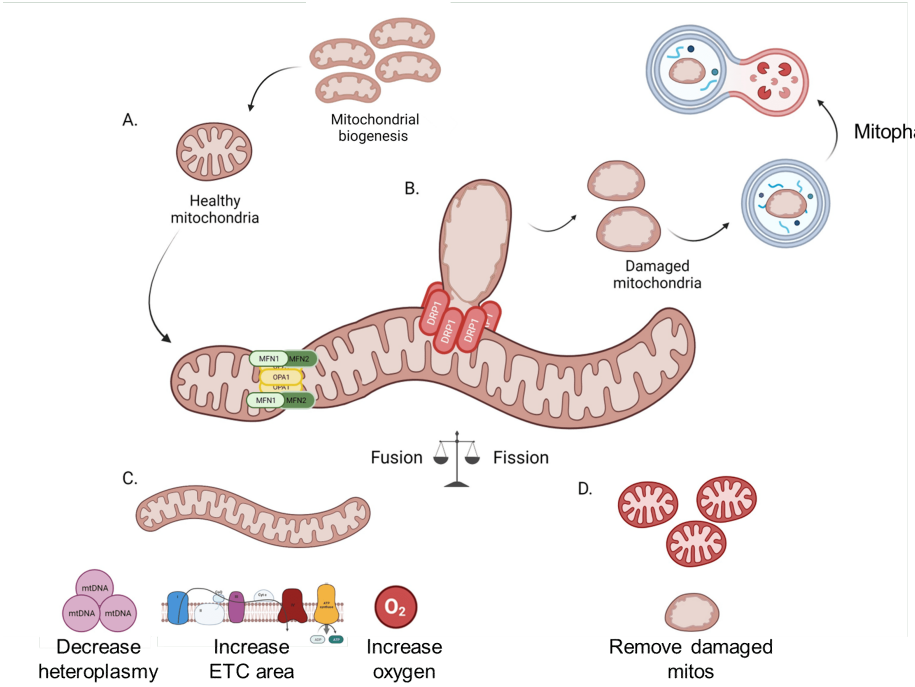

Figure 5.3: **Schematic representation of fusion/fission dynamics in mitochondrial networks. (A).** Following biogenesis, new healthy mitochondria will fuse with the mitochondrial network. Fusion of the inner and outer mitochondrial membranes is mediated by optic atrophy 1 (OPA1) and mitofusins 1 and 2 (MFN1/2), respectively. **(B).** Dysfunctional mitochondria are removed through fission, which is managed via the dynamin-related protein 1 (DRP1) and a host of its interactor proteins. Fission removes dysfunctional mitochondria that are then targeted for degradation by mitophagy. **(C-D).** Fusion and fission mediate different, but critical, roles that must both be seamlessly balanced for optimal management of a healthy mitochondrial network.

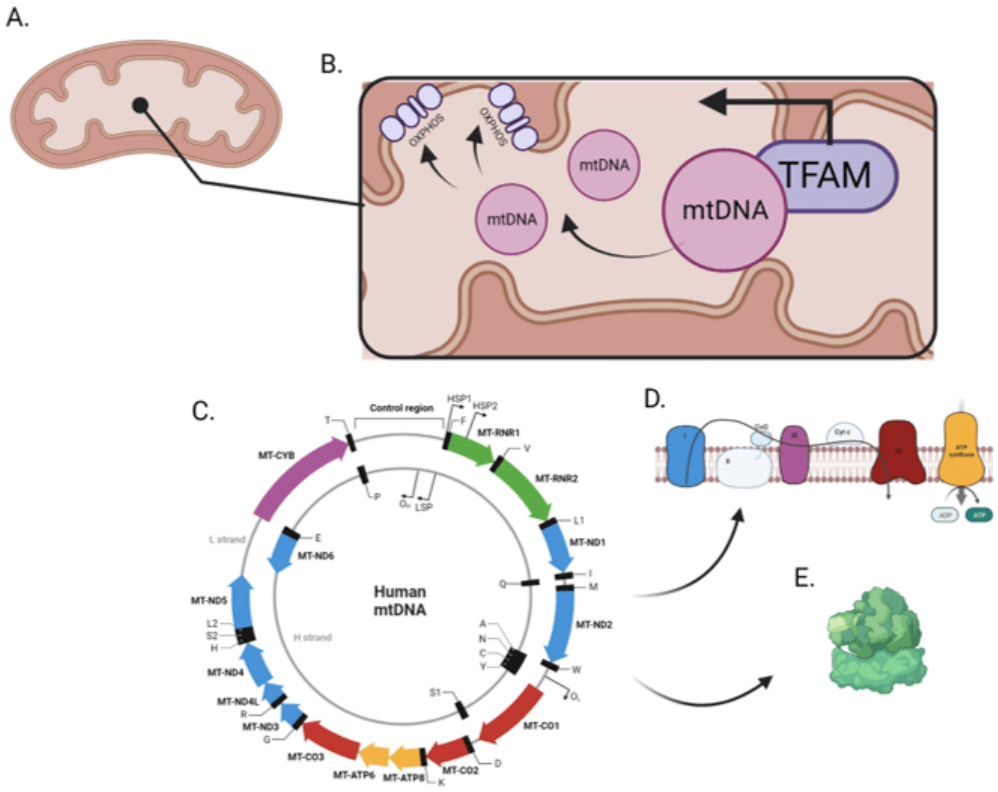

Figure 5.4: **Schematic representation of mt-DNA form and encoded units. (A-B).** TFAM levels mediate mt-DNA replication and transcription. **(C).** The mitochondrial genome encodes 37 genes: 2 rRNA (seen in **(E).**), 22 tRNA, and 13 OXPHOS polypeptides. **(D).** All polypeptides code for components of the mitochondrial oxidative phosphorylation (OXPHOS) system. Seven polypeptides contribute to the OXPHOS complex I (CI), one polypeptide contributes to complex III (CIII), three polypeptides contribute to complex IV (CIV), and two polypeptides contribute to complex V (CV).

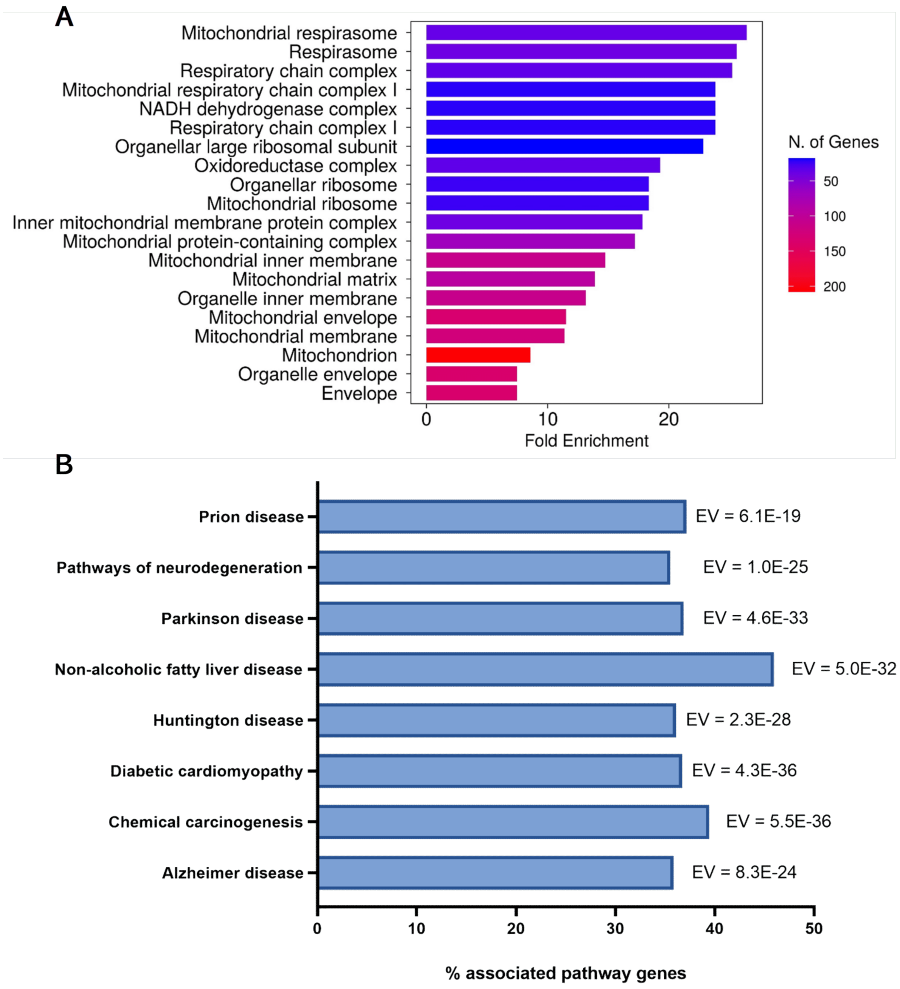

Figure 5.5: **RNA-seq analysis in RACK1 KD HeLa cells.** A list of DEGs in RACK1 KD HG cells were assessed for MAPs. The following 237 MAPs in the RACK1 KD HG dataset were analyzed with SHINYGO 0.77 to identify statistical enrichments for specific GO terms from the cellular component annotation. Categories with high enrichment in the sample set included **(A).** i) Mitochondrial protein synthesis, (translation initiation/elongation/and termination); ii) Mitochondrial respiration components, (ETC components/carrier proteins); and iii) Mitochondrial membranes (management and transport). X axis = fold enrichment of pathway in RACK1 KD versus control. Number of genes from dataset associated with cellular component are denoted in blue-red color gradient. **(B).** Histogram denoting statistical enrichment for disease pathways. X- axis = % genes active in disease state that were enriched in curated RACK1 KD MAP dataset. EV = enrichment value.

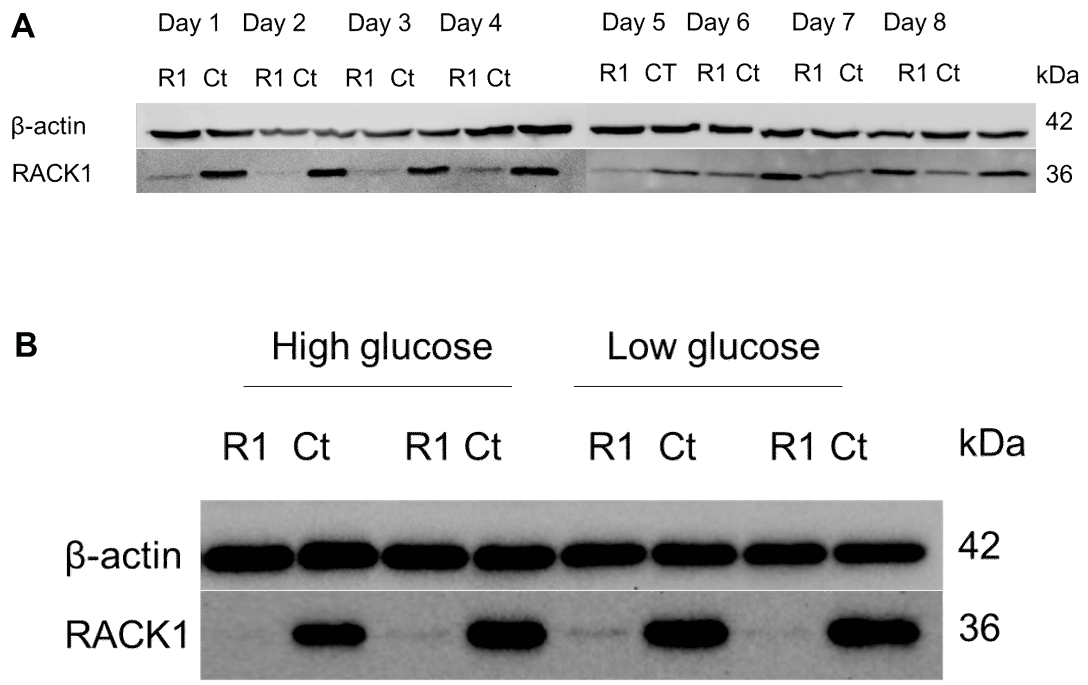

Figure 5.6: **Western blot confirmation of RACK1 KD in HeLa cells. (A)**. Success of siRNA-mediated RACK1 KD was measured for 8 days post-knockdown to confirm knockdown efficacy. **(B).** Western blot confirmation of RACK1 KD in HG and LG conditions. Data is representative of the confirmation blots that accompanied all knockdowns performed in this study. kDa = kilodaltons.

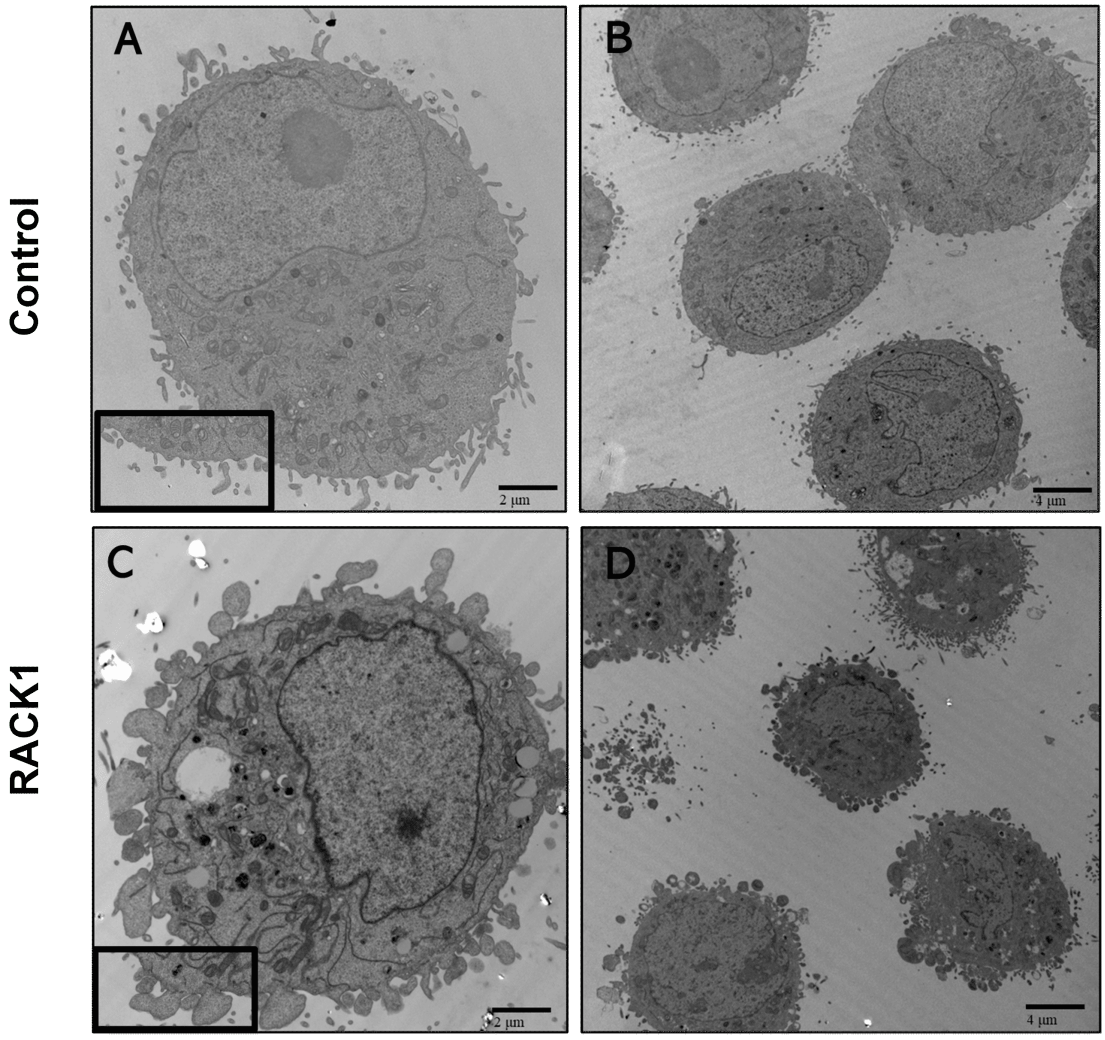

Figure 5.7: **Effects of RACK1 KD on HeLa cell morphology in HG media**. TEM images taken of RACK1 KD HG and control HG cells. **(A-B)** = Control cells (labelled 'control'). **(C-D)** = RACK1 KD cells (labelled 'RACK1'). **(A).** Control at 8X magnification exhibiting smooth cell membrane with consistent punctuated protrusions (inset in bottom left corner highlights membrane structure) and cytoplasm filled with organelles **(B).** Control HG cells at 4X magnification demonstrate consistent smooth membranes and regular filopodia throughout population. **(C).** RACK1 KD HG cell at 8X magnification demonstrates loss of cellular integrity with irregular circular protrusions along cell border (inset in bottom left corner highlight membrane structure) and cytoplasm packed with many irregular cell components **(D).** RACK1 KD HG cells at 4X magnification show these membrane defects throughout the population. Data is representative of 3 independent experiments. Scale bars = 2 μM in A, C, and 4 μM in B, D.

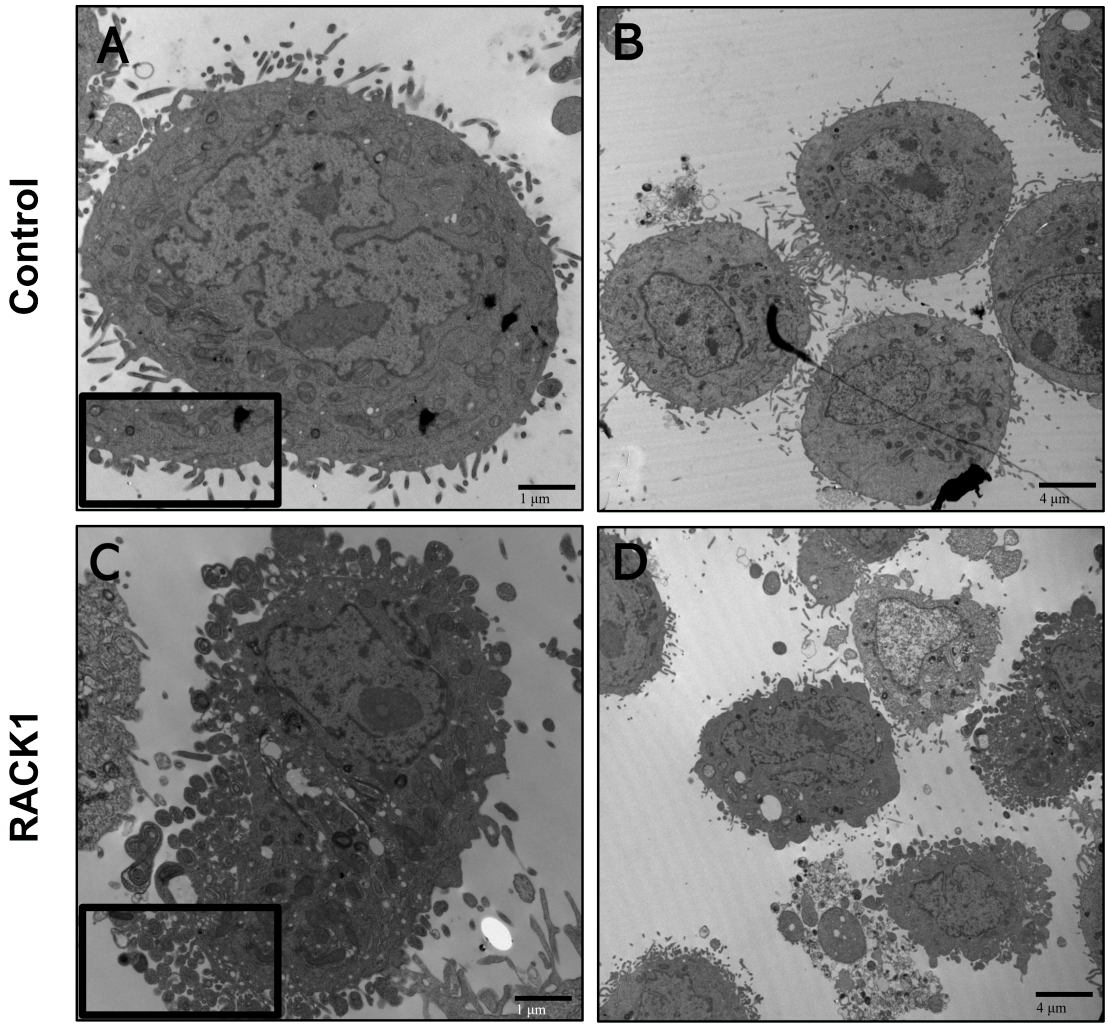

Figure 5.8: **Effects of RACK1 KD on HeLa cell morphology in LG media.** TEM images taken of RACK1 KD LG and control LG cells. **(A-B)** = Control cells (labelled 'control') and **(C-D)** = RACK1 KD cells (labelled 'RACK1'). **(A).** Control at 8X magnification exhibiting smooth cell membrane with consistent punctuated protrusions (inset in bottom left corner highlights cell membrane structure) and cytoplasm filled with organelles **(B).** Control HG cells at 4X magnification demonstrate consistent smooth membranes and regular filopodia throughout population. **(C).** RACK1 KD LG cell at 8X magnification demonstrates loss of cellular integrity with extremely large, irregular circular protrusions along cell border (inset in bottom left corner highlight membrane structure) and cytoplasm packed with many irregular, dark cell components **(D).** RACK1 KD LG cells at 4X magnification show these consistent membrane defects throughout the population. Data is representative of 3 independent experiments. (A,C) Scale bars = 1 μM . (B,D) scale bars= 4 μM.

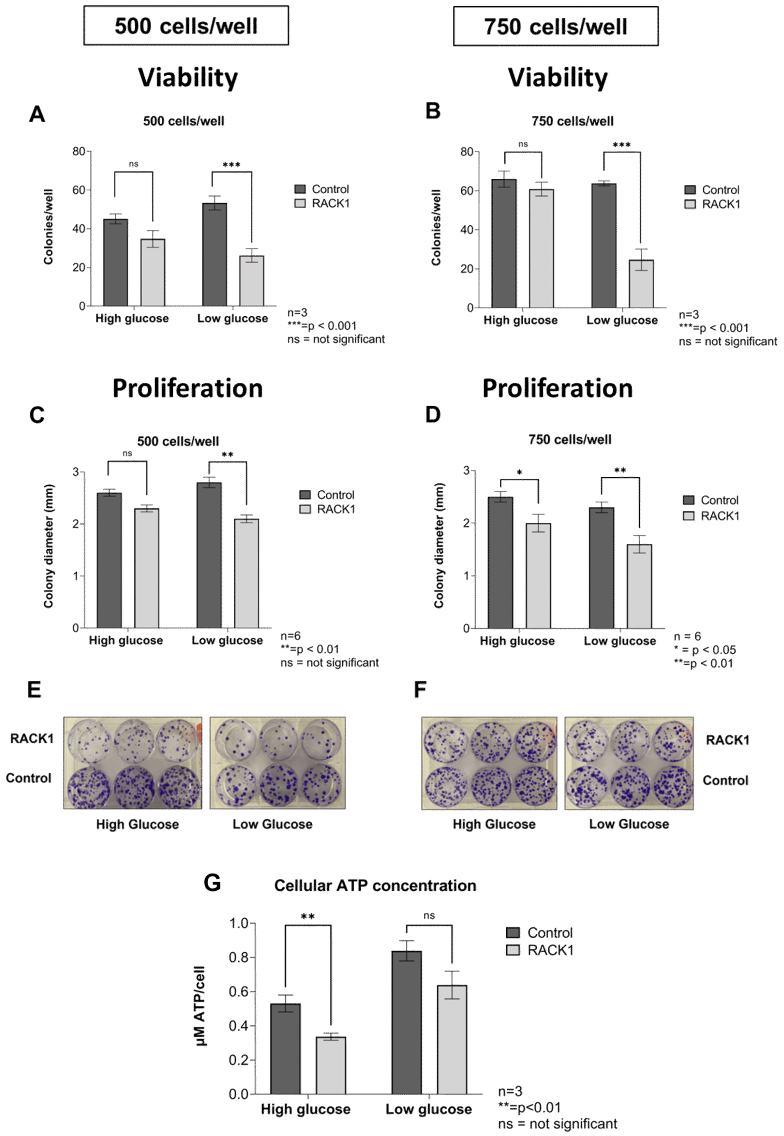

Figure 5.9: **RACK1 KD cells experience decreased viability, proliferation, and energy production.** RACK1 KD and control HG and LG cells seeded at 500 and 750 cells/well were grown for 2 weeks and assessed for changes in viability and proliferation. **(A,C)** = 500 cells/well and **(B,D)** = 750 cells/well. **(A-D)**. colony viability (number of colonies/well) and colony size (diameter (mm)/colony) were measured for both seeding densities. RACK1 KD HG and LG cells experienced decreases in viability and proliferation. **(E-F).** Examples of completed clonogenic assays (E). 500 cell/well seeding density result for RACK1 KD/Control HG/LG (not shown to scale) (F). 750 cells/well seeding density for RACK1 KD/Control HG/LG (not shown to scale). **(G).** Cellular ATP measurements reveal a decrease in ATP levels. Results are from 3-6 independent experiments where 1 experiment = average of 3 wells/plate. 1000-cell seeding densities are not pictured. Data presented as mean ± s.e.m, * = P $\leq$ 0.05, ** = P $\leq$0.01, *** = P $\leq$0.001.

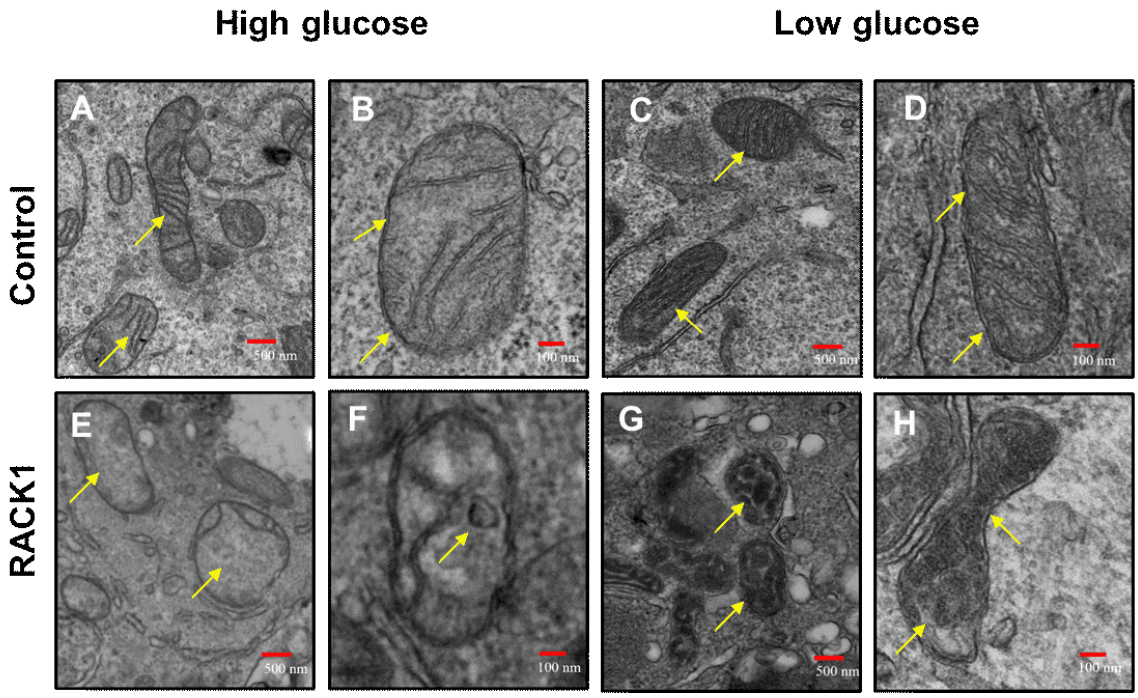

Figure 5.10: **TEM analysis of mitochondria reveal RACK1 KD cells have a higher incidence of undesirable mitochondrial morphology.** Mitochondrial ultrastructural analysis for RACK1 KD HG/LG and Control HG/LG. **(A-D)**= Control cells (labelled 'control'). **(E-H)** = RACK1 KD cells (labelled 'RACK1'). **(A-B, E-F)** = HG condition (labelled "high glucose"). **(C-D, G-H)** = LG condition (labelled "low glucose"). **(A).** Control HG mitochondria demonstrate lamellar, long cristae that span the matrix (highlighted by yellow arrows). **(B).** Control HG mitochondria demonstrate a continuous, smooth double membrane (highlighted by yellow arrows). **(C).** Control LG mitochondria demonstrate lamellar, long cristae that span the matrix (highlighted by yellow arrows). **(D).** Control LG mitochondria demonstrate a continuous, smooth cell membrane and double membrane (highlighted by yellow arrows). **(E).** RACK1 KD HG mitochondria are bloated and lack cristae (highlighted by yellow arrows). **(F).** RACK1 KD HG mitochondria show dark inclusions in matrix (highlighted by yellow arrow). **(G).** RACK1 KD LG mitochondria are small/fragmented with dark condensed bodies in inner membrane (highlighted by yellow arrows). **(H).** RACK1 KD LG mitochondria are shrunken and have blackened condensed matrix (highlighted by yellow arrows). Data is representative of 3 independent experiments. Image magnifications: **(A, C, E)**= 60X (scale bar = 500 nm); **(F, G)** 40X (F = zoomed, scale bar = 100 nm; G = no zoom, scale bar = 500 nm). (B, D, H) = 80X (scale bar = 100 nm).

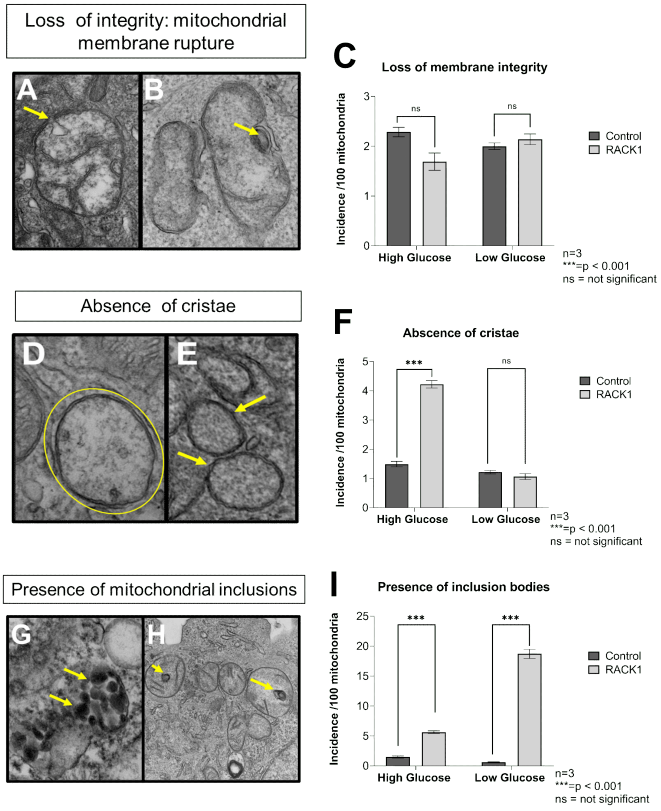

Figure 5.11: **Quantitation of deleterious morphology within RACK1 KD mitochondria** . The ultrastructural features of RACK1 KD HG and LG mitochondria membranes and matrix were examined for signs of mitochondrial damage. **(A-B).** TEM example of mitochondrial membrane integrity loss depicted by outer/inner membrane rupture, (characterized as loss of inner/outer membranes in-plane). (highlighted by yellow arrows). **(C).** Quantification of membrane integrity loss incidences between RACK1 KD and control cells. **(D-E).** TEM example of cristae loss (characterized by lack of visible cristae in mitochondrion with inner/outer membranes in-plane (membrane highlighted with yellow circle; highlighted by yellow arrows). **(F).** Quantification of cristae loss incidences between RACK1 KD and control cells. **(G-H).** TEM example of mitochondrial inclusion bodies (characterized by black granular structure within mitochondrion double membrane, highlighted by yellow arrows). **(I).** Quantification of mitochondrial inclusion numbers between RACK1 KD and control cells. Data in graphs was normalized to total mitochondria in panels of respective sample. **(A, B, D, E, H)** = RACK1 KD HG samples. **(E)**= RACK1 KD LG sample. Image magnifications: **(A, B, D, G)** = 80X. **(E,H)** taken at 40X. Images are enlarged to show regions of interest and are not represented to scale. Results are representative of 3 independent experiments. Data presented as mean ± s.e.m, * = P $\leq$ 0.05, ** = P$\leq$0.01, *** = P$\leq$0.001.

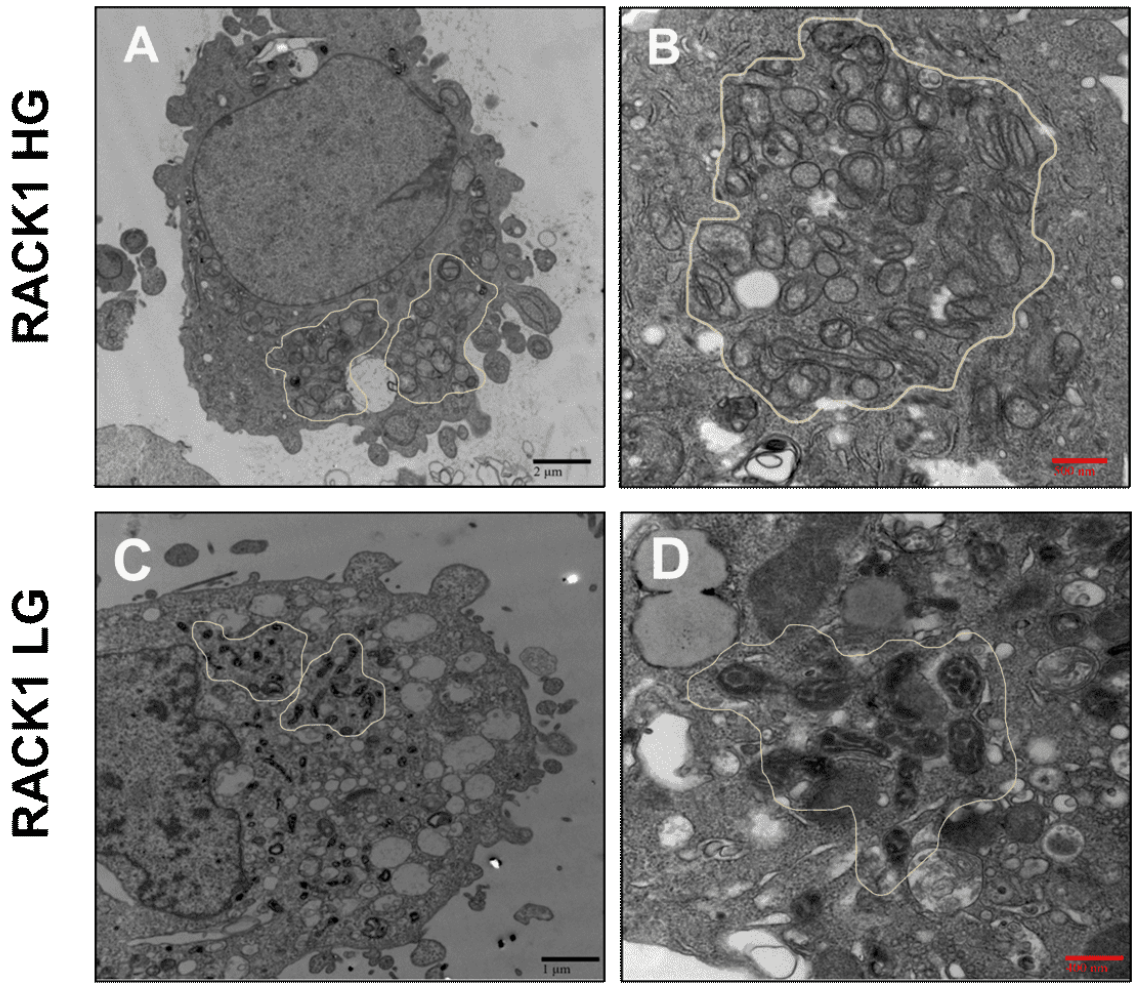

Figure 5.12:
RACK1 KD HG cells exhibit increased mitochondrial numbers. Large numbers of mitochondria clumped into groups were recorded in RACK1 KD HG cells. **(A-B)** = RACK1 KD HG cells (labelled 'RACK1HG'). **(C-D)** = RACK1 KD LG cells (labelled 'RACK1LG'). **(A).** Large numbers of mitochondria in RACK1 KD HG cells (groups of increased mitochondrial density outlined in beige). **(B).** Example of a "dumping ground" where large numbers of mitochondria are clumped together (groups of increased mitochondrial density outlined in beige). **(C).** RACK1 KD LG demonstrate similar clumping patterns of increased mitochondrial density outlined in beige. **(D).** Example of a "dumping ground" in the RACK1 KD LG (groups of increased mitochondrial density outlined in beige). Results are representative of 3 independent experiments. Image magnifications: **(A)** = 10X (scale bar = 2 μM); **(C)** = 20X (scale bar = 1 μM) **(B, D)** = 60X (scale bar = 400 nm).

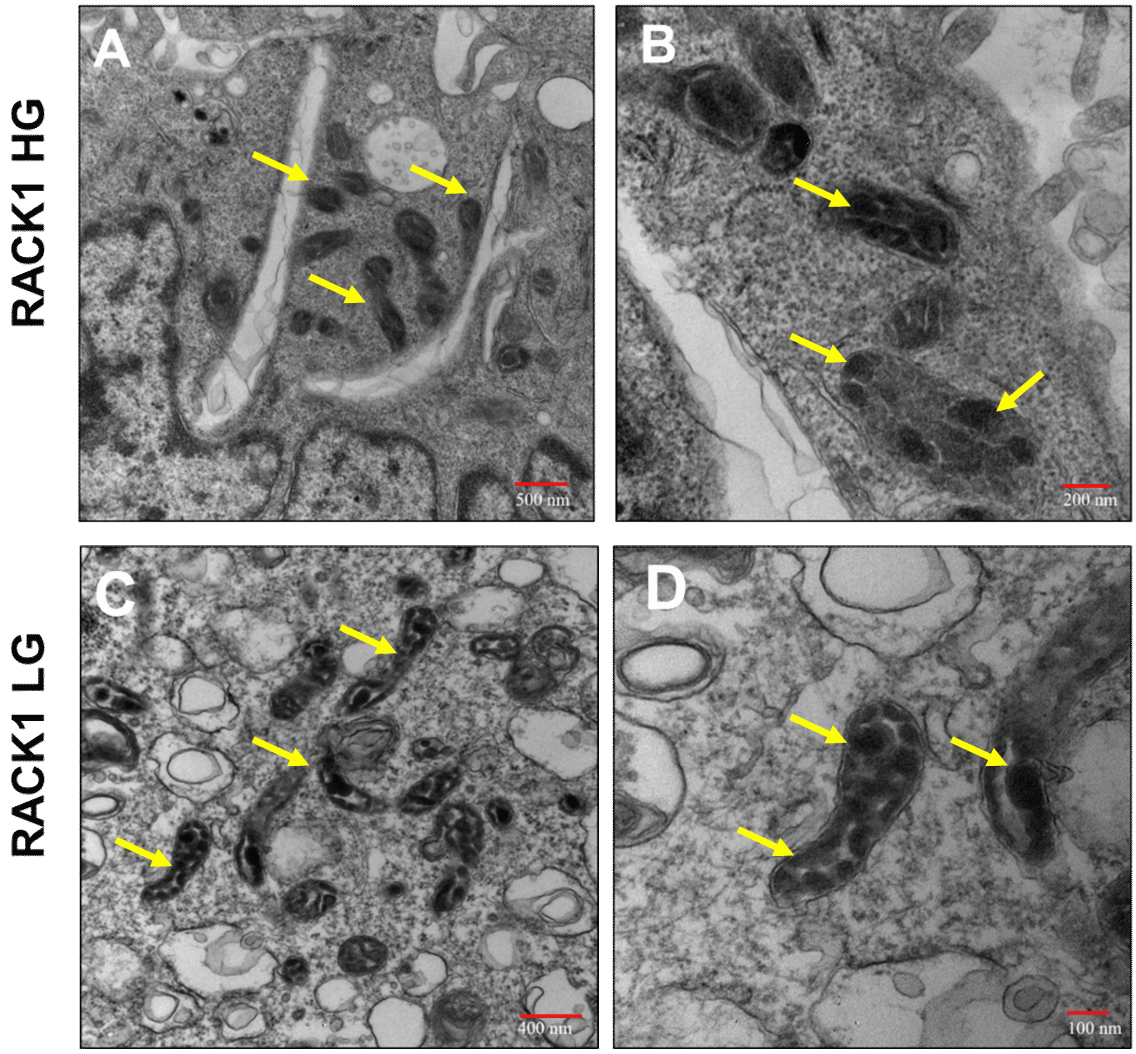

Figure 5.13:
RACK1 KD LG display a unique inclusion body phenotype. Ultrastructural TEM image analysis of RACK1 KD HG and LG cells revealed a unique phenotype in RACK1 KD LG mitochondria. **(A-B)** = RACK1 KD HG cells (labelled 'RACK1HG'). **(C-D)** = RACK1 KD LG cells (labelled 'RACK1LG'). **(A-B)** . Unbalanced increases in matrix density in RACK1 KD HG cells (highlighted by yellow arrows). **(C-D).** RACK1 KD LG mitochondria have darkened and dense matrices filled with circular black inclusion bodies (highlighted by yellow arrows). Results are representative of 3 independent experiments. Image magnifications: **(A, B)** = 40X (scale bar = 500 nm, 400nm, respectively). **(C)**= 80X (scale bar = 200 nm) **(D).**taken at 100X (scale bar = 100 nm).

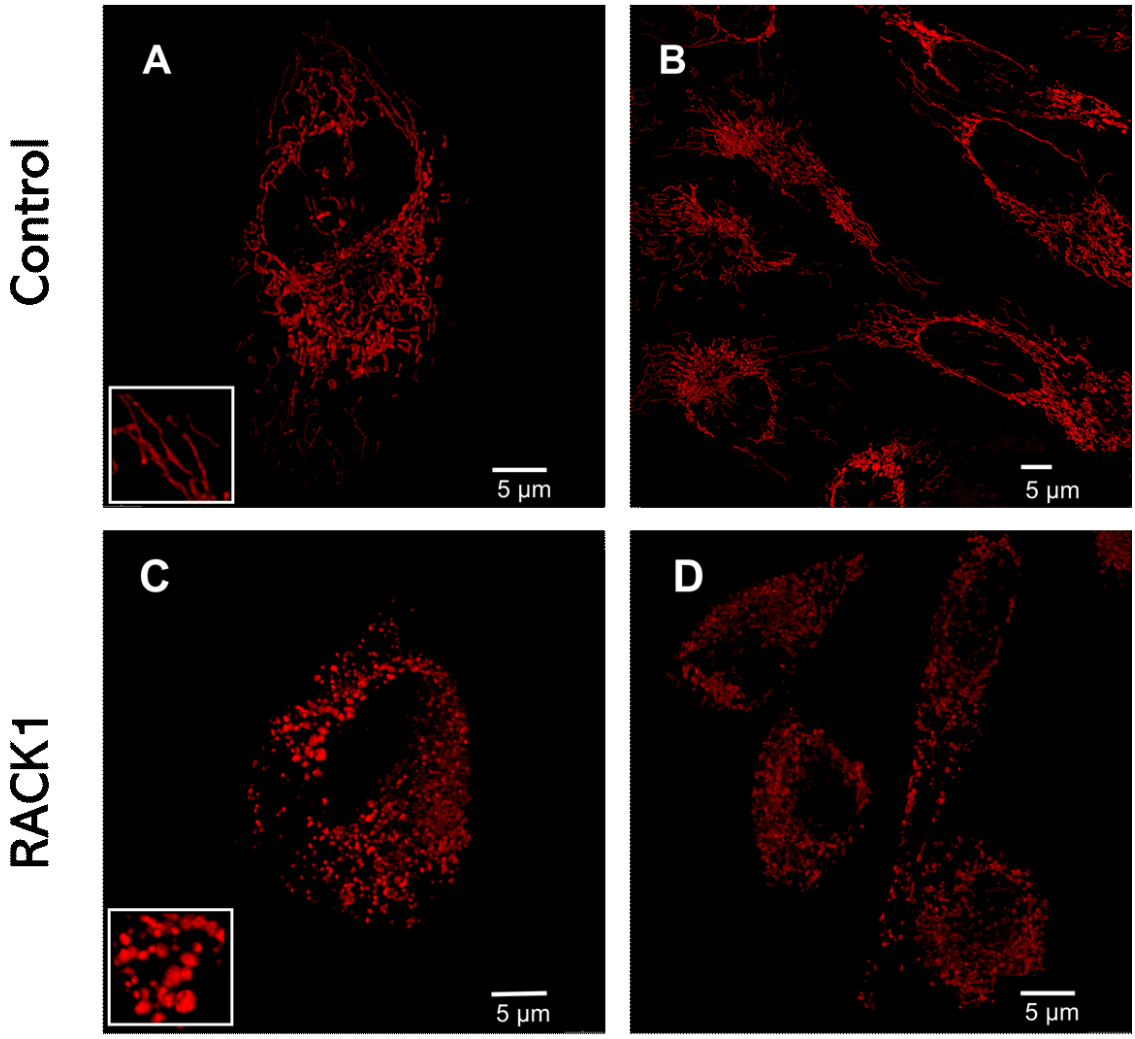

Figure 5.14: **Live mitochondrial network dynamics in RACK1 KD HG cells.** Confocal microscopy images of live RACK1 KD HG and control HG cells stained in mitotracker to highlight mitochondrial networks. **(A-B)** = control cells (labelled 'control') and **(C-D)** = RACK1 KD cells (labelled 'RACK1'). **(A)**. Control cell contains large branching networks of mitochondria spanning the cell. **(B).** Mitochondrial phenotype in Control HG cells is consistent in population. **(C).** The RACK1 KD HG mitochondrial networks show less connectivity and increased fragmentation that spans the cell. **(D).** Mitochondrial phenotype in RACK1 KD HG cells is consistent in population. Results are representative of 3 independent experiments. Image magnifications : **(A-B)** = 93X (with zoom applied) **(C-D)** = taken at 93X. **(A-D)** scale bars = 10μM.

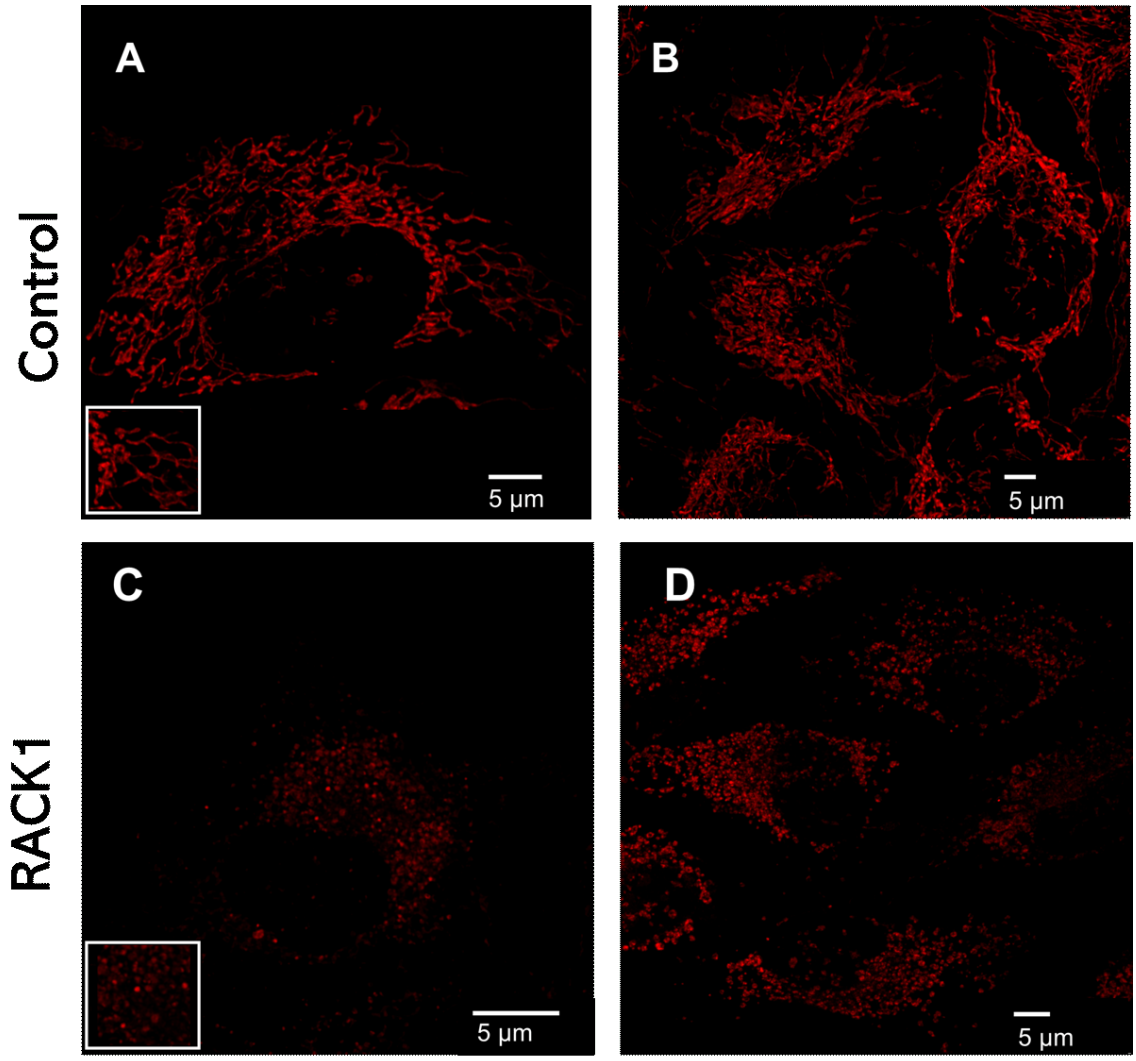

Figure 5.15: **Live mitochondrial network dynamics in RACK1 KD LG cells.** Confocal microscopy images of live RACK1 KD LG and control LG cells stained in mitotracker to highlight mitochondrial networks. **(A-B)** = control cells (labelled 'control'). **(C-D)** = RACK1 KD cells (labelled 'RACK1'). **(A)**. Control cell contains large branching mitochondrial networks spanning the cell. **(B).** Mitochondrial phenotype in Control LG cells is consistent in population. **(C).** The RACK1 KD LG mitochondrial networks show loss of connectivity and increased fragmentation spanning the cell. **(D).** Mitochondrial phenotype in RACK1 KD LG cells is consistent in population. Results are representative of 3 independent experiments. Image magnifications: **(A-B)** = 93X (zoom applied) **(C-D)** = 93X. **(A-D)** scale bars = 10 μM.

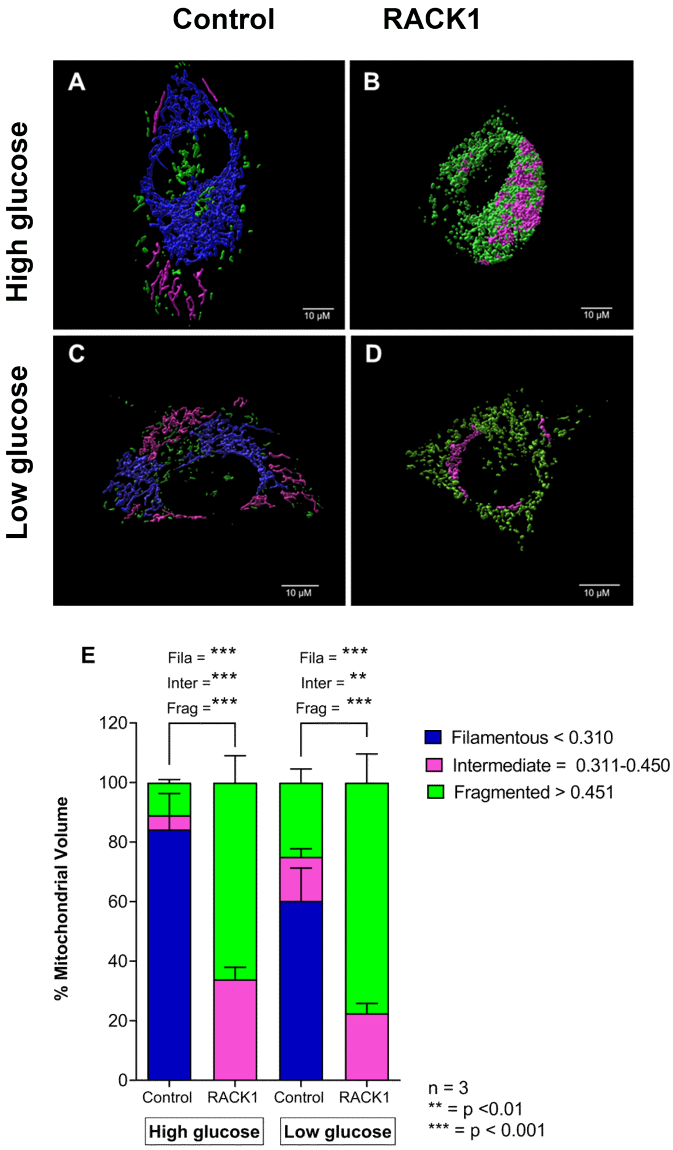

Figure 5.16: **Mitochondrial network characterization of RACK1 KD cells and controls.** Surface overlays color-coded to represent sphericity values of mitochondrial components were used to determine overall network character of cells. **(A,C)** = control cells (labelled 'control') and **(B,D)** = RACK1 KD cells (labelled 'RACK1'). Highly filamentous, interconnected networks with low spherical values = blue; intermediate values = pink; fragmented networks with high spherical values = green. **(A).** Control HG cell spherical values. **(B).** RACK1 KD HG cell spherical values. **(C).** Control LG cell spherical values. **(D).** RACK1 KD LG cell spherical values. **(E-F).** Bar graphs representing the proportion (%) of each spherical group (defined by spherical group's total mitochondrial volume/total mitochondrial volume). Results from 3 independent experiments are shown. Data presentation is mean ± s.e.m. * = P $\leq$0.05, ** = P$\leq$0.01, *** = P $\leq$0.001. (A-D) scale bars = 10 μm.

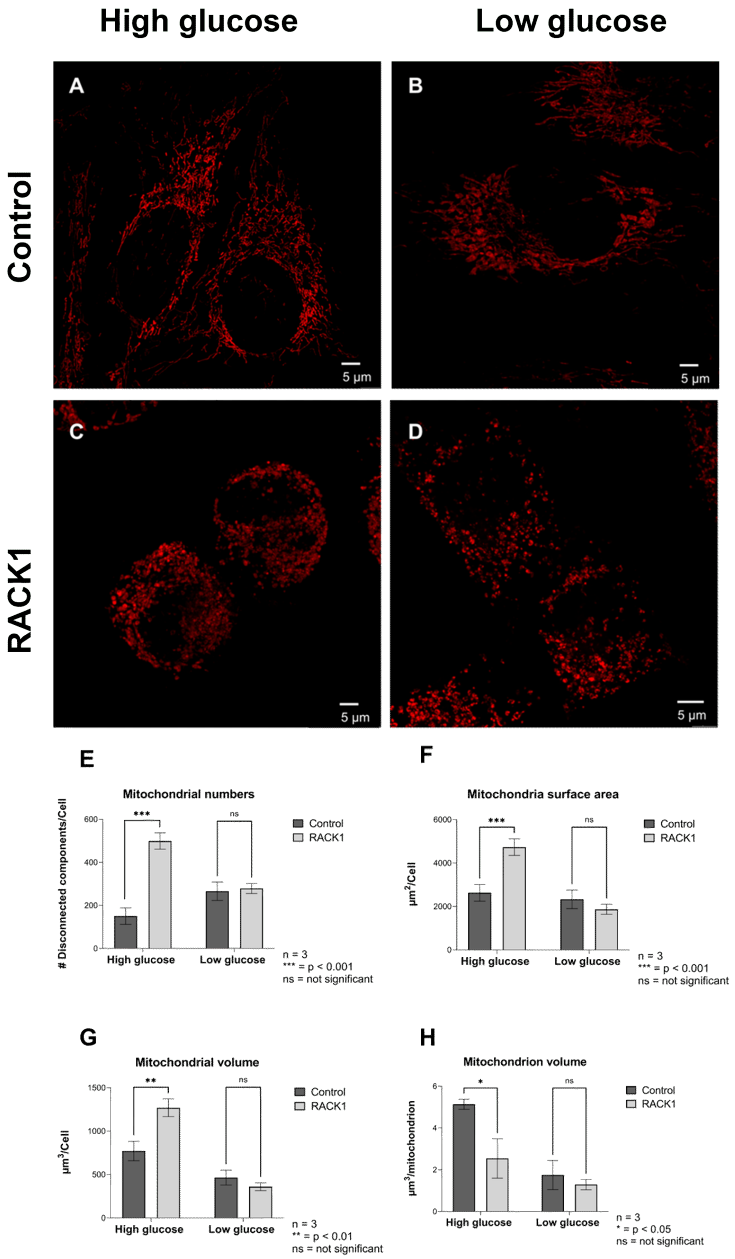

Figure 5.17: **Mitochondrial network parameters comparison between RACK1 KD and control cells**. **(A-B)** = control cells (labelled 'control') and **(C-D)** = RACK1 KD cells ('labelled RACK1'). Mitochondrial network parameters for RACK1 KD cells and control including mitochondrial numbers **(E)**, average surface area **(F),** total mitochondrial volume **(G)** and mean mitochondrion volume **(H)**. Results shown are from 3 independent experiments. Image magnifications: **(A-B)** = 93X. **(C-D)** = 93X. Scale bars **(A-D)** = 10 μm. Data presentation is mean $\pm$ s.e.m,* = P $\leq$0.05, ** = P$\leq$0.01, *** = P $\leq$0.001.

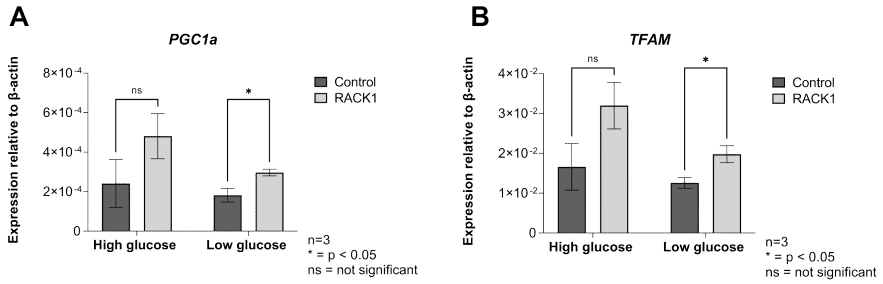

Figure 5.18: **Mitochondrial biogenesis upregulation in RACK1 KD cells.** Mitochondrial biogenesis mediator *PGC1α* and *TFAM* expression was measured in RACK1 KD cells and controls. **(A.)** PGC1α levels were increased in both RACK1 KD HG and LG compared to respective controls. **(B).** *TFAM* levels were increased in both RACK1 KD HG and LG compared to the controls. Expression is reported for both RACK1 KD and controls as expression relative to β-actin levels in those samples. Results from 3 independent experiments are shown. Data presentation is mean $\pm$ s.e.m. * = P$\leq$0.05, ** = P $\leq$0.01, *** = P $\leq$0.001.

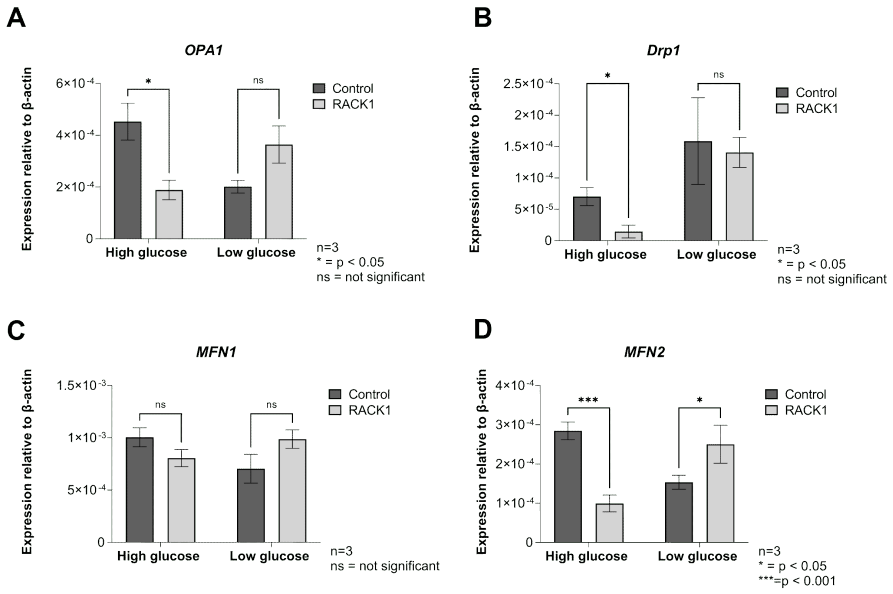

Figure 5.19: **Expression of mitochondrial fusion and fission mediators in RACK1 KD cells.** Nuclear expression of **(A)** *OPA1*, (**B**) *Drp1* , **(C)** *MFN1*, and **(D)** *MFN2* was measured in RACK1 KD/controls HG/LG. Expression for both RACK1 and control is reported as expression relative to β-actin levels in the samples. Results from 3 independent experiments are shown. Data presentation is mean$\pm$ s.e.m. * = P $\leq$0.05, ** = P $\leq$0.01, *** = P$\leq$0.001.

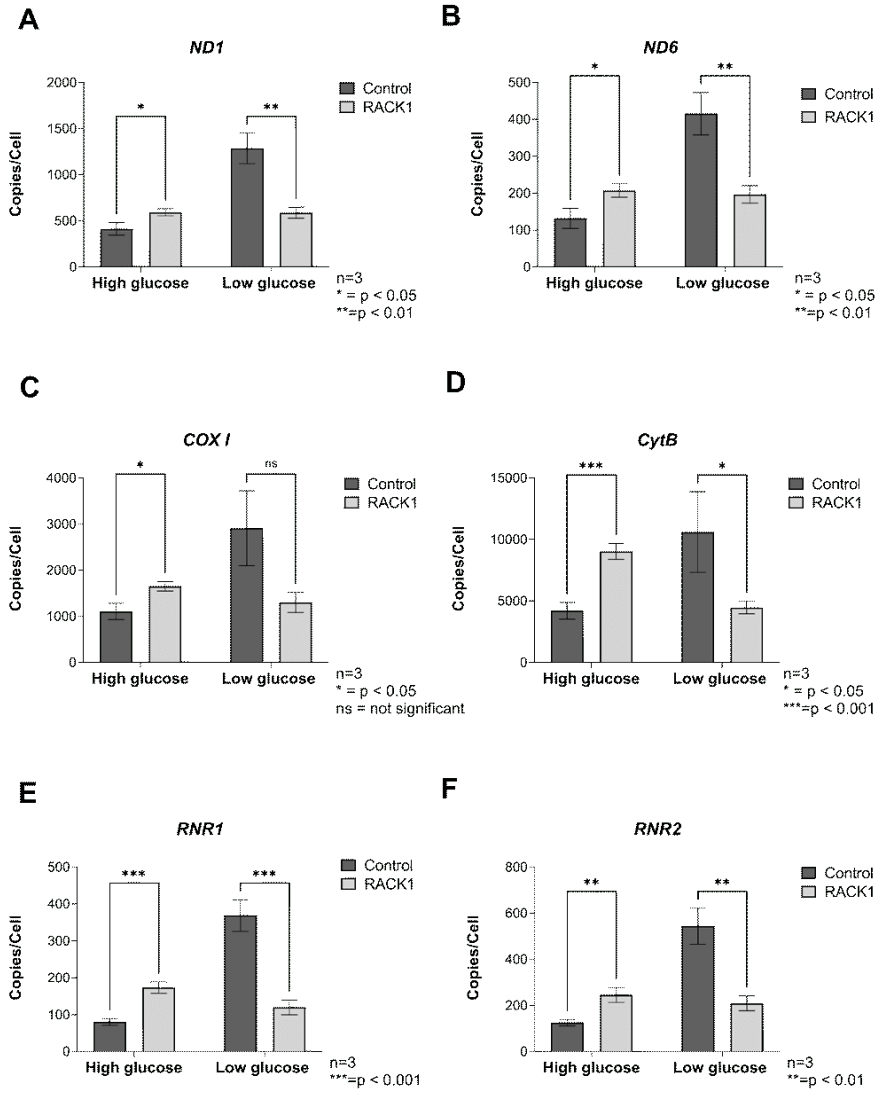

Figure 5.20: **Expression of mt-DNA-encoded genes in RACK1 KD cells.** mt-DNA genes A) *ND1,* B) *ND6,* C) *COX I,* D) *CytB,* E) *RNR1,* and F) *RNR2* levels were measured in mitochondria isolated from each of the four conditions. Results are reported as mt-DNA copies per cell, normalized to total cell counts. Results from 3 independent experiments are shown. Data presentation is mean± s.e.m. * = P≤0.05, ** = P≤0.01, *** = P≤0.001.

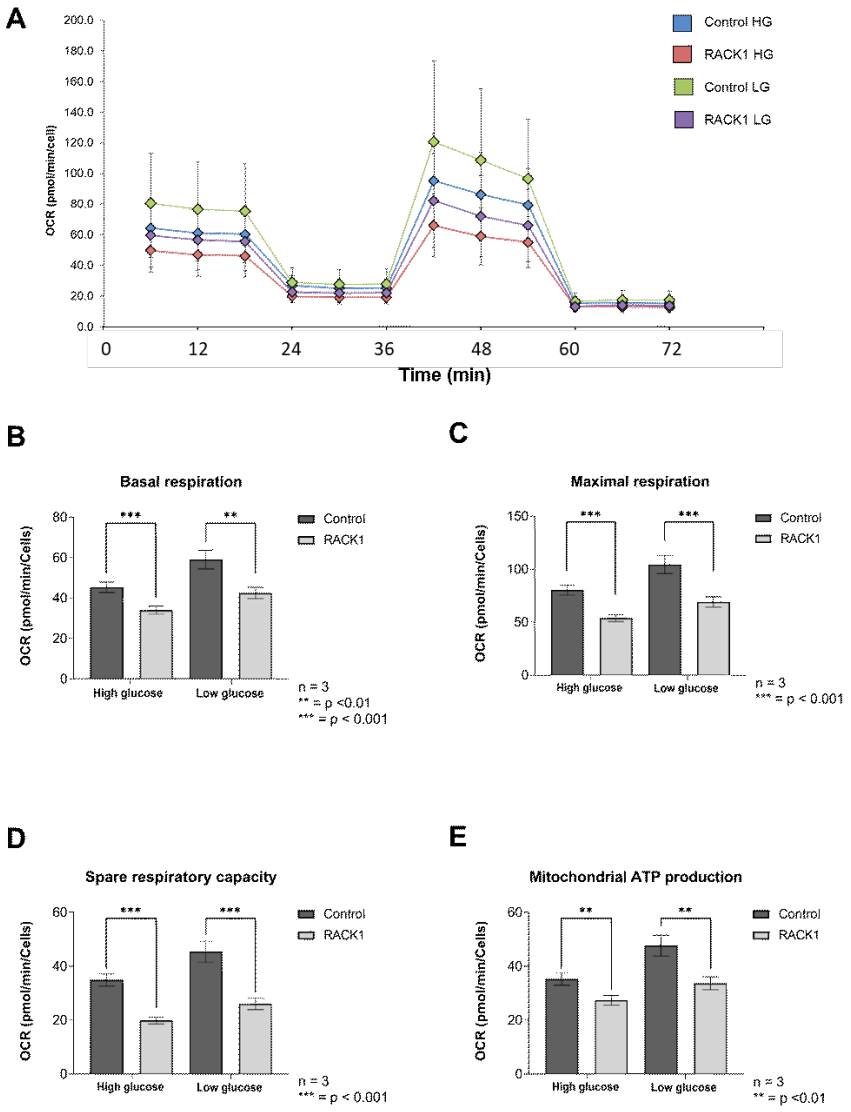

Figure 5.21: **Bioenergetic profiles of RACK1 KD cells.** (A) RACK1 KD/control cells were exposed to mitochondrial toxins Oligomycin (OG), FCCP, and Rotenone + Antimycin A (R/AA). Dotted lines indicate timing of toxin injection. X axis = injection numbers over time. Changes in oxygen consumption rate (OCR) is plotted over course of injection numbers to measure the response of each cell group. **(B-F).** Mitochondrial health indicators including **(B)** basal respiration values, **(C)** maximal respiration values, **(D)** spare respiratory capacity and **(E)** mitochondrial ATP production were measured using OCR and are compared between RACK1 KD HG/LG and controls. Results from 3 independent experiments are shown and were normalized to cell counts. Results from 3 independent experiments are shown. Data presentation is mean ± s.e.m. * = P $\leq$0.05, ** = P $\leq$0.01, *** = P $\leq$0.001.

A

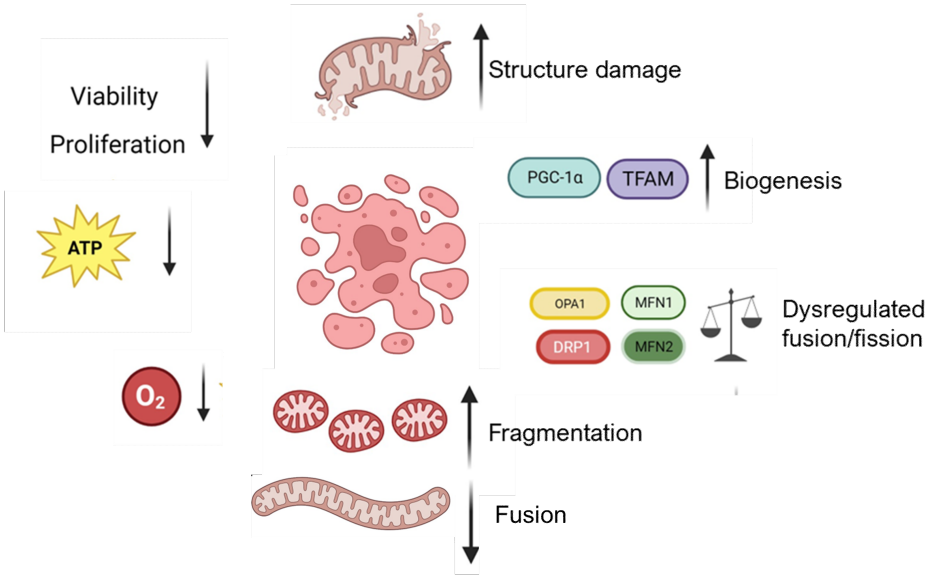

B

Cellular growth/energy			
Sample	**Viability**	**Proliferation**	**ATP production**
R1 KD HG	N/A	Decrease	Decrease
R1 KD LG	Decrease	Decrease	N/A
Membrane integrity			
Sample	**Membrane rupture**	**Loss of cristae**	**Inclusion bodies**
R1 KD HG	N/A	Increase	Increase
R1 KD LG	N/A	N/A	Increase
Network phenotype			
Sample	**Numbers**	**Filamen. network**	**Frag. network**
R1 KD HG	Increase	Decrease	Increase
R1 KD LG	N/A	Decrease	Increase
Network size parameters			
Sample	**Surface area**	**Volume**	**Volume/mitochondria**
R1 KD HG	Increase	Increase	Decrease
R1 KD LG	N/A	N/A	N/A
Biogenesis/fusion/fission mediators			
Sample	***PGC-1α/TFAM***	***OPA1/MFN1/MFN2***	***Drp1***
R1 KD HG	N/A	Decrease (MFN1 – N/A)	Decrease
R1 KD LG	Increase	Increase (OPA1/MFN1 – N/A)	N/A
Mt-DNA levels			
Sample	***ND1/ND6***	***COX I/CytB***	***RNR1/RNR2***
R1 KD HG	Increase	Increase	Increase
R1 KD LG	Decrease	Decrease (COX I – N/A)	Decrease
Mitochondrial bioenergetics			
Sample	**Basal respiration**	**Maximal respiration**	**Mitochondrial ATP production**
R1 KD HG	Decrease	Decrease	Decrease
R1 KD LG	Decrease	Decrease	Decrease

Figure 5.22: **A complete summary of cellular and mitochondrial responses to RACK1 KD in high and low glucose medium. (A)** The RACK1 KD impact upon mitochondrial form and function. A summary of the phenotype consistent between both the RACK1 KD sample in HG and LG medium. **(B)** A complete summary of cellular and mitochondrial responses to RACK1 KD in high and low glucose medium.

Bibliography

[1] David R Adams, Dorit Ron, and Patrick A Kiely. Rack1, a multifaceted scaffolding protein: Structure and function. *Cell communication and signaling*, 9(1):1–24, 2011.

[2] Sara Al-Reefy and Kefah Mokbel. The role of rack1 as an independent prognostic indicator in human breast cancer. *Breast cancer research and treatment*, 123(3):911–912, 2010.

[3] AM Ashique, V Kharazia, R Yaka, K Phamluong, AS Peterson, and D Ron. Localization of the scaffolding protein rack1 in the developing and adult mouse brain. *Brain research*, 1069(1):31–38, 2006.

[4] Fiorenzo Battaini and Alessia Pascale. Protein kinase c signal transduction regulation in physiological and pathological aging. *Annals of the New York Academy of Sciences*, 1057(1):177–192, 2005.

[5] Fiorenzo Battaini, Alessia Pascale, Laura Lucchi, Giulio M Pasinetti, and Stefano Govoni. Protein kinase c anchoring deficit in postmortem brains of alzheimer's disease patients. *Experimental neurology*, 159(2):559–564, 1999.

[6] Rebecca J Bird, George S Baillie, and Stephen J Yarwood. Interaction with receptor for activated c-kinase 1 (rack1) sensitizes the phosphodiesterase pde4d5 towards hydrolysis of camp and activation by protein kinase c. *Biochemical Journal*, 432(1):207–219, 2010.

[7] Pierre Boesch, Frédérique Weber-Lotfi, Noha Ibrahim, Vladislav Tarasenko, Anne Cosset, François Paulus, Robert N Lightowlers, and André Dietrich. Dna repair in organelles: pathways, organization, regulation, relevance in disease and aging. *Biochimica et Biophysica Acta (BBA)-Molecular Cell Research*, 1813(1):186–200, 2011.

[8] Dillon P Boulton and M Cecilia Caino. Mitochondrial fission and fusion in tumor progression to metastasis. *Frontiers in Cell and Developmental Biology*, 10:849962, 2022.

[9] MD Brand, AL Orr, IV Perevoshchikova, and CL Quinlan. The role of mitochondrial function and cellular bioenergetics in ageing and disease. *British Journal of Dermatology*, 169(s2):1–8, 2013.

[10] Wesley M Brown, Matthew George Jr, and Allan C Wilson. Rapid evolution of animal mitochondrial dna. *Proceedings of the National Academy of Sciences*, 76(4):1967–1971, 1979.

[11] Charito S Buensuceso, Darren Woodside, Janice L Huff, George E Plopper, and Timothy E O'Toole. The wd protein rack1 mediates protein kinase c and integrin-dependent cell migration. *Journal of cell science*, 114(9):1691–1698, 2001.

[12] Enrica Calura, Stefano Cagnin, Anna Raffaello, Paolo Laveder, Gerolamo Lanfranchi, and Chiara Romualdi. Meta-analysis of expression signatures of muscle atrophy: gene interaction networks in early and late stages. *BMC genomics*, 9:1–20, 2008.

[13] Cristina Camello-Almaraz, Pedro J Gomez-Pinilla, Maria J Pozo, and Pedro J Camello. Mitochondrial reactive oxygen species and ca2+ signaling. *American Journal of Physiology-Cell Physiology*, 291(5):C1082–C1088, 2006.

[14] Robert B Cameron, Craig C Beeson, and Rick G Schnellmann. Development of therapeutics that induce mitochondrial biogenesis for the treatment of acute and chronic degenerative diseases. *Journal of medicinal chemistry*, 59(23):10411–10434, 2016.

[15] Robert B Cameron, Yuri K Peterson, Craig C Beeson, and Rick G Schnellmann. Structural and pharmacological basis for the induction of mitochondrial biogenesis by formoterol but not clenbuterol. *Scientific reports*, 7(1):1–11, 2017.

[16] Graham R Campbell, Iryna Ziabreva, Amy K Reeve, Kim J Krishnan, Richard Reynolds, Owen Howell, Hans Lassmann, Doug M Turnbull, and Don J Mahad. Mitochondrial dna deletions and neurodegeneration in multiple sclerosis. *Annals of neurology*, 69(3):481–492, 2011.

[17] Xi-Xi Cao, Jing-Da Xu, Xiao-Li Liu, Jia-Wen Xu, Wen-Juan Wang, Qing-Quan Li, Qi Chen, Zu-De Xu, and Xiu-Ping Liu. Rack1: A superior independent predictor for poor clinical outcome in breast cancer. *International journal of cancer*, 127(5):1172–1179, 2010.

[18] Xi-Xi Cao, Jing-Da Xu, Jia-Wen Xu, Xiao-Li Liu, Yuan-Yuan Cheng, Wen-Juan Wang, Qing-Quan Li, Qi Chen, Zu-De Xu, and Xiu-Ping Liu. Rack1 promotes breast carcinoma proliferation and invasion/metastasis in vitro and in vivo. *Breast cancer research and treatment*, 123:375–386, 2010.

[19] Daviel Cardenas, Pamela M Carter, Catherine S Nation, Juan C Pizarro, Jessie Guidry, Ashok Aiyar, and Ben L Kelly. Lack, a rack 1 ortholog, facilitates cytochrome c oxidase subunit expression to promote l eishmania major fitness. *Molecular microbiology*, 96(1):95–109, 2015.

[20] Elisabetta Catalani, Silvia Zecchini, Matteo Giovarelli, Agnese Cherubini, Simona Del Quondam, Kashi Brunetti, Federica Silvestri, Paulina Roux-Biejat, Alessandra Napoli, Silvia Rosanna Casati, et al. Rack1 is evolutionary conserved in satellite stem cell activation and adult skeletal muscle regeneration. *Cell Death Discovery*, 8(1):459, 2022.

[21] Thomas Cavalier-Smith. Origin of mitochondria by intracellular enslavement of a photosynthetic purple bacterium. *Proceedings of the Royal Society B: Biological Sciences*, 273(1596):1943–1952, 2006.

[22] Marcello Ceci, Cristina Gaviraghi, Chiara Gorrini, Leonardo A Sala, Nina Offenhäuser, Pier Carlo Marchisio, and Stefano Biffo. Release of eif6 (p27bbp) from the 60s subunit allows 80s ribosome assembly. *Nature*, 426(6966):579–584, 2003.

[23] Ian G Chambers, Praveen Kumar, Jens Lichtenberg, Pengcheng Wang, Jianshi Yu, John D Phillips, Maureen A Kane, David Bodine, and Iqbal Hamza. Mrp5 and mrp9 play a concerted role in male reproduction and mitochondrial function. *Proceedings of the National Academy of Sciences*, 119(6):e2111617119, 2022.

[24] Shilpi Chaudhary, Shuvadeep Ganguly, Jayanth Kumar Palanichamy, Archna Singh, Dibyabhaba Pradhan, Radhika Bakhshi, Anita Chopra, and Sameer Bakhshi. Decoding mitochondrial genes in pediatric aml and development of a novel prognostic mitochondrial gene signature. *medRxiv*, pages 2022–04, 2022.

[25] Le Chen, Allison J Winger, and Anne A Knowlton. Mitochondrial dynamic changes in health and genetic diseases. *Molecular biology reports*, 41:7053–7062, 2014.

[26] Songhai Chen, Edward J Dell, Fang Lin, Jiqing Sai, and Heidi E Hamm. Rack1 regulates specific functions of g$\beta\gamma$. *Journal of Biological Chemistry*, 279(17):17861–17868, 2004.

[27] Tao Chen, Yue Wang, Yu-Hai Wang, and Chun-Hua Hang. The mfn1-βiipkc interaction regulates mitochondrial dysfunction via sirt3 following experimental subarachnoid hemorrhage. *Translational Stroke Research*, 13(5):845–857, 2022.

[28] Dongmei Cheng, Xiao Zhu, Federica Barchiesi, Delbert G Gillespie, Raghvendra K Dubey, and Edwin K Jackson. Receptor for activated protein kinase c1 regulates cell proliferation by modulating calcium signaling. *Hypertension*, 58(4):689–695, 2011.

[29] Meiyu Cheng, Huimei Yu, Qinghuan Kong, Bingrong Wang, Luyan Shen, Delu Dong, and Liankun Sun. The mitochondrial phb2/oma1/dele1 pathway cooperates with endoplasmic reticulum stress to facilitate the response to chemotherapeutics in ovarian cancer. *International Journal of Molecular Sciences*, 23(3):1320, 2022.

[30] Wei-Chun Chou, Zengli Guo, Hao Guo, Liang Chen, Ge Zhang, Kaixin Liang, Ling Xie, Xianming Tan, Sara A Gibson, Elena Rampanelli, et al. Aim2 in regulatory t cells restrains autoimmune diseases. *Nature*, 591(7849):300–305, 2021.

[31] Yii-Cheng Chou, Chih-Chung Chou, Yi-Kai Chen, Shorn Tsai, Francis MJ Hsieh, Hon Ju Liu, and Tzong-Hsiung Hseu. Structure and genomic organization of porcine rack1 gene. *Biochimica et Biophysica Acta (BBA)-Gene Structure and Expression*, 1489(2-3):315–322, 1999.

[32] Scott M Coyle, Wendy V Gilbert, and Jennifer A Doudna. Direct link between rack1 function and localization at the ribosome in vivo. *Molecular and cellular biology*, 29(6):1626–1634, 2009.

[33] Wenting Dai and Lei Jiang. Dysregulated mitochondrial dynamics and metabolism in obesity, diabetes, and cancer. *Frontiers in endocrinology*, 10:570, 2019.

[34] Edward J Dell, Jennifer Connor, Songhai Chen, Elizabeth G Stebbins, Nikolai P Skiba, Daria Mochly-Rosen, and Heidi E Hamm. The $\beta\gamma$ subunit of heterotrimeric g proteins interacts with rack1 and two other wd repeat proteins. *Journal of Biological Chemistry*, 277(51):49888–49895, 2002.

[35] Maria R Depaoli, Felix Karsten, Corina T Madreiter-Sokolowski, Christiane Klec, Benjamin Gottschalk, Helmut Bischof, Emrah Eroglu, Markus Waldeck-Weiermair, Thomas Simmen, Wolfgang F Graier, et al. Real-time imaging of mitochondrial atp dynamics reveals the metabolic setting of single cells. *Cell reports*, 25(2):501–512, 2018.

[36] Fangfang Duan, Hao Wu, Dongwei Jia, Weicheng Wu, Shifang Ren, Lan Wang, Shushu Song, Xinying Guo, Fenglin Liu, Yuanyuan Ruan, et al. O-glcnacylation of rack1 promotes hepatocellular carcinogenesis. *Journal of hepatology*, 68(6):1191–1202, 2018.

[37] Verónica Eisner, Martin Picard, and György Hajnóczky. Mitochondrial dynamics in adaptive and maladaptive cellular stress responses. *Nature cell biology*, 20(7):755–765, 2018.

[38] Yanling Fan, Weiyao Si, Wei Ji, Zhiyong Wang, Zicong Gao, Ran Tian, Weijie Song, He Zhang, Ruifang Niu, and Fei Zhang. Rack1 mediates tyrosine phosphorylation of anxa2 by src and promotes invasion and metastasis in drug-resistant breast cancer cells. *Breast Cancer Research*, 21:1–16, 2019.

[39] Evelyn Fessler, Eva-Maria Eckl, Sabine Schmitt, Igor Alves Mancilla, Matthias F Meyer-Bender, Monika Hanf, Julia Philippou-Massier, Stefan Krebs, Hans Zischka, and Lucas T Jae. A pathway coordinated by dele1 relays mitochondrial stress to the cytosol. *Nature*, 579(7799):433–437, 2020.

[40] Edismauro G Freitas Filho, Elaine ZM da Silva, Hwei Ling Ong, William D Swaim, Indu S Ambudkar, Constance Oliver, and Maria Célia Jamur. Rack1 plays a critical role in mast cell secretion and ca2+ mobilization by modulating f-actin dynamics. *Journal of Cell Science*, 134(9):jcs252585, 2021.

[41] Nicolaas AP Franken, Hans M Rodermond, Jan Stap, Jaap Haveman, and Chris Van Bree. Clonogenic assay of cells in vitro. *Nature protocols*, 1(5):2315–2319, 2006.

[42] Simone Gallo, Sara Ricciardi, Nicola Manfrini, Elisa Pesce, Stefania Oliveto, Piera Calamita, Marilena Mancino, Elisa Maffioli, Monica Moro, Mariacristina Crosti, et al. Rack1 specifically regulates translation through its binding to ribosomes. *Molecular and Cellular Biology*, 38(23):e00230–18, 2018.

[43] Valentina Gandin, Daniela Senft, Ivan Topisirovic, and Ze'ev A Ronai. Rack1 function in cell motility and protein synthesis. *Genes & cancer*, 4(9-10):369–377, 2013.

[44] Preston Ge, Valina L Dawson, and Ted M Dawson. Pink1 and parkin mitochondrial quality control: A source of regional vulnerability in parkinson's disease. *Molecular neurodegeneration*, 15:1–18, 2020.

[45] Steven Xijin Ge, Dongmin Jung, and Runan Yao. Shinygo: a graphical gene-set enrichment tool for animals and plants. *Bioinformatics*, 36(8):2628–2629, 2020.

[46] Niels Geijsen, Marcel Spaargaren, Jan AM Raaijmakers, Jan-Willem J Lammers, Leo Koenderman, and Paul J Coffer. Association of rack1 and pkcβ with the common β-chain of the il-5/il-3/gm-csf receptor. *Oncogene*, 18(36):5126–5130, 1999.

[47] Vincent R Gerbasi, Connie M Weaver, Salisha Hill, David B Friedman, and Andrew J Link. Yeast asc1p and mammalian rack1 are functionally orthologous core 40s ribosomal proteins that repress gene expression. *Molecular and cellular biology*, 24(18):8276–8287, 2004.

[48] Giulia Girolimetti, Flora Guerra, Luisa Iommarini, Ivana Kurelac, Daniele Vergara, Michele Maffia, Michele Vidone, Laura Benedetta Amato, Giulia Leone, Sabrina Dusi, et al. Platinum-induced mitochondrial dna mutations confer lower sensitivity to paclitaxel by impairing tubulin cytoskeletal organization. *Human Molecular Genetics*, 26(15):2961–2974, 2017.

[49] Michael W Gray, Gertraud Burger, and B Franz Lang. Mitochondrial evolution. *Science*, 283(5407):1476–1481, 1999.

[50] Xia Gu, Yuan Ma, Yi Liu, and Qiang Wan. Measurement of mitochondrial respiration in adherent cells by seahorse xf96 cell mito stress test. *STAR protocols*, 2(1):100245, 2021.

[51] M Guha, S Srinivasan, G Ruthel, AK Kashina, RP Carstens, A Mendoza, C Khanna, T Van Winkle, and NG Avadhani. Mitochondrial retrograde signaling induces epithelial–mesenchymal transition and generates breast cancer stem cells. *Oncogene*, 33(45):5238–5250, 2014.

[52] Anna L Hatch, Wei-Ke Ji, Ronald A Merrill, Stefan Strack, and Henry N Higgs. Actin filaments as dynamic reservoirs for drp1 recruitment. *Molecular biology of the cell*, 27(20):3109–3121, 2016.

[53] Antentor Hinton Jr, Prasanna Katti, Trace A Christensen, Margaret Mungai, Jianqiang Shao, Liang Zhang, Sergey Trushin, Ahmad Alghanem, Adam Jaspersen, Rachel E Geroux, et al. A comprehensive approach to sample preparation for electron microscopy and the assessment of mitochondrial morphology in tissue and cultured cells. *Advanced biology*, page 2200202, 2023.

[54] Riekelt H Houtkooper, Laurent Mouchiroud, Dongryeol Ryu, Norman Moullan, Elena Katsyuba, Graham Knott, Robert W Williams, and Johan Auwerx. Mitonuclear protein imbalance as a conserved longevity mechanism. *Nature*, 497(7450):451–457, 2013.

[55] Guomin Huang, Hongyan Li, and Hong Zhang. Abnormal expression of mitochondrial ribosomal proteins and their encoding genes with cell apoptosis and diseases. *International journal of molecular sciences*, 21(22):8879, 2020.

[56] Jyun-Bin Huang, Shih-Pin Hsu, Hsiu-Yung Pan, Shang-Der Chen, Shu-Fang Chen, Tsu-Kung Lin, Xuan-Ping Liu, Jie-Hau Li, Nai-Ching Chen, Chia-Wei Liou, et al. Peroxisome proliferator-activated receptor γ coactivator 1α activates vascular endothelial growth factor that protects against neuronal cell death following status epilepticus through pi3k/akt and mek/erk signaling. *International Journal of Molecular Sciences*, 21(19):7247, 2020.

[57] Tomomi Ide, Hiroyuki Tsutsui, Shunji Hayashidani, Dongchon Kang, Nobuhiro Suematsu, Kei-ichiro Nakamura, Hideo Utsumi, Naotaka Hamasaki, and Akira Takeshita. Mitochondrial dna damage and dysfunction associated with oxidative stress in failing hearts after myocardial infarction. *Circulation research*, 88(5):529–535, 2001.

[58] Yoshiyuki Ikeda, Akihiro Shirakabe, Christopher Brady, Daniela Zablocki, Mitsuru Ohishi, and Junichi Sadoshima. Molecular mechanisms mediating mitochondrial dynamics and mitophagy and their functional roles in the cardiovascular system. *Journal of molecular and cellular cardiology*, 78:116–122, 2015.

[59] Sujata Jha, Madeline G Rollins, Gabriele Fuchs, Dean J Procter, Elizabeth A Hall, Kira Cozzolino, Peter Sarnow, Jeffrey N Savas, and Derek Walsh. Transkingdom mimicry underlies ribosome customization by a poxvirus kinase. *Nature*, 546(7660):651–655, 2017.

[60] Szymon Juszkiewicz and Ramanujan S Hegde. Initiation of quality control during poly (a) translation requires site-specific ribosome ubiquitination. *Molecular cell*, 65(4):743–750, 2017.

[61] Anton MF Kalsbeek, Eva KF Chan, Judith Grogan, Desiree C Petersen, Weerachai Jaratlerdsiri, Ruta Gupta, Ruth J Lyons, Anne-Maree Haynes, Lisa G Horvath, James G Kench, et al. Altered mitochondrial genome content signals worse pathology and prognosis in prostate cancer. *The Prostate*, 78(1):25–31, 2018.

[62] Patrick A Kiely, George S Baillie, Robert Barrett, Deirdre A Buckley, David R Adams, Miles D Houslay, and Rosemary O'Connor. Phosphorylation of rack1 on tyrosine 52 by c-abl is required for insulin-like growth factor i-mediated regulation of focal adhesion kinase. *Journal of Biological Chemistry*, 284(30):20263–20274, 2009.

[63] Patrick A Kiely, George S Baillie, Martin J Lynch, Miles D Houslay, and Rosemary O'Connor. Tyrosine 302 in rack1 is essential for insulin-like growth factor-i-mediated competitive binding of pp2a and β1 integrin and for tumor cell proliferation and migration. *Journal of Biological Chemistry*, 283(34):22952–22961, 2008.

[64] Patrick A Kiely, Madeline Leahy, Denise O'Gorman, and Rosemary O'Connor. Rack1-mediated integration of adhesion and insulin-like growth factor i (igf-i) signaling and cell migration are defective in cells expressing an igf-i receptor mutated at tyrosines 1250 and 1251. *Journal of Biological Chemistry*, 280(9):7624–7633, 2005.

[65] Patrick A Kiely, Denise O'Gorman, Ken Luong, Dorit Ron, and Rosemary O'Connor. Insulin-like growth factor i controls a mutually exclusive association of rack1 with protein phosphatase 2a and β1 integrin to promote cell migration. *Molecular and cellular biology*, 26(11):4041–4051, 2006.

[66] Patrick A Kiely, Anagha Sant, and Rosemary O'Connor. Rack1 is an insulin-like growth factor 1 (igf-1) receptor-interacting protein that can regulate igf-1-mediated akt activation and protection from cell death. *Journal of Biological Chemistry*, 277(25):22581–22589, 2002.

[67] Patrick A Kiely, Anagha Sant, and Rosemary O'Connor. Rack1 is an insulin-like growth factor 1 (igf-1) receptor-interacting protein that can regulate igf-1-mediated akt activation and protection from cell death. *Journal of Biological Chemistry*, 277(25):22581–22589, 2002.

[68] Patrick A Kiely, Anagha Sant, and Rosemary O'Connor. Rack1 is an insulin-like growth factor 1 (igf-1) receptor-interacting protein that can regulate igf-1-mediated akt activation and protection from cell death. *Journal of Biological Chemistry*, 277(25):22581–22589, 2002.

[69] Hag Dong Kim, EunBin Kong, YongJoong Kim, Jin-Soo Chang, and Joon Kim. Rack1 depletion in the ribosome induces selective translation for non-canonical autophagy. *Cell death & disease*, 8(5):e2800–e2800, 2017.

[70] YE Kushnareva, AA Gerencser, B Bossy, WK Ju, AD White, J Waggoner, MH Ellisman, G Perkins, and E Bossy-Wetzel. Loss of opa1 disturbs cellular calcium homeostasis and sensitizes for excitotoxicity. *Cell Death & Differentiation*, 20(2):353–365, 2013.

[71] Jacob Lam, Prasanna Katti, Michelle Biete, Margaret Mungai, Salma AshShareef, Kit Neikirk, Edgar Garza Lopez, Zer Vue, Trace A Christensen, Heather K Beasley, et al. A universal approach to analyzing transmission electron microscopy with imagej. *Cells*, 10(9):2177, 2021.

[72] Jennifer Law, Isabel Kwek, Orysya Svystun, Jonathan Lim, Chong Teik Tan, Le Luong, C Yu Victor, and Shairaz Baksh. Rack1/traf2 regulation of modulator of apoptosis-1 (moap-1). *Biochimica et Biophysica Acta (BBA)-Molecular Cell Research*, 1865(5):684–694, 2018.

[73] Nichola Z Lax, Doug M Turnbull, and Amy K Reeve. Mitochondrial mutations: newly discovered players in neuronal degeneration. *The Neuroscientist*, 17(6):645–658, 2011.

[74] H-S Lee, SJ Millward-Sadler, MO Wright, G Nuki, R Al-Jamal, and DM Salter. Activation of integrin—rack1/pkcα signalling in human articular chondrocyte mechanotransduction. *Osteoarthritis and cartilage*, 10(11):890–897, 2002.

[75] You-Kyung Lee and Jin-A Lee. Role of the mammalian atg8/lc3 family in autophagy: differential and compensatory roles in the spatiotemporal regulation of autophagy. *BMB reports*, 49(8):424, 2016.

[76] D Li and R Roberts. Human genome and diseases: Wd-repeat proteins: structure characteristics, biological function, and their involvement in human diseases. *Cellular and Molecular Life Sciences CMLS*, 58:2085–2097, 2001.

[77] JJ Li and D Xie. Rack1, a versatile hub in cancer. *Oncogene*, 34(15):1890–1898, 2015.

[78] JJ Li and D Xie. Rack1, a versatile hub in cancer. *Oncogene*, 34(15):1890–1898, 2015.

[79] Maria V Liberti and Jason W Locasale. The warburg effect: how does it benefit cancer cells? *Trends in biochemical sciences*, 41(3):211–218, 2016.

[80] Joanna Liliental and David D Chang. Rack1, a receptor for activated protein kinase c, interacts with integrin β subunit. *Journal of Biological Chemistry*, 273(4):2379–2383, 1998.

[81] Wencheng Lin, Zhiqiang Zhang, Zhichao Xu, Bin Wang, Xiaoqi Li, Hong Cao, Yongqiang Wang, and Shijun J Zheng. The association of receptor of activated protein kinase c 1 (rack1) with infectious bursal disease virus viral protein vp5 and voltage-dependent anion channel 2 (vdac2) inhibits apoptosis and enhances viral replication. *Journal of Biological Chemistry*, 290(13):8500–8510, 2015.

[82] Dong Liu, Yiming Lin, Ting Kang, Bo Huang, Wei Xu, Minerva Garcia-Barrio, Moshood Olatinwo, Roland Matthews, Y Eugene Chen, and Winston E Thompson. Mitochondrial dysfunction and adipogenic reduction by prohibitin silencing in 3t3-l1 cells. *PloS one*, 7(3):e34315, 2012.

[83] Wenhua Liu, Fei Dou, Jian Feng, and Zhen Yan. Rack1 is involved in β-amyloid impairment of muscarinic regulation of gabaergic transmission. *Neurobiology of aging*, 32(10):1818–1826, 2011.

[84] Qiao-Li Lv, Yuan-Tao Huang, Gui-Hua Wang, Yan-Ling Liu, Jin Huang, Qiang Qu, Bao Sun, Lei Hu, Lin Cheng, Shu-Hui Chen, et al. Overexpression of rack1 promotes metastasis by enhancing epithelial-mesenchymal transition and predicts poor prognosis in human glioma. *International journal of environmental research and public health*, 13(10):1021, 2016.

[85] Jun Ma, Rong Wu, Qiang Zhang, Jun-bing Wu, Jizhong Lou, Zheng Zheng, Jian-qing Ding, and Zengqiang Yuan. Dj-1 interacts with rack1 and protects neurons from oxidative-stress-induced apoptosis. *Biochemical Journal*, 462(3):489–497, 2014.

[86] Jun Ma, Rong Wu, Qiang Zhang, Jun-bing Wu, Jizhong Lou, Zheng Zheng, Jian-qing Ding, and Zengqiang Yuan. Dj-1 interacts with rack1 and protects neurons from oxidative-stress-induced apoptosis. *Biochemical Journal*, 462(3):489–497, 2014.

[87] Somya Madan, Bhavin Uttekar, Sayali Chowdhary, and Richa Rikhy. Mitochondria lead the way: mitochondrial dynamics and function in cellular movements in development and disease. *Frontiers in Cell and Developmental Biology*, 9:3810, 2022.

[88] V Mamidipudi and CA Cartwright. A novel pro-apoptotic function of rack1: suppression of src activity in the intrinsic and akt pathways. *Oncogene*, 28(50):4421–4433, 2009.

[89] Vidya Mamidipudi, Betty Y Chang, Rachel A Harte, Kelly C Lee, and Christine A Cartwright. Rack1 inhibits the serum-and anchorage-independent growth of v-src transformed cells. *FEBS letters*, 567(2-3):321–326, 2004.

[90] Lynn Margulis. Origin of eukaryotic cells: evidence and research implications for a theory of the origin and evolution of microbial, plant, and animal cells on the precambrian earth. *(No Title)*, 1970.

[91] Lynn Margulis. Symbiosis in cell evolution: Life and its environment on the early earth. 1981.

[92] Yoshitaka Matsuo, Ken Ikeuchi, Yasushi Saeki, Shintaro Iwasaki, Christian Schmidt, Tsuyoshi Udagawa, Fumiya Sato, Hikaru Tsuchiya, Thomas Becker,

Keiji Tanaka, et al. Ubiquitination of stalled ribosome triggers ribosome-associated quality control. *Nature communications*, 8(1):159, 2017.

[93] Heidi M McBride, Margaret Neuspiel, and Sylwia Wasiak. Mitochondria: more than just a powerhouse. *Current biology*, 16(14):R551–R560, 2006.

[94] A McCahill, J Warwicker, GB Bolger, MD Houslay, and SJ Yarwood. The rack1 scaffold protein: a dynamic cog in cell response mechanism. *Mol Pharmacol*, 62:1261–1273, 2002.

[95] Pauline Mencke, Ibrahim Boussaad, Chiara D Romano, Toshimori Kitami, Carole L Linster, and Rejko Krüger. The role of dj-1 in cellular metabolism and pathophysiological implications for parkinson's disease. *Cells*, 10(2):347, 2021.

[96] Prashant Mishra and David C Chan. Mitochondrial dynamics and inheritance during cell division, development and disease. *Nature reviews Molecular cell biology*, 15(10):634–646, 2014.

[97] Prashant Mishra and David C Chan. Mitochondrial dynamics and inheritance during cell division, development and disease. *Nature reviews Molecular cell biology*, 15(10):634–646, 2014.

[98] Yoshihiro Miyazono, Shingo Hirashima, Naotada Ishihara, Jingo Kusukawa, Kei-ichiro Nakamura, and Keisuke Ohta. Uncoupled mitochondria quickly shorten along their long axis to form indented spheroids, instead of rings, in a fission-independent manner. *Scientific reports*, 8(1):1–14, 2018.

[99] Jeremie Neasta, Anna Fiorenza, Dao-Yao He, Khanhky Phamluong, Patrick A Kiely, and Dorit Ron. Activation of the camp pathway induces rack1-dependent binding of β-actin to bdnf promoter. *Plos one*, 11(8):e0160948, 2016.

[100] EJ Neer. Schmidt cj, nambudripad r, smith tf. *The ancient regulatory-protein family of WD-repeat proteins. Nature*, 371:297–300, 1994.

[101] Hong-Min Ni, Jessica A Williams, and Wen-Xing Ding. Mitochondrial dynamics and mitochondrial quality control. *Redox biology*, 4:6–13, 2015.

[102] Maja Holch Nielsen, Rasmus Kock Flygaard, and Lasse Bohl Jenner. Structural analysis of ribosomal rack1 and its role in translational control. *Cellular Signalling*, 35:272–281, 2017.

[103] Jakob Nilsson, Jayati Sengupta, Joachim Frank, and Poul Nissen. Regulation of eukaryotic translation by the rack1 protein: a platform for signalling molecules on the ribosome. *EMBO reports*, 5(12):1137–1141, 2004.

[104] Laura D Osellame, Thomas S Blacker, and Michael R Duchen. Cellular and molecular mechanisms of mitochondrial function. *Best practice & research Clinical endocrinology & metabolism*, 26(6):711–723, 2012.

[105] Babu J Padanilam. Induction and subcellular localization of protein kinase c isozymes following renal ischemia. *Kidney international*, 59(5):1789–1797, 2001.

[106] Massimo Paoli. Protein folds propelled by diversity. *Progress in biophysics and molecular biology*, 76(1-2):103–130, 2001.

[107] Jin Hee Park, Eutteum Jeong, Jingjing Lin, Ryeojin Ko, Ji Hee Kim, Sol Yi, Youngjin Choi, In-Cheol Kang, Daekee Lee, and Soo Young Lee. Rack1 interaction with c-src is essential for osteoclast function. *Experimental & Molecular Medicine*, 51(7):1–9, 2019.

[108] Jason Pass, Jun Zhang, Yu-Ting Zheng, Roberto Bolli, and Peipei Ping. Enhanced pkcβii translocation and pkcβii-rack1 interactions in pkcε-induced cardiac hypertrophy and failure: A role for rack1. *Journal of Molecular and Cellular Cardiology*, 6(33):A90, 2001.

[109] Randen L Patterson, Damian B Van Rossum, Roxanne K Barrow, and Solomon H Snyder. Rack1 binds to inositol 1, 4, 5-trisphosphate receptors and mediates ca2+ release. *Proceedings of the National Academy of Sciences*, 101(8):2328–2332, 2004.

[110] Perla Perez-Trevino, Mónica Velásquez, and Noemi Garcia. Mechanisms of mitochondrial dna escape and its relationship with different metabolic diseases. *Biochimica et Biophysica Acta (BBA)-Molecular Basis of Disease*, 1866(6):165761, 2020.

[111] Anastasia V Poznyak, Ekaterina A Ivanova, Igor A Sobenin, Shaw-Fang Yet, and Alexander N Orekhov. The role of mitochondria in cardiovascular diseases. *Biology*, 9(6):137, 2020.

[112] Long Qian, Jiahai Shi, Chi Zhang, Jiawei Lu, Xiaoning Lu, Kunpeng Wu, Chen Yang, Daliang Yan, Chao Zhang, Qingsheng You, et al. Downregulation of rack1 is associated with cardiomyocyte apoptosis after myocardial ischemia/reperfusion injury in adult rats. *In Vitro Cellular & Developmental Biology-Animal*, 52:305–313, 2016.

[113] Guihua Qiu, Jian Liu, Qianqian Cheng, Qingyang Wang, Zhaofei Jing, Yujun Pei, Min Zhao, Jing Wang, Jessie Yanxiang Guo, and Jiyan Zhang. Impaired autophagy and defective t cell homeostasis in mice with t cell-specific deletion of receptor for activated c kinase 1. *Frontiers in immunology*, 8:575, 2017.

[114] Rubén Quintana-Cabrera, Israel Manjarrés-Raza, Carlos Vicente-Gutiérrez, Mauro Corrado, Juan P Bolanos, and Luca Scorrano. Opa1 relies on cristae preservation and atp synthase to curtail reactive oxygen species accumulation in mitochondria. *Redox Biology*, 41:101944, 2021.

[115] Nicole Rachfall, Kerstin Schmitt, Susanne Bandau, Nadine Smolinski, Armin Ehrenreich, Oliver Valerius, and Gerhard H Braus. Rack1/asc1p, a ribosomal node in cellular signaling. *Molecular & Cellular Proteomics*, 12(1):87–105, 2013.

[116] Michela Ranieri, Simona Brajkovic, Giulietta Riboldi, Dario Ronchi, Federica Rizzo, Nereo Bresolin, Stefania Corti, and Giacomo P Comi. Mitochondrial fusion proteins and human diseases. *Neurology research international*, 2013, 2013.

[117] Sneha Rath, Rohit Sharma, Rahul Gupta, Tslil Ast, Connie Chan, Timothy J Durham, Russell P Goodman, Zenon Grabarek, Mary E Haas, Wendy HW Hung, et al. Mitocarta3. 0: an updated mitochondrial proteome now with sub-organelle localization and pathway annotations. *Nucleic acids research*, 49(D1):D1541–D1547, 2021.

[118] P Hemachandra Reddy. Inhibitors of mitochondrial fission as a therapeutic strategy for diseases with oxidative stress and mitochondrial dysfunction. *Journal of Alzheimer's Disease*, 40(2):245–256, 2014.

[119] Cindy L Reiner, Jennifer S McCullar, Rebecca L Kow, Joshua H Le, David R Goodlett, and Neil M Nathanson. Rack1 associates with muscarinic receptors and regulates m2 receptor trafficking. *PLoS One*, 5(10):e13517, 2010.

[120] Lin Ren, Li Meng, Jing Gao, Mingdian Lu, Chengyu Guo, Yunyun Li, Ziye Rong, and Yan Ye. Phb2 promotes colorectal cancer cell proliferation and tumorigenesis through ndufs1-mediated oxidative phosphorylation. *Cell Death & Disease*, 14(1):44, 2023.

[121] D Ron. Jiang z, yao l, vagts a, diamond i, gordon a. *Coordinated movement of RACK1 with activated betaIIPKC. J Biol Chem*, 274:27039–27046, 1999.

[122] D Ron and Mochly-Rosen D. An autoregulatory region in protein kinase c: the pseudoanchoring site. *Proceedings of the National Academy of Sciences*, 92:492–496, 1995.

[123] D Ron, J Luo, and D Mochly-Rosen. C2 region-derived peptides inhibit translocation and function of β protein kinase c in vivo. *J Biol Chem*, 270:24180–24187, 1995.

[124] Dorit Ron, Che-Hong Chen, Jeremy Caldwell, Lee Jamieson, Elisha Orr, and Daria Mochly-Rosen. Cloning of an intracellular receptor for protein kinase c: a homolog of the beta subunit of g proteins. *Proceedings of the National Academy of Sciences*, 91(3):839–843, 1994.

[125] Antje K Rottner, Yingying Ye, Elena Navarro-Guerrero, Varsha Rajesh, Alina Pollner, Romina J Bevacqua, Jing Yang, Aliya F Spigelman, Roberta Baronio, Austin Bautista, et al. A genome-wide crispr screen identifies calcoco2 as a

regulator of beta cell function influencing type 2 diabetes risk. *Nature Genetics*, 55(1):54–65, 2023.

[126] Joanna Rusecka, Magdalena Kaliszewska, Ewa Bartnik, and Katarzyna Tońska. Nuclear genes involved in mitochondrial diseases caused by instability of mitochondrial dna. *Journal of applied genetics*, 59:43–57, 2018.

[127] Joanna Rusecka, Magdalena Kaliszewska, Ewa Bartnik, and Katarzyna Tońska. Nuclear genes involved in mitochondrial diseases caused by instability of mitochondrial dna. *Journal of applied genetics*, 59:43–57, 2018.

[128] Richard C Scarpulla, Rick B Vega, and Daniel P Kelly. Transcriptional integration of mitochondrial biogenesis. *Trends in Endocrinology & Metabolism*, 23(9):459–466, 2012.

[129] Caroline A Schneider, Wayne S Rasband, and Kevin W Eliceiri. Nih image to imagej: 25 years of image analysis. *Nature methods*, 9(7):671–675, 2012.

[130] Jayati Sengupta, Jakob Nilsson, Richard Gursky, Christian MT Spahn, Poul Nissen, and Joachim Frank. Identification of the versatile scaffold protein rack1 on the eukaryotic ribosome by cryo-em. *Nature structural & molecular biology*, 11(10):957–962, 2004.

[131] Bryan Serrels, Emma Sandilands, and Margaret C Frame. Signaling of the direction-sensing fak/rack1/pde4d5 complex to the small gtpase rap1. *Small GTPases*, 2(1):1086–1092, 2011.

[132] Bryan Serrels, Emma Sandilands, Alan Serrels, George Baillie, Miles D Houslay, Valerie G Brunton, Marta Canel, Laura M Machesky, Kurt I Anderson, and Margaret C Frame. A complex between fak, rack1, and pde4d5 controls spreading initiation and cancer cell polarity. *Current Biology*, 20(12):1086–1092, 2010.

[133] Reika Shiratori, Kenta Furuichi, Masashi Yamaguchi, Natsumi Miyazaki, Haruna Aoki, Hiroji Chibana, Kousei Ito, and Shigeki Aoki. Glycolytic suppression dramatically changes the intracellular metabolic profile of multiple cancer cell lines in a mitochondrial metabolism-dependent manner. *Scientific reports*, 9(1):1–15, 2019.

[134] Boris Shor, Jimmy Calaycay, Julie Rushbrook, and Maureen McLeod. Cpc2/rack1 is a ribosome-associated protein that promotes efficient translation in schizosaccharomyces pombe. *Journal of Biological Chemistry*, 278(49):49119–49128, 2003.

[135] Han Shuwen, Yang Xi, and Pan Yuefen. Can mitochondria dna provide a novel biomarker for evaluating the risk and prognosis of colorectal cancer? *Disease markers*, 2017, 2017.

[136] Bhupendra Singh, Josephine S Modica-Napolitano, and Keshav K Singh. Defining the momiome: Promiscuous information transfer by mobile mitochondria and the mitochondrial genome. In *Seminars in cancer biology*, volume 47, pages 1–17. Elsevier, 2017.

[137] Ritika Singh, Ayushi Jain, Jayanth Kumar Palanichamy, TC Nag, Sameer Bakhshi, and Archna Singh. Ultrastructural changes in cristae of lymphoblasts in acute lymphoblastic leukemia parallel alterations in biogenesis markers. *Applied Microscopy*, 51(1):1–12, 2021.

[138] Cole S Sitron, Joseph H Park, and Onn Brandman. Asc1, hel2, and slh1 couple translation arrest to nascent chain degradation. *Rna*, 23(5):798–810, 2017.

[139] Ella H Sklan, Erez Podoly, and Hermona Soreq. Rack1 has the nerve to act: structure meets function in the nervous system. *Progress in neurobiology*, 78(2):117–134, 2006.

[140] Ella H Sklan, Erez Podoly, and Hermona Soreq. Rack1 has the nerve to act: structure meets function in the nervous system. *Progress in neurobiology*, 78(2):117–134, 2006.

[141] Temple F Smith. Diversity of wd-repeat proteins. *The Coronin Family of Proteins: Subcellular Biochemistry*, pages 20–30, 2008.

[142] Jessica B Spinelli and Marcia C Haigis. The multifaceted contributions of mitochondria to cellular metabolism. *Nature cell biology*, 20(7):745–754, 2018.

[143] Elizabeth G Stebbins and Daria Mochly-Rosen. Binding specificity for rack1 resides in the v5 region of βii protein kinase c. *Journal of Biological Chemistry*, 276(32):29644–29650, 2001.

[144] David A Stroud and Michael T Ryan. Mitochondria: organization of respiratory chain complexes becomes cristae-lized. *Current Biology*, 23(21):R969–R971, 2013.

[145] Elayanambi Sundaramoorthy, Marilyn Leonard, Raymond Mak, Jeffrey Liao, Amitkumar Fulzele, and Eric J Bennett. Znf598 and rack1 regulate mammalian ribosome-associated quality control function by mediating regulatory 40s ribosomal ubiquitylation. *Molecular cell*, 65(4):751–760, 2017.

[146] Hidetoshi Suzuki, Yasufumi Katanasaka, Yoichi Sunagawa, Yusuke Miyazaki, Masafumi Funamoto, Hiromichi Wada, Koji Hasegawa, and Tatsuya Morimoto. Tyrosine phosphorylation of rack1 triggers cardiomyocyte hypertrophy by regulating the interaction between p300 and gata4. *Biochimica et Biophysica Acta (BBA)-Molecular Basis of Disease*, 1862(9):1544–1557, 2016.

[147] Kensei Taguchi, Bertha C Elias, Evan Krystofiak, Subo Qian, Snehal Sant, Haichun Yang, Agnes B Fogo, and Craig R Brooks. Quantitative super-resolution microscopy reveals promoting mitochondrial interconnectivity protects against aki. *Kidney360*, 2(12):1892, 2021.

[148] Mary K Thompson, Maria F Rojas-Duran, Paritosh Gangaramani, and Wendy V Gilbert. The ribosomal protein asc1/rack1 is required for efficient translation of short mrnas. *Elife*, 5:e11154, 2016.

[149] Mary K Thompson, Maria F Rojas-Duran, Paritosh Gangaramani, and Wendy V Gilbert. The ribosomal protein asc1/rack1 is required for efficient translation of short mrnas. *Elife*, 5:e11154, 2016.

[150] Mary K Thompson, Maria F Rojas-Duran, Paritosh Gangaramani, and Wendy V Gilbert. The ribosomal protein asc1/rack1 is required for efficient translation of short mrnas. *Elife*, 5:e11154, 2016.

[151] Claire Thornton, Ka-Choi Tang, Khanhky Phamluong, Ken Luong, Alicia Vagts, Donna Nikanjam, Rami Yaka, and Dorit Ron. Spatial and temporal regulation of rack1 function and n-methyl-d-aspartate receptor activity through wd40 motif-mediated dimerization. *Journal of Biological Chemistry*, 279(30):31357–31364, 2004.

[152] Martine Uittenbogaard and Anne Chiaramello. Mitochondrial biogenesis: a therapeutic target for neurodevelopmental disorders and neurodegenerative diseases. *Current pharmaceutical design*, 20(35):5574–5593, 2014.

[153] Ashley A Untereiner, Ming Fu, Katalin Módis, Rui Wang, YoungJun Ju, and Lingyun Wu. Stimulatory effect of cse-generated h2s on hepatic mitochondrial biogenesis and the underlying mechanisms. *Nitric Oxide*, 58:67–76, 2016.

[154] Anna Usacheva, Rebecca Smith, Richard Minshall, Gleb Baida, Seyha Seng, Ed Croze, and Oscar Colamonici. The wd motif-containing protein receptor for activated protein kinase c (rack1) is required for recruitment and activation of signal transducer and activator of transcription 1 through the type i interferon receptor. *Journal of Biological Chemistry*, 276(25):22948–22953, 2001.

[155] Alexander M Van der Bliek, Margaret M Sedensky, and Phil G Morgan. Cell biology of the mitochondrion. *Genetics*, 207(3):843–871, 2017.

[156] Viviana Volta, Anne Beugnet, Simone Gallo, Laura Magri, Daniela Brina, Elisa Pesce, Piera Calamita, Francesca Sanvito, and Stefano Biffo. Rack1 depletion in a mouse model causes lethality, pigmentation deficits and reduction in protein synthesis efficiency. *Cellular and Molecular Life Sciences*, 70:1439–1450, 2013.

[157] Timothy Wai and Thomas Langer. Mitochondrial dynamics and metabolic regulation. *Trends in Endocrinology & Metabolism*, 27(2):105–117, 2016.

[158] Timothy Wai and Thomas Langer. Mitochondrial dynamics and metabolic regulation. *Trends in Endocrinology & Metabolism*, 27(2):105–117, 2016.

[159] Douglas C Wallace and Dimitra Chalkia. Mitochondrial dna genetics and the heteroplasmy conundrum in evolution and disease. *Cold Spring Harbor perspectives in biology*, 5(11):a021220, 2013.

[160] Jun Wang, Sebastien Carnicella, Khanhky Phamluong, Jerome Jeanblanc, Jennifer A Ronesi, Nadia Chaudhri, Patricia H Janak, David M Lovinger, and Dorit Ron. Ethanol induces long-term facilitation of nr2b-nmda receptor activity in the dorsal striatum: implications for alcohol drinking behavior. *Journal of Neuroscience*, 27(13):3593–3602, 2007.

[161] Qingyang Wang, Silei Zhou, Jing-Yang Wang, Junxia Cao, Xueying Zhang, Jing Wang, Kun Han, Qianqian Cheng, Guihua Qiu, Yawei Zhao, et al. Rack1 antagonizes tnf-α-induced cell death by promoting p38 activation. *Scientific Reports*, 5(1):1–9, 2015.

[162] Shu Wang, Jin-zhong Chen, Zhen Zhang, Shaohua Gu, Chaoneng Ji, Rong Tang, Kang Ying, Yi Xie, and Yumin Mao. Cloning, expression and genomic structure of a novel human gnb2l1 gene, which encodes a receptor of activated protein kinase c (rack). *Molecular biology reports*, 30:53–60, 2003.

[163] Wang Wang, Georgios Karamanlidis, and Rong Tian. Novel targets for mitochondrial medicine. *Science translational medicine*, 8(326):326rv3–326rv3, 2016.

[164] Otto Warburg. The metabolism of carcinoma cells. *The Journal of Cancer Research*, 9(1):148–163, 1925.

[165] Peter Wehner, Iryna Shnitsar, Henning Urlaub, and Annette Borchers. Rack1 is a novel interaction partner of ptk7 that is required for neural tube closure. *Development*, 138(7):1321–1327, 2011.

[166] Tina Wenz. Regulation of mitochondrial biogenesis and pgc-1α under cellular stress. *Mitochondrion*, 13(2):134–142, 2013.

[167] Benedikt Westermann. Mitochondrial fusion and fission in cell life and death. *Nature reviews Molecular cell biology*, 11(12):872–884, 2010.

[168] Lauren P Westhaver, Sarah Nersesian, Riley J Arseneau, Joshua Hefler, Breanna KV Hargreaves, Alexander Edgar, Yara Azizieh, Nerea Cuesta-Gomez, Dayne L Izquierdo, James Shapiro, et al. Mitochondrial dna levels in perfusate and bile during ex vivo normothermic machine perfusion predict donor liver quality. *Available at SSRN 4435894*.

[169] Niluni M Wijesundara, Song F Lee, Zhenyu Cheng, Ross Davidson, David N Langelaan, and HP Vasantha Rupasinghe. Bactericidal activity of carvacrol against streptococcus pyogenes involves alteration of membrane fluidity and integrity through interaction with membrane phospholipids. *Pharmaceutics*, 14(10):1992, 2022.

[170] Tanila Wood dos Santos, Quélita Cristina Pereira, Lucimara Teixeira, Alessandra Gambero, Josep A. Villena, and Marcelo Lima Ribeiro. Effects of polyphenols on thermogenesis and mitochondrial biogenesis. *International journal of molecular sciences*, 19(9):2757, 2018.

[171] Yinyuan Wu, Yinyin Wang, Yang Sun, Liying Zhang, Dianjun Wang, Fangli Ren, Donald Chang, Zhijie Chang, and Baoqing Jia. Rack1 promotes bax oligomerization and dissociates the interaction of bax and bcl-xl. *Cellular signalling*, 22(10):1495–1501, 2010.

[172] Chao Xu and Jinrong Min. Structure and function of wd40 domain proteins. *Protein & cell*, 2:202–214, 2011.

[173] Yizhou Xu, Ningfu Wang, Feng Ling, Peizhang Li, and Yan Gao. Receptor for activated c-kinase 1, a novel binding partner of adiponectin receptor 1. *Biochemical and biophysical research communications*, 378(1):95–98, 2009.

[174] Rami Yaka, Dao-Yao He, Khanhky Phamluong, and Dorit Ron. Pituitary adenylate cyclase-activating polypeptide (pacap (1–38)) enhances n-methyl-d-aspartate receptor function and brain-derived neurotrophic factor expression via rack1. *Journal of Biological Chemistry*, 278(11):9630–9638, 2003.

[175] Rami Yaka, Khanhky Phamluong, and Dorit Ron. Scaffolding of fyn kinase to the nmda receptor determines brain region sensitivity to ethanol. *Journal of Neuroscience*, 23(9):3623–3632, 2003.

[176] Rami Yaka, Claire Thornton, Alicia J Vagts, Khanhky Phamluong, Antonello Bonci, and Dorit Ron. Nmda receptor function is regulated by the inhibitory scaffolding protein, rack1. *Proceedings of the National Academy of Sciences*, 99(8):5710–5715, 2002.

[177] Stephen J Yarwood, Michael R Steele, Grant Scotland, Miles D Houslay, and Graeme B Bolger. The rack1 signaling scaffold protein selectively interacts with the camp-specific phosphodiesterase pde4d5 isoform. *J Biol Chem*, 274:14909–14917, 2001.

[178] Laure Yatime, Kim Langemach Hein, Jakob Nilsson, and Poul Nissen. Structure of the rack1 dimer from saccharomyces cerevisiae. *Journal of molecular biology*, 411(2):486–498, 2011.

[179] Jian Ye, George Coulouris, Irena Zaretskaya, Ioana Cutcutache, Steve Rozen, and Thomas L Madden. Primer-blast: a tool to design target-specific primers for polymerase chain reaction. *BMC bioinformatics*, 13:1–11, 2012.

[180] Hong Yi, Xin-Hui Li, Bin Yi, Jie Zheng, Guo Zhu, Cui Li, Mao-Yu Li, Peng-Fei Zhang, Jian-Ling Li, Zhu-Chu Chen, et al. Identification of rack1, ef-tu and rhodanese as aging-related proteins in human colonic epithelium by proteomic analysis. *Journal of proteome research*, 9(3):1416–1423, 2010.

[181] Anna Zakrzewicz, Matthias Hecker, Leigh M Marsh, Grazyna Kwapiszewska, Bozena Nejman, Lu Long, Werner Seeger, Ralph T Schermuly, Nicholas W Morrell, Rory E Morty, et al. Receptor for activated c-kinase 1, a novel interaction partner of type ii bone morphogenetic protein receptor, regulates smooth muscle cell proliferation in pulmonary arterial hypertension. *Circulation*, 115(23):2957–2968, 2007.

[182] Weizhou Zhang, George Zhi Cheng, Jianli Gong, Ulrich Hermanto, Cong Susan Zong, Joseph Chan, Jin Quan Cheng, and Lu-Hai Wang. Rack1 and cis mediate the degradation of bimel in cancer cells. *Journal of Biological Chemistry*, 283(24):16416–16426, 2008.

[183] Weizhou Zhang, Cong S Zong, Ulrich Hermanto, Pablo Lopez-Bergami, Ze'ev Ronai, and Lu-Hai Wang. Rack1 recruits stat3 specifically to insulin and insulin-like growth factor 1 receptors for activation, which is important for regulating anchorage-independent growth. *Molecular and cellular biology*, 26(2):413–424, 2006.

[184] Yawei Zhao, Qingyang Wang, Guihua Qiu, Silei Zhou, Zhaofei Jing, Jingyang Wang, Wendie Wang, Junxia Cao, Kun Han, Qianqian Cheng, et al. Rack1 promotes autophagy by enhancing the atg14l-beclin 1-vps34-vps15 complex formation upon phosphorylation by ampk. *Cell reports*, 13(7):1407–1417, 2015.

[185] Jiejun Zhu, Xu Chen, Yun Song, Yuanyuan Zhang, Liming Zhou, and Lihong Wan. Deficit of rack1 contributes to the spatial memory impairment via upregulating beclin1 to induce autophagy. *Life sciences*, 151:115–121, 2016.